Symmetries and Topological order: realizations and signals in correlated strong spin-orbit coupled materials

by

Yi-Ping Huang

B.A., National Tsing-Hua University, 2008

M.S., University of Colorado at Boulder, 2012

A thesis submitted to the

Faculty of the Graduate School of the

University of Colorado in partial fulfillment

of the requirements for the degree of

Doctor of Philosophy

Department of Physics

2017

This thesis entitled:
Symmetries and Topological order: realizations and signals in correlated strong spin-orbit coupled materials
written by Yi-Ping Huang
has been approved for the Department of Physics

Prof. Michael Hermele

Prof. Victor Gurarie

Date

The final copy of this thesis has been examined by the signatories, and we find that both the content and the form meet acceptable presentation standards of scholarly work in the above mentioned discipline.

Huang, Yi-Ping (Ph.D., Physics)

Symmetries and Topological order: realizations and signals in correlated strong spin-orbit coupled materials

Thesis directed by Prof. Michael Hermele

Spin-orbit coupling exists in materials in general. However, it entangles the spin and orbital degrees of freedom and complicates the model. Thus, theorists usually neglect the effects induced by spin-orbit coupling first and consider spin-orbit coupling as perturbation next. The non-perturbative effects brought up by spin-orbit coupling are thus often less studied or overlooked.

On the other hand, the majority in the study of interacting topological order focusing on the general structure of theories and made significant advances by leaving material details behind. It is thus important to find possible microscopic models that could realize the new phases in laboratories and benefits from the progress of theories to make experimental predictions.

In this thesis, we study the physical effects due to strong spin-orbit coupling from the perspective of searching new quantum orders and the non-trivial responses.

(i) The first project, we propose the nontrivial dipolar-octupolar(DO) doublets on the pyrochlore lattice. By studying the most general symmetry allowed model at the localized and the itinerant limit for DO doublets, we found two 3D symmetry enriched topological orders and topological insulator correspondingly. (ii) In the second project, we analyze the 2D model descending from the localized limit of DO doublets on pyrochlore. The discrete onsite symmetry and space group symmetry could lead to a symmetry-enriched topological order with symmetry fractionalization pattern that cannot emerge from a spin model with continuous spin rotational symmetry. The non-trivial symmetry fractionalization pattern contributes to the striking numerical signal that can help identifying the topological order. (iii) In the third project, we develop a theory to understand the high-energy Raman signal in Sr_2IrO_4.

Dedication

To my parents, Te-Fu Huang and Wen-Yi (Yu-Lan) Lu.

Acknowledgements

First and foremost, I am sincerely grateful to my advisor, Prof. Michael Hermele, for the scientific support. I am lucky to work on a thesis project that expands across the interesting theoretical question and physical reality. During the interaction with Prof. Hermele, I learned how to appreciate works at the two ends of the spectrum through different angles. Prof. Hermele's open attitude toward different scientific ideas and the sharp understanding of the physics content inspire me a lot and assist me to develop toward scientific independence. Without him, this thesis would not have been possible. Besides, Prof. Hermele has also provided a lot of professional help and advice on writing paper, preparing presentations and finding post-doctoral positions.

Also, I want to thank the wonderful condensed matter group. As a graduate student, I benefit a lot from discussion and collaboration with Prof. Victor Gurarie, Prof. Leo Radzihovsky, Prof. Rahul Nandkishore, Prof. Ana Maria Rey, Prof. Gang Chen, Prof. Andrew Essin, Dr. Hao Song, Dr. Zhaochuan Shen, Dr. Xiao Yin, Sheng-Jie Huang, Han Ma and Abhinav Prem. Particular thanks are due to Prof. Gang Chen, Prof. Victor Gurarie, Prof. Leo Radzihovsky, Prof. Rahul Nandkishore and Prof. Dmitry Reznik for the help on finding post-doctoral positions.

Moreover, I would like to thank Prof. Joel Eaves, Prof. Victor Gurarie, Prof. Ana Maria Rey and Prof. Dmitry Reznik for being in my committee of comprehensive exam and defense.

Finally, I want to express my deep gratitude to my parents and girl friend who always support me no matter how far away I am. Also, I am grateful to all my friends that I have made in Boulder. Thank you all, sincerely.

Contents

Chapter

Tables

Table

Figures

Figure

Chapter 1

Introduction

1.1 General introduction

One of the most important question in physics is: **"What are the quantum phases of matter? "**. The question is not only centrally important for physics but also to move the frontiers of materials science. The band theory successfully characterizes a large family of weakly interacting electron systems and is the underpinning of many advances in the study of semiconductors. The abilities to predict and manipulate semiconductors assists the development of computer era. The study of band theory is one corner of the study of quantum phase of matter where interaction effect can be understood perturbatively. It is interesting to ask: are there quantum phases that cannot be explained using the perturbative picture of the microscopic degrees of freedom? A broad way to rephrase the question is: what kind of quantum emergent phenomena are possible in nature? How to realize those quantum emergent phenomena?

There are two different philosophical concepts in the research of Physics- emergence and reductionism[1]. Condensed matter systems are formed by electrons, protons, and neutrons which are well-understood particles. From the reductionists' point of view, all we need to do to understand condensed matter systems is to find a powerful computer to simulate how all the building blocks interact with each other. The study of condensed matter systems is thus an area with only technical challenges based on the reductionists' view of nature.

However, reductionists' cogent statement is too limited and fails to appreciate the beauty of condensed matter physics. In the highly influential article "More is different" by Philip Anderson[2],

he points out the fallacy of this kind of thinking is the reductionist hypothesis does not imply the ability to start from the microscopic components and reconstruct the macroscopic phenomena. Also, the exact wavefunction with a macroscopic number of quantum particles will be so complicated that it is challenging or even impossible to extract useful information to predict its behavior or to develop possible applications.

In contrast to reductionism, emergence is a concept that takes an entirely different point of view. We might understand how the building blocks in our system very well. However, the complexity of the systems could lead to qualitatively new phenomena which only emerge at the thermodynamic limit. Thus the phenomena are intrinsically many-body phenomena and cannot be understood using its building blocks alone.

Emergent phenomena are ubiquitous in physics. One of the most important concepts- spontaneous symmetry breaking- is an emergent phenomenon. Only when the number of degrees of freedom reaches the thermodynamic limit, the symmetry could be spontaneously broken. The concept of emergence points out quantitative change could lead to qualitative change and can be generalized in different fields of physics[3]. The idea of emergence thus brings immense possibilities to condensed matter systems and becomes the backbone of modern condensed matter physics.

Landau introduced a general theory that describes the phases of matter and the transitions between different phases[4]. The idea behind Landau's theory is to classify different phases of matter according to the global symmetry and the order parameter. Transitions among the various phases are thus the change of symmetry of the order parameters. The order parameter is a local phenomenological quantity that emerges from microscopic degrees of freedom. For example, the crystal phase spontaneously breaks continuous translation symmetry, and the order parameter is a vector defined in a unit cell; the Bose-Einstein condensate is a phase spontaneously breaks particle number conservation $U(1)$ symmetry, and the order parameter is a complex number with modulus 1; the nematic phase spontaneously breaks $SO(3)$ rotational symmetry, and the order parameter is a quadrupolar operator. Such order parameters emerge from the complex interactions between underlying microscopic degrees of freedom. The order parameters for different systems are defined

in various spaces. The order parameter for the crystal phase in 2D is defined in a torus space, the order parameter for Bose-Einstein condensation is defined in S^1, and the order parameter for the nematic phase is defined in RP^2[5].

The Landau theory describes a broad class of matter and forms the cornerstone to understand and to characterize different phases of matter according to its symmetry. One natural question to ask is: are there other scenarios to describe different phases? Are there new phases that cannot be described by Landau theory ? There are various attempts to go beyond the Landau theory. It is reasonable to question the axiom of the existence of the locality of order parameters to find new phases beyond Landau theory. Another possibility is to find new phases that have the same symmetry but have very different physical properties.

The discovery of Berezinskii-Kosterlitz-Thouless(BKT) transition suggests the nontrivial role played by the topology of the system[6, 7, 8]. In a two dimensional system with $U(1)$ symmetry, the Goldstone mode will destroy the spontaneous order and suggest no spontaneous symmetry breaking in such system. However, different asymptotics of correlation functions at high- and low- temperature limits indicate there should be a transition point that separates the two distinct behavior. It turns out such transition is characterized by the proliferation of topological defects, $U(1)$ vortices. The topological defect is characterized by "classical topology." The proliferation of vortices is driven by thermal fluctuations and is of classical nature.

Spontaneously symmetry breaking and the BKT transition are emergent phenomena with a classical interpretation. However, there are emergent phenomena without any classical analogy and must be understood in quantum picture. The main subject of this thesis, topological order, is a quantum emergent phenomena without classical description. F. Wegner invented Ising gauge theory in 1971[9]. The model is a quantum model. The gauge structure of the theory turns the model into a quantum gauge theory. According to Elitzur's theorem, the local symmetry cannot be broken. However, the model still has nontrivial phase diagram with phases that cannot be characterized by a local order parameter. Wegner's theory thus shed much light's on the novel concept of quantum phase transition without local order parameter. One of the key structure for

the Ising gauge theory is the constrained Hilbert space which is non-local. The Hilbert space is non-local in a sense that it cannot be described by direct products of local Hilbert spaces. The basis of the Hilbert space can have a classical interpretation. However, superposition of the basis leads to long-range entangled wave functions. Thus, the Hilbert space is long-range entangled in that sense. Such structure is closely related to the later development of string-net picture[10, 11, 12, 13]. The long-range entangled state is intrinsically quantum state and has no classical analogy.

Many such states share similar behavior that the low energy effective theory is a topological field theory. Therefore, those states are called topological order. During the development, people found symmetry alone is not enough to describe the topological order. The most famous examples for such physics are the chiral spin liquid[14, 15] and fractional quantum Hall effect(FQHE)[16]. Later, people realize chiral spin liquid and FQHE are just tips of the iceberg for a huge class of topological order. From experimental perspectives, FQHE is experimentally measured[16]. However, searching for quantum spin liquids in the lab is still a challenging and ongoing research topic[17, 18].

Now, let's change gear to another line of important but more abstract thinking and discuss how it helps us in studying quantum spin liquids.

The discovery of topological insulator sparks a huge wave of research activities on the study of quantum phases[19, 20, 21, 22, 23, 24, 25, 26, 27]. People realize that topological insulator is just a tip of the iceberg of a huge family of phases which is dubbed symmetry protected topological orders (SPTs)[28, 29, 30, 31, 32, 33, 34, 35, 36, 37]. SPTs are non-trivial phases that are protected by certain symmetries. A topological insulator can be considered as a non-trivial phase protected by time-reversal symmetry. When time reversal symmetry is preserved, the wave function of a topological insulator can not be adiabatically transformed into the wave function of a trivial insulator without closing the bulk gap.

The discovery of topological insulator not only indicates the nontrivial effect of spin-orbit coupling in materials but also raises the interesting question of the interplay among symmetry and topological orders.

The useful idea initiated from the discovery of topological insulator gives new insight to the

study of topological order[38]. The new advances on the line of study of topological order is that symmetry alone can not pin down which topological order it is. However, symmetry divides the parameter space of a topological order such that we have a finer classification for topological order. The topological excitations will carry non-trivial quantum numbers that can distinct the topological order in this finer classification scheme. Thus, symmetries could provide useful experimental signatures to probe the underneath topological order. After imposing symmetry on topological orders, we have more topological orders with different physical properties. Thus, the new topological order is "enriched" from the parent topological order. The new generation of topological order are thus called symmetry enriched topological order(SETs)[39, 40, 41, 42, 43, 44, 45, 46, 47].

The new understanding of SPTs and SETs ignites the study of new quantum phases in the last decade. SPTs and SETs are both macroscopic quantum phases. Both of them have energy gap in the bulk. The energy gap provides a well-defined topological structure. That is, we can change the parameters of the Hamiltonian, as long as the gap is not closed by tuning of parameters, the phase should remain in the same topological phase. Thus, the parameter space of the Hamiltonian is divided into different topological phases. As the Hamiltonian followed a particular path of change of parameters, if the path crosses the boundary of distinct topological phases, the gap closes, and the Hamiltonian could go from one topological phase to the other topological phase. When symmetry is broken, the SPTs will collapse into a trivial product state. On the other hand, the SETs will collapse into a topological order which is still a nontrivial long-range entangled wave function. Specifically, a topological insulator is an SPT protected by time-reversal symmetry and electron number conservation. When time reversal symmetry or electron number conservation is broken, the wave function can be adiabatically connected to product states of atomic orbitals. A Z_2 topological order can be enriched by space group symmetry thus the spinon/vison transform nontrivially under space group. When the symmetry is removed, only the topological structure like fusion and braiding is left and we have a generic Z_2 topological order.

Now, we can get back to the challenge to find the material realization of quantum spin liquids. There are several difficulties to realize quantum spin liquids in experiments. One of the challenges

for seeking quantum spin liquids is the microscopic mechanism for the emergent phenomena is not clear. Exactly solvable models are powerful tools to analyze the properties of topological orders. However, it is laborious or even impossible to relate the results from exactly solvable models to real materials and provide useful experimental predictions. Because of that, the experimentally relevant measurement which can positively identify topological order is lacking. To shed new lights on the problem of how quantum spin liquids emerges from realistic microscopic models, simple models with physical realizations that can be simulated by numerical techniques will be essential. Another major obstacle is the smoking gun evidence of quantum spin liquid. Most experimental measurements are local probes. It is thus tough to devise a probe to extract the global quantum structure.

In this thesis, I will tackle the two issue accordingly. In chapter 2, I would like to strengthen the weak link between theory and material by proposing realistic models in new parameter region of the material- strong spin-orbit coupled 4f and 5d pyrochlores. The new model demonstrates interesting physics from different perspectives. First, it is the minimum model to capture spin-orbit coupling for certain rare earth pyrochlore material. Second, it lies in a sweet spot that interesting theoretical proposal can be tested by unbiased large-scale quantum Monte Carlo simulation. The advantage of this model puts itself in a good position to study three dimension long range entangled quantum states. Because of the general symmetry argument, it could be relevant to realize topological insulator for 5d transition metal compounds in the future. In chapter 3, I would like to connect the newly developed theoretical concepts to a closely related model by proposing signals that can be measured by numerical simulation and potentially can be measured in future experiments. In chapter 4, I will discuss the work I collaborate with a local experiment group to construct a theoretical model to understand the Raman scattering experiment in Sr_2IrO_4. The spin-orbit coupling leads to different selection rules that reveal the possible microscopic dynamics in this material.

In summary, this thesis explores how novel quantum orders emerge from strong spin-orbit coupling in materials. Through the understanding of spin-orbit coupling and symmetry, we can

identify the unique response to probe new quantum orders or the possible microscopic dynamics from the experiment.

1.2 Quantum spin ices and topological phases from dipolar-octupolar doublets on the pyrochlore lattice [1]

We consider a class of d- and f-electron systems in which dipolar-octupolar Kramers doublets arise on the sites of the pyrochlore lattice. For such doublets, two components of the pseudospin transform like a magnetic dipole, while the other transforms like a component of the magnetic octupole tensor. Based on a symmetry analysis, we construct and study models of dipolar-octupolar doublets in itinerant and localized limits. In both limits, the resulting models are of surprisingly simple form. In the itinerant limit, we find topological insulating behavior. In the localized limit, the most general nearest-neighbor spin model is the XYZ model. We show that this XYZ model exhibits **two distinct** quantum spin ice (QSI) phases, that we dub dipolar QSI, and octupolar QSI. We conclude with a discussion of potential relevance to real material systems.

1.3 Theory of quantum Kagome ice and vison zero modes[2]

We derive an effective Z_2 gauge theory to describe the quantum kagome ice (QKI) state that has been observed by Carrasquilla **et. al.** in Monte Carlo studies of the $S = 1/2$ kagome XYZ model in a Zeeman field[50]. The numerical results on QKI are consistent with, but do not confirm or rule out, the hypothesis that it is a Z_2 spin liquid. Our effective theory allows us to explore this hypothesis and make a striking prediction for future numerical studies, namely that symmetry-protected vison zero modes arise at lattice disclination defects, leading to a Curie defect term in the spin susceptibility, and a characteristic $(N_{dis} - 1)\ln 2$ contribution to the entropy, where N_{dis} is the number of disclinations. Only the Z_2 Ising symmetry is required to protect the

[1] This section has been published as a portion of Yi-Ping Huang, Gang Chen, Michael Hermele, Phys. Rev. Lett. 112, 167203,[48] copyright 2014 American Physical Society, and is reproduced here in accord with the copyright policies of the American Physical Society.

[2] This section has been published as a portion of Yi-Ping Huang and Michael Hermele, Phys. Rev. B 95, 075130,[49] copyright 2017 American Physical Society, and is reproduced here in accord with the copyright policies of the American Physical Society.

vison zero modes. This is remarkable because a unitary Z_2 symmetry cannot be responsible for symmetry-protected degeneracies of local degrees of freedom. We also discuss other signatures of symmetry fractionalization in the Z_2 spin liquid, and phase transitions out of the Z_2 spin liquid to nearby ordered phases.

1.4 High-energy electronic excitations in Sr_2IrO_4 observed by Raman scattering [3]

Spin-orbit interaction in Sr_2IrO_4 leads to the realization of the $J_{\text{eff}} = 1/2$ state and also induces an insulating behavior. Using large-shift Raman spectroscopy, experimentalists found two high-energy excitations of the d-shell multiplet at 690 meV and 680 meV with A_{1g} and B_{1g} symmetry respectively. As temperature decreases, the A_{1g} and B_{1g} peaks narrow, and the A_{1g} peak shifts to higher energy while the energy of the B_{1g} peak remains the same. We show that both pseudospin-flip and non-pseudosin-flip dd electronic transitions are Raman active, but only the latter are observed. Our analysis and experiments place significant new constraints on the possible electronic structure of Sr_2IrO_4.

[3] This section has been published as a portion of Jhih-An Yang, Yi-Ping Huang, Michael Hermele, Tongfei Qi, Gang Cao, and Dmitry Reznik, Phys. Rev. B 91, 195140,[51] copyright 2015 American Physical Society, and is reproduced here in accord with the copyright policies of the American Physical Society.

Chapter 2

Quantum spin ices and topological phases from dipolar-octupolar doublets on the pyrochlore lattice [1]

2.1 Introduction

Finding new phases of matter is a problem of fundamental importance in condensed matter physics. This search motivates in part the exploration of new classes of materials, where novel parameter regimes can lead to phases not realized elsewhere, and other new phenomena. Recently, there has been intense interest in materials combining strong spin-orbit coupling (SOC) with substantial electron correlation, especially in compounds with heavy elements [52]. SOC entangles the spin and orbital degrees of freedom, and microscopic models including SOC have in many cases not yet been constructed and studied. Spin-orbital entanglement can lead to rather complicated models, but this need not always be the case.

In this chapter, we study a class of systems where strong SOC leads to surprisingly simple microscopic models that – in different limits – naturally realize not only a topological band insulator, but also **two distinct** quantum spin ice (QSI) phases. One of these is the familiar QSI phase [53, 54], here dubbed **dipolar** QSI (dQSI), while the other is a novel **octupolar** QSI (oQSI). dQSI and oQSI are two distinct symmetry enriched U(1) quantum spin liquids, with space group symmetry playing the crucial role.

Much of the recent activity in strong-SOC systems has focused on $5d$ iridates and $4f$ py-

[1] This chapter has been published as a portion of Yi-Ping Huang, Gang Chen, Michael Hermele, Phys. Rev. Lett. 112, 167203,[48] copyright 2014 American Physical Society, and is reproduced here in accord with the copyright policies of the American Physical Society.

rochlores. Various novel models and phases have been predicted for iridates with pyrochlore [55, 56, 57, 58, 59, 60], hyperkagome[61, 62, 63, 64, 65, 66], honeycomb[67] and hyperhoneycomb lattices[68, 69], while the dQSI phase has been predicted in $4f$ pyrochlores[70, 71, 72, 73, 74]. In many of these systems, SOC and other interactions lead to Kramers doublets on the d or f ions, which in turn are the building blocks for minimal effective models to capture the low-energy physics. Any Kramers doublet is associated with a time-reversal odd pseudospin operator τ^μ ($\mu = x, y, z$), but not all Kramers doublets transform identically under space group symmetry [75]. The most familiar possibility, which holds in the above recently studied $4f$ and $5d$ systems, is that, just like a true spin-1/2 moment, τ^μ transforms as a magnetic dipole (**i.e.** as a pseudovector) under space group operations.

In this chapter, focusing on the pyrochlore lattice of corner-sharing tetrahedra, we consider a class of systems with Kramers doublets arising from d or f ions, where (in suitable local coordinates discussed below) τ^z and τ^x both transform like the z-component of a magnetic dipole, while τ^y transforms as a component of the magnetic octupole tensor. Models of such dipolar-octupolar (DO) doublets have striking properties in both weak and strong correlation limits. We note that a similar type of Kramers doublet has been considered on other lattices[76, 77].

More specifically we consider both $A_2B_2O_7$ pyrochlores and AB_2O_4 spinels, where the pyrochlore A-site, and B-sites in both families, form a pyrochlore lattice. We consider two principal situations: (1) In both pyrochlores and spinels, B is a transition metal in d^1 or d^3 electron configuration and A is non-magnetic. (2) In pyrochlores, A is a trivalent rare earth with a partially filled $4f$ shell, and B is non-magnetic. Both cases can lead to effective models of DO doublets on the pyrochlore lattice.

Case (1)**.** The magnetic ions reside at the center of a trigonally-distorted oxygen octahedron; the single-ion physics has been treated **e.g.** in [75]. Due to the cubic crystal field only the t_{2g} manifold is relevant. Projection $\mathcal{P}$ of orbital angular momentum $\boldsymbol{L}$ into the t_{2g} manifold is $\mathcal{P}\boldsymbol{L}\mathcal{P} =$

$-\boldsymbol{\ell}$, where the ℓ^μ are spin-1 matrices. The single-site Hamiltonian within the t_{2g} manifold is

$$H = -\lambda\, \boldsymbol{\ell} \cdot \boldsymbol{S} + H_{\text{tri}} + H_{\text{int}}, \tag{2.1}$$

with λ the strength of SOC and $\boldsymbol{S}$ the spin operator. $H_{\text{tri}} = \Delta_3 (\ell^{z_i})^2$ is the trigonal crystal field allowed by D_{3d} site symmetry. The z_i-axis is the local C_3 axis ($i = 1, \ldots 4$ is the sublattice index), and x_i, y_i-axes are specified in the section 2.3. The interaction H_{int} is of Kanamori form, and is treated in the atomic limit where it is characterized by Hubbard interaction U and Hund's coupling J_H (see section 2.2).

Defining an effective total angular momentum $\boldsymbol{j}_{\text{eff}} = \boldsymbol{\ell} + \boldsymbol{S}$, SOC alone splits the t_{2g} manifold into an upper doublet ($j_{\text{eff}} = 1/2$) and lower quadruplet ($j_{\text{eff}} = 3/2$). Effective models of $j_{\text{eff}} = 1/2$ doublets are relevant for $5d^5$ iridates [78, 79] and have received significant attention[61, 55, 67, 59, 68, 69]. While the $j_{\text{eff}} = 1/2$ doublet is dipolar, it does not obey a naïve Heisenberg exchange model due to strong SOC [77, 80].

The trigonal crystal field H_{tri} splits the quadruplet into two Kramers doublets, for a total of three doublets. If $\Delta_3 > 0$, the lower and upper doublets are dipolar and transform as the Γ_4^+ irreducible representation of the D_{3d} double group [81]. The middle doublet is a DO doublet; it has $j_{\text{eff}}^{z_i} = \pm 3/2$, and transforms as $\Gamma_5^+ \oplus \Gamma_6^+$ (Fig. 2.1). The doublet is half-filled for d^3 electron configuration, or (if $\Delta_3 < 0$) for d^1 configuration.

While Hubbard interaction does not affect the single-site energy spectrum for a fixed number of electrons, Hund's coupling plays an important role. When $\Delta_3 > 0$, we find the d^3 ground state multiplet remains a DO doublet even for large J_H (see section 2.2). However, as J_H increases, the energy gap between the ground state and the dipolar doublet first excited state decreases, vanishing in the limit of large J_H where we recover a spin-3/2 moment. The splitting between the ground and first excited doublets is substantial only when $J_H \lesssim \lambda$, and increases with Δ_3/λ (see section 2.2). Hund's coupling has no effect for d^1 configuration.

Case (2). Here A is a trivalent rare earth, where the ground state has angular momentum J. The D_{3d}-symmetric crystal field Hamiltonian is $H_{\text{cf}} = 3B_2^0 (J^z)^2 + \cdots$ [82]. If $J = 9/2$ or $15/2$,

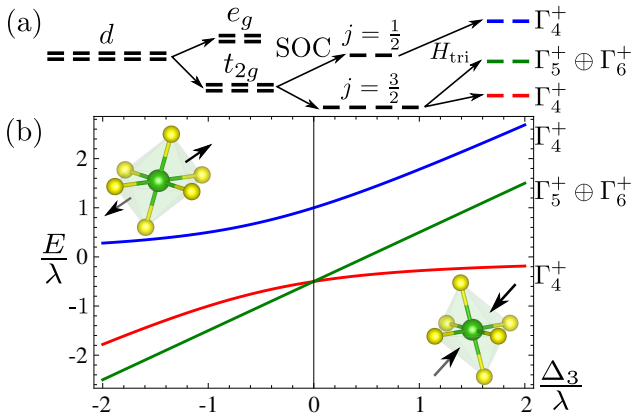

Figure 2.1: (Color online.) (a) The evolution of d electron states under cubic crystal field, SOC and trigonal distortion. (b) The energies for the three local doublets under different trigonal distortions. Compression (elongation) along the C_3 axis corresponds to $\Delta_3 > 0$ ($\Delta_3 < 0$).

and $B_2^0 < 0$ and dominates the other crystal field terms, then the ground state is a DO doublet with $J^z = \pm J$, transforming as $\Gamma_5^+ \oplus \Gamma_6^+$ under D_{3d} site symmetry. The DO doublet nature of the ground state is robust even when the other crystal field terms are appreciable, as long as the ground state is adiabatically connected to the $J^z = \pm J$ doublet. Among the lanthanides, only Nd^{3+}, Dy^{3+} and Er^{3+} have the required values of J. Of these, $B_2^0 < 0$ only for Nd^{3+} and Dy^{3+} [82]. Indeed, the crystal field ground state of Nd^{3+} in $Nd_2Ir_2O_7$ is a DO doublet [83], and a DO doublet ground state is predicted for Dy^{3+} in $Dy_2Ti_2O_7$[84].

The action of $Fd\bar{3}m$ space group symmetry on DO doublets is given in the supplementary material (see section 2.6). The D_{3d} site symmetry is generated by a 3-fold rotation C_3, a mirror plane M, and inversion $\mathcal{I}$, with: $C_3 : \tau^\mu \to \tau^\mu$, $M : \tau^{x,z} \to -\tau^{x,z}$, $M : \tau^y \to \tau^y$, and $\mathcal{I} : \tau^\mu \to \tau^\mu$. These transformations are not those of a pseudovector, and imply that $\tau^{x,z}$ transform like the z_i-component of a magnetic dipole, while τ^y transforms like a component of the magnetic octupole tensor (see section 2.6).

We now proceed to construct effective models using a single DO doublet on each pyrochlore lattice site as the basic building block. We assume throughout that higher-energy on-site degrees of freedom can be ignored. Even when this is not quantitatively accurate, our models may still be valid as minimal low-energy effective models.

We consider limits of itinerant and localized electrons, constructing tight-binding and spin Hamiltonians, respectively, in the two limits. The Hamiltonian contains all electron hopping terms (itinerant limit) or spin exchange terms (localized limit) allowed by time reversal and $Fd\bar{3}m$ space group symmetry, up to a given spatial range. We note that tight-binding and exchange models of dipolar Γ_4^+ doublets have been extensively studied in the context of iridate and rare-earth pyrochlores[85, 55, 86, 59, 60, 73, 72].

In the itinerant limit we ignore electron interactions, and the general form of the model is

$$H_{TB} = \sum_{(\boldsymbol{r},\boldsymbol{r}')} \left[c_{\boldsymbol{r}}^\dagger T_{\boldsymbol{r}\boldsymbol{r}'} c_{\boldsymbol{r}} + h.c. \right]. \tag{2.2}$$

Here, $\boldsymbol{r}$ labels pyrochlore lattice sites, the sum is over all pairs of sites, and $c_{\boldsymbol{r}}^T = (c_{\boldsymbol{r}+}, c_{\boldsymbol{r}-})$.

$T_{\boldsymbol{r}\boldsymbol{r}'} = T^\dagger_{\boldsymbol{r}'\boldsymbol{r}}$ is a 2×2 matrix describing tunneling between sites $\boldsymbol{r}$ and $\boldsymbol{r}'$. The operator $c^\dagger_{\boldsymbol{r}\pm}$ creates an electron at site $\boldsymbol{r}$ with $j^{z_i}_{\text{eff}} = \pm 3/2$ in case (1), or $J^{z_i} = \pm J$ in case (2). Pseudospin operators are $\tau^\mu_{\boldsymbol{r}} = (1/2) c^\dagger_{\boldsymbol{r}} \sigma^\mu c_{\boldsymbol{r}}$, where σ^μ are the Pauli matrices. Time reversal symmetry implies $T_{\boldsymbol{r}\boldsymbol{r}'} = t^0_{\boldsymbol{r}\boldsymbol{r}'} + i t^\mu_{\boldsymbol{r}\boldsymbol{r}'} \sigma^\mu$.

For nearest-neighbor sites, the hopping matrix $T_{\boldsymbol{r}\boldsymbol{r}'}$ has a remarkably simple form. Choosing an appropriate orientation of bonds (see section 2.4.2), we find $T_{\boldsymbol{r}\boldsymbol{r}'} = i[t^1_{nn}\sigma^1 + t^3_{nn}\sigma^3]$, **taking the same form for all nearest-neighbor bonds**. A global rotation about the y-axis in pseudospin space can thus eliminate t^1_{nn}, leading to $\tilde{T}_{\boldsymbol{r},\boldsymbol{r}'} = i\tilde{t}^3_{nn}\sigma^3$, where the tilde indicates we are working in the transformed basis. The nearest-neighbor model thus has a U(1) spin symmetry, and the purely imaginary (spin-dependent) hopping is similar to models considered in [87]. A highly unstable Fermi surface coincides with a surface of intersection between two bands (see section 2.4.2).

Evidently the nearest-neighbor tight-binding model is highly fine-tuned, so we also include second-neighbor hopping, which is specified by parameters $(\tilde{w}_0, \tilde{w}_x, \tilde{w}_z)$ (see section 2.4.2). Second-neighbor hopping breaks the U(1) spin symmetry and gaps out most of the nearest-neighbor Fermi surface. One finds either a metallic state, or a semi-metal with isolated band touchings occurring at the W points (see Fig. 2.2). These W-point touchings are in fact unstable and are gapped out by fourth-neighbor hopping, leading to a strong topological band insulator (see section 2.4.2).

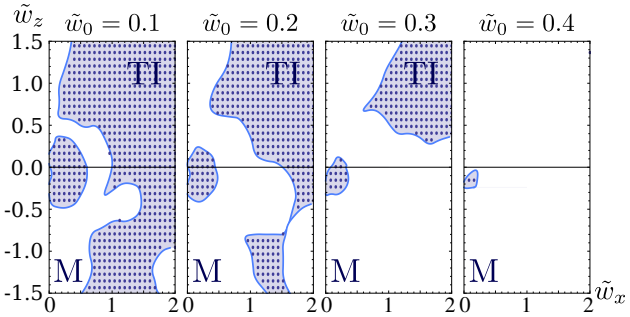

Figure 2.2: Phase diagram of the tight-binding model wtih first- and second-neighbor hopping, as a function of $(\tilde{w}_0, \tilde{w}_x, \tilde{w}_z)$, setting $\tilde{t}^3_{nn} = 1$. Very small fourth-neighbor hopping is included to remove unstable band touchings at the W-point. Metallic (M) and strong topological insulator (TI) phases are found. The phase diagram is symmetric under $\tilde{w}_x \to -\tilde{w}_x$ and $\tilde{w}_0 \to -\tilde{w}_0$.

We now consider the large-U limit of localized electrons, where the degrees of freedom are the

pseudospin-1/2 moments $\tau^{\mu}_{\boldsymbol{r}}$. We find that the most general symmetry allowed nearest-neighbor exchange is $H_{ex} = \sum_{\langle \boldsymbol{r}\boldsymbol{r}'\rangle}[J_x\tau^x_{\boldsymbol{r}}\tau^x_{\boldsymbol{r}'} + J_y\tau^y_{\boldsymbol{r}}\tau^y_{\boldsymbol{r}'} + J_z\tau^z_{\boldsymbol{r}}\tau^z_{\boldsymbol{r}'} + J_{xz}(\tau^x_{\boldsymbol{r}}\tau^z_{\boldsymbol{r}'} + \tau^z_{\boldsymbol{r}}\tau^x_{\boldsymbol{r}'})]$, where the sum is over nearest-neighbor bonds. Quite remarkably, the exchange is identical in form on every bond. Similar to the itinerant limit, the J_{xz} term can be eliminated by a global pseudospin rotation (see section 2.4.1). After this transformation, the exchange is of the remarkably simple XYZ form:

$$H_{\mathrm{XYZ}} = \sum_{\langle \boldsymbol{r}\boldsymbol{r}'\rangle} \tilde{J}_x\tilde{\tau}^x_{\boldsymbol{r}}\tilde{\tau}^x_{\boldsymbol{r}'} + \tilde{J}_y\tilde{\tau}^y_{\boldsymbol{r}}\tilde{\tau}^y_{\boldsymbol{r}'} + \tilde{J}_z\tilde{\tau}^z_{\boldsymbol{r}}\tilde{\tau}^z_{\boldsymbol{r}'}. \tag{2.3}$$

This result should be contrasted with the case of dipolar doublets on the pyrochlore lattice, where the form of nearest-neighbor exchange varies according to the orientation of each bond [71].

Beyond simplicity of form, this pyrochlore XYZ model supports two distinct QSI phases. To see this, we first review the XXZ model ($\tilde{J}_\perp \equiv \tilde{J}_x = \tilde{J}_y$), where QSI was identified in a study of the regime $\tilde{J}_z > 0$, $\tilde{J}_z \gg |\tilde{J}_\perp|$ [53]. For simplicity we concentrate on $\tilde{J}_\perp < 0$, where quantum Monte Carlo [88] found QSI for $|\tilde{J}_\perp|/\tilde{J}_z < c$, with $c \approx 0.1$. When $|\tilde{J}_\perp|/\tilde{J}_z > c$, magnetic order is present. It is important to note that QSI is robust to arbitrary symmetry breaking perturbations, and thus survives away from the XXZ line.

The physics of QSI can be understood by mapping to a compact U(1) gauge theory, which is exact for large $\tilde{J}_z$ [53]. The centers of pyrochlore lattice tetrahedra $\mathbf{r}$ form a diamond lattice, and each pyrochlore site $\boldsymbol{r}$ corresponds to a unique nearest-neighbor diamond link $(\mathbf{r}, \mathbf{r}')$. We introduce lattice vector fields $E_{\mathbf{r}\mathbf{r}'} = \tilde{\tau}^z_{\boldsymbol{r}}$ and $e^{iA_{\mathbf{r}\mathbf{r}'}} = \tilde{\tau}^x_{\boldsymbol{r}} + i\tilde{\tau}^y_{\boldsymbol{r}}$, where $\mathbf{r}$ ($\mathbf{r}'$) lies in the diamond A (B) sublattice, and $E_{\mathbf{r}\mathbf{r}'} = -E_{\mathbf{r}'\mathbf{r}}$, $A_{\mathbf{r}\mathbf{r}'} = -A_{\mathbf{r}'\mathbf{r}}$. E (A) can be interpreted as the electric field (vector potential) of a compact U(1) lattice gauge theory, of which QSI is the deconfined phase, supporting a gapless photon, and gapped electric charge and magnetic monopole excitations.

So far we have been describing dQSI, so named because the electric field $E_{\mathbf{r}\mathbf{r}'} = \tilde{\tau}^z_{\boldsymbol{r}}$ is a magnetic dipole. In the low-energy continuum theory, the electric field is odd under time reversal and transforms under the Γ_4^+ (pseudovector) representation of the O_h point group. [The magnetic field is time reversal even, and transforms under the Γ_4^- (vector) representation.] The same dQSI phase occurs for large $\tilde{J}_x > 0$ ($\tilde{J}_{y,z} < 0$ for simplicity), where $E_{\mathbf{r}\mathbf{r}'} = \tilde{\tau}^x_{\boldsymbol{r}}$, which transforms identically

to $\tilde{\tau}^z_{\boldsymbol{r}}$ under symmetry.

The novel oQSI phase arises for $\tilde{J}_y > 0$ large ($\tilde{J}_{x,z} < 0$ for simplicity), so that $E_{\mathbf{r}\mathbf{r}'} = \tilde{\tau}^y_{\boldsymbol{r}}$. In this case the electric field is purely octupolar. In the continuum theory, the electric field is still time reversal odd, but transforms under the Γ_5^+ representation of O_h (neither vector nor pseudovector). The magnetic field transforms as Γ_5^-.

oQSI and dQSI are thus distinguished by the action of space group symmetry on electric and magnetic fields, and can be viewed as distinct symmetry enriched U(1) quantum spin liquids. This means that dQSI and oQSI are distinct phases in the presence of space group symmetry, but weak space-group-breaking perturbations take dQSI and oQSI into the same U(1) quantum spin liquid phase (which is robust to arbitrary weak perturbations regardless of symmetry). In terms of physical properties, dQSI and oQSI both have a T^3 contribution to specific heat from gapless photons; in f-electron realizations, this is expected to be about 1000 times the phonon contribution [72]. Dipolar spin correlations, as measured **e.g.** by neutron scattering, will, however, be quite different, as illustrated by the fact that, neglecting effects of long-range dipolar interaction, equal-time dipolar correlations fall off as $1/r^4$ in dQSI [53], but as $1/r^8$ in oQSI (see section 2.7). In future work, it would be interesting to compare the dynamic spin structure factor in dQSI and oQSI. Neutron scattering signatures of dQSI have been discussed in [72].

So far, we have avoided discussing the case $\tilde{J}_\perp > 0$; here, less is known for the XXZ model, due to the presence of a sign problem in quantum Monte Carlo. In the $|\tilde{J}_\perp|/\tilde{J}_z \ll 1$ limit, $\tilde{J}_\perp$ favors QSI with π flux of the vector potential $A_{\mathbf{r}\mathbf{r}'}$ through each pyrochlore hexagon, unlike for $\tilde{J}_\perp < 0$, where zero flux is favored (see section 2.8). We have not considered the properties of the resulting π-flux versions of dQSI and oQSI, leaving this for future work. QSI is expected to persist over a larger range of $\tilde{J}_\perp > 0$, since in this case both $\tilde{J}_z$ and $\tilde{J}_\perp$ interactions are frustrated [73].

We now discuss the phase diagram of the XYZ model. The simplest magnetically ordered phases appear ferromagnetic in local coordinates; for instance, if $\tilde{J}_z < 0$ and is dominant, $\langle \tilde{\tau}^z_{\boldsymbol{r}} \rangle = m_d \neq 0$. This is the "all-in-all-out" (AIAO) state, where dipoles point along the local z_i axes, toward (away from) pyrochlore tetrahedron centers lying in the diamond A (B) sublattices (or vice

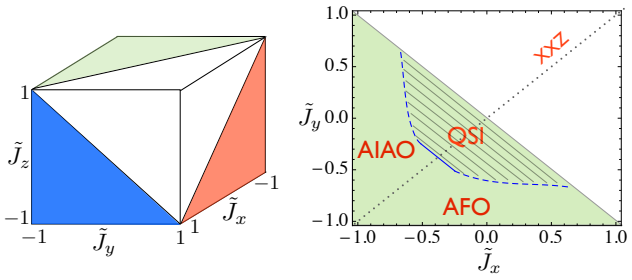

Figure 2.3: (Color online). Left: Unit cube in $(\tilde{J}_x, \tilde{J}_y, \tilde{J}_z)$ parameter space of the XYZ model. Shaded regions were analyzed via gMFT. Right: gMFT phase diagram on the $\tilde{J}_z = 1$ surface of the cube, where dQSI, all-in-all-out (AIAO), and anti-ferro-octupolar (AFO) phases are found. Within gMFT, the phase transition is 1st order (2nd order) at the dashed (solid) boundary. The dotted line is the XXZ line. We did not apply gMFT for $\tilde{J}_x + \tilde{J}_y \geq 0$. There, the exchange is frustrated, and QSI is likely to be more stable than for $\tilde{J}_x + \tilde{J}_y < 0$ [73]. The phase diagram on the other surfaces of the cube can be obtained by relabeling parameters, with the nature of phases changing according to the anisotropic character of $\tilde{\tau}^{\mu}_{\boldsymbol{r}}$. dQSI occurs on the $\tilde{J}_z = 1$ and $\tilde{J}_x = 1$ faces, while oQSI occurs on the $\tilde{J}_y = 1$ face.

versa). Since τ^z and τ^x transform identically under space group, the same AIAO state arises when $\tilde{J}_x < 0$, $|\tilde{J}_x| \gg \tilde{J}_{y,z}$. A distinct magnetically ordered phase, with $\langle \tilde{\tau}^y_{\boldsymbol{r}} \rangle = m_o \neq 0$, is obtained when $\tilde{J}_y < 0$, $|\tilde{J}_y| \gg \tilde{J}_{x,z}$. This state has anti-ferro-octupolar order, and no on-site dipolar order.

To study the phase diagram away from the simple limits discussed above, we employ gauge mean field theory (gMFT)[72, 73] to our model (see section 2.8). gMFT makes the U(1) gauge structure explicit via a slave particle construction, and is capable of describing both QSI and magnetic phases. For simplicity, we limited our analysis to the shaded regions shown (Fig. 2.3) on the faces of a cube in $(\tilde{J}_x, \tilde{J}_y, \tilde{J}_z)$ space. We find only the two QSI and magnetically ordered phases discussed above. In the same regions of parameter space we analyzed via gMFT, the XYZ model can be studied via quantum Monte Carlo without a sign problem (see section 2.8).

We now comment on the prospects for applying the models discussed above to real materials. Promising systems to realize the XYZ model are $Nd_2B_2O_7$ pyrochlores. B = Zr, Sn compounds are insulators exhibiting antiferromagnetic order at low temperature [89, 90]. While the B = Ir compound is known to carry a DO doublet [83], the physics is complicated by the presence of Ir conduction electrons[58]. Synthesis of other Nd pyrochlores has been reported [91]. The validity of the XYZ model description could be ascertained and the exchange couplings measured directly via neutron scattering in applied magnetic field, as was done in the dipolar case for $Yb_2Ti_2O_7$ [92]. DO doublets are likely in Dy pyrochlores [84], but the large moment of Dy^{3+} means dipolar interactions must be included. DO doublets may also occur in B-site rare earth spinels, and there is evidence for this in $CdEr_2Se_4$ [93]. More broadly, strongly localized d-electron Mott insulators with $S = 3/2$ and D_{3d} site symmetry comprise another class of systems where DO doublets may be the low-energy degrees of freedom.

$5d$ systems are a likely setting for itinerant (or weakly localized) DO doublets. $Cd_2Os_2O_7$, believed to exhibit AIAO order below a finite-temperature metal-insulator transition[94, 95], has Os^{3+} in $5d^3$ configuration. Microscopic calculations indicate a DO doublet ground state, but show a very small splitting between ground and first excited doublets [96], likely due to Hund's coupling. Moreover, electronic structure calculations do not show a clear separation between DO doublet and

other energy bands [97, 98]. Thus $5d^1$ systems, perhaps on other lattices, may be more promising for the realization of itinerant DO doublets.

In summary, we have pointed out that Kramers doublets with dipolar-octupolar character can arise on the sites of the pyrochlore lattice in both d- and f-electron systems. We studied effective models of DO doublets in itinerant and localized limits, finding topological insulation in the former case, and two distinct quantum spin ice phases in the latter.

2.2 On-site interaction for d^3 electron configuration

As discussed in the main text, for d^3 electron configuration, the on-site interaction plays an important role and must be included. For a fixed lattice site, the interaction $H_{\rm int}$ projected into the t_{2g} manifold is of Kanamori form,

$$\begin{aligned} H_{\rm int} &= \frac{U}{2}\sum_{m}\sum_{\sigma\neq\sigma'} d^\dagger_{m\sigma}d^\dagger_{m\sigma'}d_{m\sigma'}d_{m\sigma} \\ &+ \frac{U'}{2}\sum_{m\neq m'}\sum_{\sigma,\sigma'} d^\dagger_{m\sigma}d^\dagger_{m'\sigma'}d_{m'\sigma'}d_{m\sigma} \\ &+ \frac{J}{2}\sum_{m\neq m'}\sum_{\sigma,\sigma'} d^\dagger_{m\sigma}d^\dagger_{m'\sigma'}d_{m\sigma'}d_{m'\sigma} \\ &+ \frac{J'}{2}\sum_{m\neq m'}\sum_{\sigma,\sigma'} d^\dagger_{m\sigma}d^\dagger_{m\sigma'}d_{m'\sigma'}d_{m'\sigma}. \end{aligned} \tag{2.4}$$

Here, $d^\dagger_{m\sigma}$ creates an electron in the t_{2g} orbital labeled by $m = 1, 2, 3$, with spin $\sigma = \uparrow, \downarrow$, and U, U', J, J' are the Kanamori parameters. For simplicity, we take the atomic limit by setting $U = U' + J + J'$ and $J = J' \equiv J_H$, where J_H is the Hund's coupling.

We have assessed the effect of on-site interaction by direct diagonalization of the on-site Hamiltonian [Eq. (1) in the main text], including spin-orbit coupling λ, trigonal crystal field splitting Δ_3, as well as the interaction parameter J_H. For a fixed number of electrons, the Hubbard interaction U has no effect and can be neglected. In Fig. 2.4a, the energy spectrum is plotted as a function of J_H/λ for $\Delta_3 = \lambda$. The ground state is a DO doublet, and the first excitation is a dipolar doublet; we denote the splitting between these levels by δ. Independent of J_H, we find that the DO doublet remains the ground state ($\delta > 0$), but δ/λ becomes small for $J_H \gtrsim \lambda$, as large

J_H favors a $S = 3/2$ ground state. The splitting δ is plotted in Fig. 2.4b for different values of Δ_3/λ; it is apparent that larger trigonal splitting leads to larger separation between the two lowest doublets.

2.3 Lattice geometry

The pyrochlore lattice is a FCC lattice with four-site basis. Setting the FCC lattice constant to unity, we choose the FCC primitive vectors to be

$$\begin{aligned} \boldsymbol{a}_1 &= \frac{1}{2}(0,1,1) \\ \boldsymbol{a}_2 &= \frac{1}{2}(1,0,1) \\ \boldsymbol{a}_3 &= \frac{1}{2}(1,1,0). \end{aligned} \tag{2.5}$$

The basis vectors are taken to be

$$\boldsymbol{b}_i = -\frac{\sqrt{3}}{8}\hat{z}_i, \tag{2.6}$$

where $\hat{z}_i$ is defined below, and $i = 1, \ldots, 4$ is the sublattice index. The pyrochlore lattice can be viewed as composed of corner-sharing tetrahedra whose centers form a diamond lattice. The A-sublattice diamond sites are $\{\boldsymbol{R}\}$, and the B-sublattice sites are $\{\boldsymbol{R} + \frac{1}{4}(1,1,1)\}$, where $\boldsymbol{R}$ is an arbitrary FCC Bravais lattice vector. The basis vectors themselves form the A-sublattice tetrahedron centered at the origin. In the following we will use serif symbol r, r' to label the sites on the dual diamond lattice and $\boldsymbol{r}, \boldsymbol{r}'$ to label the sites on the pyrochlore lattice. Pyrochlore sites are also labeled by the pair $(\boldsymbol{R}, i)$, where $\boldsymbol{r} = \boldsymbol{R} + \boldsymbol{b}_i$.

It is convenient to introduce local coordinate systems for each sublattice. These are given by unit vectors $(\hat{x}_i, \hat{y}_i, \hat{z}_i)$ defined as follows,

$$\begin{aligned} \hat{z}_1 &= \frac{1}{\sqrt{3}}(1,1,1) & \hat{y}_1 &= \frac{1}{\sqrt{2}}(0,1,-1), \\ \hat{z}_2 &= \frac{1}{\sqrt{3}}(1,-1,-1) & \hat{y}_2 &= \frac{1}{\sqrt{2}}(-1,0,-1), \\ \hat{z}_3 &= \frac{1}{\sqrt{3}}(-1,1,-1) & \hat{y}_3 &= \frac{1}{\sqrt{2}}(-1,-1,0), \\ \hat{z}_4 &= \frac{1}{\sqrt{3}}(-1,-1,1) & \hat{y}_4 &= \frac{1}{\sqrt{2}}(-1,1,0), \end{aligned} \tag{2.7}$$

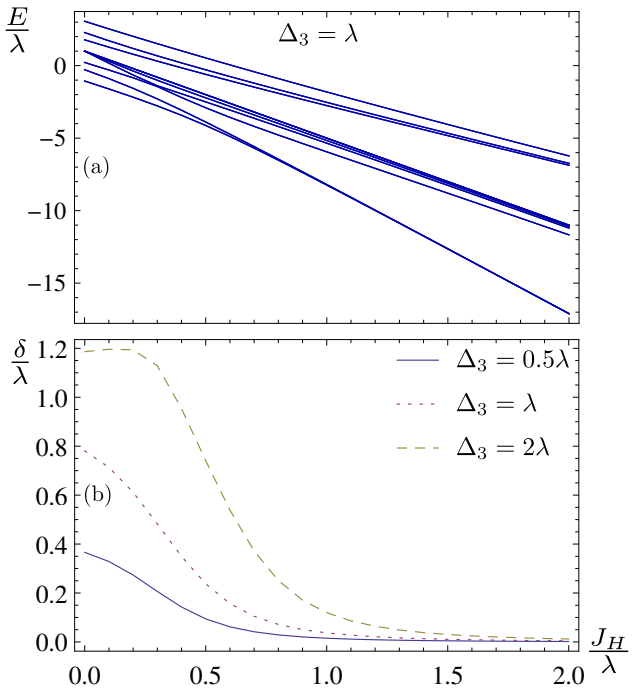

Figure 2.4: (a) The energy spectrum of the single-site Hamiltonian for d^3 electron configuration, as a function of J_H/λ at $\Delta_3 = \lambda$. (b) Plot of the splitting δ between the first excited and ground doublets as a function of J_H/λ for three different values of Δ_3/λ.

and $\hat{x}_i \equiv \hat{y}_i \times \hat{z}_i$. $\hat{z}_i$ the local 3-fold axis of the D_{3d} site symmetry, and points toward the center of the A-sublattice tetrahedra.

2.4 Symmetry analysis

2.6

The $Fd\bar{3}m$ space group is generated by the following operations: (1) Symmetries of the tetrahedron centered at $\mathbf{r} = 0$, forming the group T_d. (2) Inversion $\mathcal{I}$ about the site $\boldsymbol{r} = \boldsymbol{b}_1$. (3) Primitive FCC translations $T_{\boldsymbol{a}_1}, T_{\boldsymbol{a}_2}, T_{\boldsymbol{a}_3}$. We also consider time reversal symmetry $\mathcal{T}$.

The T_d group preserving the $\mathbf{r} = 0$ tetrahedron is generated by $C_{3,1}$ and $M_{x\bar{y}}$. Here, $C_{3,1}$ is a 3-fold rotation preserving the site $\boldsymbol{r} = \boldsymbol{b}_1$, and $M_{x\bar{y}}$ is a mirror reflection sending $x \leftrightarrow -y$. Explicitly,

$$C_{3,1} : \boldsymbol{r} \to C_{3,1}\boldsymbol{r} \equiv \begin{pmatrix} 0 & 0 & 1 \\ 1 & 0 & 0 \\ 0 & 1 & 0 \end{pmatrix} \boldsymbol{r}, \tag{2.8}$$

and

$$M_{x\bar{y}} : \boldsymbol{r} \to M_{x\bar{y}}\boldsymbol{r} \equiv \begin{pmatrix} 0 & -1 & 0 \\ -1 & 0 & 0 \\ 0 & 0 & 1 \end{pmatrix} \boldsymbol{r}. \tag{2.9}$$

Below, we work out the effect of these symmetries on DO doublets, first for the simpler case of localized pseudospins, then for the case of itinerant electrons in DO doublets.

2.4.1 Localized case

For concreteness, we begin by considering f-electron magnetic moments on the sites of the pyrochlore lattice, with total angular momentum $J = 3/2, 9/2, 15/2$. We suppose that crystal field splitting leads to a ground state DO doublet, with the **same symmetry** as the doublet $J^{z_i} = \pm J$. (Note that we do **not** assume the ground state doublet is exactly given by $J^{z_i} = \pm J$, only that it transforms identically under symmetry.) Letting $\mathcal{P}$ project onto the $J^{z_i} = \pm J$ subspace, we define

the pseudospin operators by

$$\tau^z_{\boldsymbol{R}i} = \frac{1}{2J}\mathcal{P}J^{z_i}_{\boldsymbol{R}i}\mathcal{P} \tag{2.10}$$

$$\tau^+_{\boldsymbol{R}i} = \frac{1}{(2J)!}\mathcal{P}(J^{+_i}_{\boldsymbol{R}i})^{2J}\mathcal{P}, \tag{2.11}$$

where $\tau^-_{\boldsymbol{R}i} = (\tau^+_{\boldsymbol{R}i})^\dagger$, $\tau^\pm_{\boldsymbol{R}i} = \tau^x_{\boldsymbol{R}i} \pm i\tau^y_{\boldsymbol{R}i}$, and $J^{\pm_i}_{\boldsymbol{R}i} = J^{x_i}_{\boldsymbol{R}i} \pm iJ^{y_i}_{\boldsymbol{R}i}$. With these conventions, the pseudospin operator $\tau^\mu_{\boldsymbol{R}i}$ ($\mu = x, y, z$) has eigenvalues $\pm 1/2$. We can now proceed to determine the symmetry transformations of $\tau^\mu_{\boldsymbol{R}i}$ in terms of the known transformations of $\boldsymbol{J}_{\boldsymbol{R}i}$.

The above discussion applies directly to DO doublets obtained from d-electrons [case (1) in the main text], upon replacing $\boldsymbol{J}_{\boldsymbol{R}i}$ with $\boldsymbol{j}^{\text{eff}}_{\boldsymbol{R}i}$, and J with $3/2$. Both $\boldsymbol{J}_{\boldsymbol{R}i}$ and $\boldsymbol{j}^{\text{eff}}_{\boldsymbol{R}i}$ transform identically under symmetry, namely as time-reversal odd pseudovectors.

The generators of the symmetry group act on $\boldsymbol{J}_{\boldsymbol{r}}$ as follows:

$$T_{\boldsymbol{a}_i} : \boldsymbol{J}_{\boldsymbol{r}} \rightarrow \boldsymbol{J}_{\boldsymbol{r}+\boldsymbol{a}_i} \tag{2.12}$$

$$\mathcal{I} : \boldsymbol{J}_{\boldsymbol{r}} \rightarrow \boldsymbol{J}_{\mathcal{I}\boldsymbol{r}} \tag{2.13}$$

$$C_{3,1} : \boldsymbol{J}_{\boldsymbol{r}} \rightarrow C^T_{3,1}\boldsymbol{J}_{C_{3,1}\boldsymbol{r}} \tag{2.14}$$

$$M_{x\bar{y}} : \boldsymbol{J}_{\boldsymbol{r}} \rightarrow -M^T_{x\bar{y}}\boldsymbol{J}_{M_{x\bar{y}}\boldsymbol{r}} \tag{2.15}$$

$$\mathcal{T} : \boldsymbol{J}_{\boldsymbol{r}} \rightarrow -\boldsymbol{J}_{\boldsymbol{r}}. \tag{2.16}$$

For each symmetry operation S, we let $\hat{U}_S$ be the unitary operator representing it. The above notation is short-hand for conjugation of $\boldsymbol{J}_{\boldsymbol{r}}$ by the appropriate unitary or anti-unitary operators representing each symmetry, **e.g.** $\mathcal{I} : \boldsymbol{J}_{\boldsymbol{r}} \rightarrow \hat{U}_{\mathcal{I}}\boldsymbol{J}_{\boldsymbol{r}}\hat{U}^\dagger_{\mathcal{I}} = \boldsymbol{J}_{\mathcal{I}\boldsymbol{r}}$.

From the above relations and the definition of $\tau^{\mu}_{\boldsymbol{r}}$, it is straightforward to show

$$T_{\boldsymbol{a}_i} : \tau^{\mu}_{\boldsymbol{r}} \rightarrow \tau^{\mu}_{\boldsymbol{r}+\boldsymbol{a}_i} \tag{2.17}$$

$$\mathcal{I} : \tau^{\mu}_{\boldsymbol{r}} \rightarrow \tau^{\mu}_{\mathcal{I}\boldsymbol{r}} \tag{2.18}$$

$$C_{3,1} : \tau^{\mu}_{\boldsymbol{r}} \rightarrow \tau^{\mu}_{C_{3,1}\boldsymbol{r}} \tag{2.19}$$

$$M_{x\bar{y}} : \tau^{x,z}_{\boldsymbol{r}} \rightarrow -\tau^{x,z}_{M_{x\bar{y}}\boldsymbol{r}} \tag{2.20}$$

$$M_{x\bar{y}} : \tau^{y}_{\boldsymbol{r}} \rightarrow \tau^{y}_{M_{x\bar{y}}\boldsymbol{r}} \tag{2.21}$$

$$\mathcal{T} : \tau^{\mu}_{\boldsymbol{r}} \rightarrow -\tau^{\mu}_{\boldsymbol{r}}. \tag{2.22}$$

It is notable that $\tau^{\mu}_{\boldsymbol{r}}$ transforms trivially under $C_{3,1}$ and that $\tau^{y}_{\boldsymbol{r}}$ transforms trivially under **all** space group operations. This is a direct reflection of the octupolar character of τ^y (see Sec. 2.5).

The space group transformation properties can be simply stated without choosing specific generators. Consider the diamond lattice formed by the tetrahedron centers $\mathbf{r}$. Every space group operation **either** preserves the diamond A-sublattice (and hence also the B-sublattice), **or** it exchanges A- and B-sublattices. We refer to the former operations as A/B-preserving, and the latter as A/B-exchanging. For improper A/B-preserving operations (**e.g.** mirror planes), $\tau^{x,z}_{\boldsymbol{r}}$ is odd. (More precisely, if S is such an operation, then $S : \tau^{x,z}_{\boldsymbol{r}} \rightarrow -\tau^{x,z}_{S\boldsymbol{r}}$.) For proper A/B-preserving operations, $\tau^{x,z}_{\boldsymbol{r}}$ is even. This is reversed for A/B-exchanging operations, with $\tau^{x,z}$ even under improper operations and odd under proper operations. Finally, $\tau^{y}_{\boldsymbol{r}}$ is even under **all** space group operations.

2.4.2 Itinerant case

Here, we work out the effect of space group and time reversal symmetry on electron operators, as required to construct models of itinerant electrons in DO doublets. Rather than pursuing a direct microscopic analysis, we adopt an indirect approach. The idea is to first write down, for each generator, the most general transformation of the electron operator consistent with the pseudospin transformations derived above. Each such transformation involves unknown phase factors, and in general the resulting transformations do not satisfy the relations defining the symmetry group. We

show that, up to gauge transformations, the phase factors are **completely** determined by requiring the group relations to hold.

We let $c^\dagger_{\boldsymbol{R}i\alpha}$, where $\alpha = \pm$, create an electron at site $(\boldsymbol{R}, i)$ in pseudospin state $\tau^z_{\boldsymbol{R}i} = 1/2$ for $\alpha = +$, and $\tau^z_{\boldsymbol{R}i} = -1/2$ for $\alpha = -$. It is convenient sometimes to suppress the pseudospin index and write $c^\dagger_{\boldsymbol{R}i}$, which we can think of as a two-component row vector of operators. Sometimes we suppress both spin and basis indices, writing $c^\dagger_{\boldsymbol{R}}$, an 8-component row vector of operators. The pseudospin operator is $\tau^\mu_{\boldsymbol{R}i} = \frac{1}{2} c^\dagger_{\boldsymbol{R}i} \sigma^\mu c_{\boldsymbol{R}i}$.

Since translations $T_{\boldsymbol{a}_i}$ commute, a gauge can be chosen in which

$$T_{\boldsymbol{a}_i} : c^\dagger_{\boldsymbol{R}} \to \hat{U}_{T_{\boldsymbol{a}_i}} c^\dagger_{\boldsymbol{R}} \hat{U}^\dagger_{T_{\boldsymbol{a}_i}} = c^\dagger_{\boldsymbol{R}+\boldsymbol{a}_i}. \tag{2.23}$$

The residual gauge freedom preserving this form of $T_{\boldsymbol{a}_i}$ is $c^\dagger_{\boldsymbol{R}i} \to \alpha^g_i c^\dagger_{\boldsymbol{R}i}$, where $\alpha^g_i \in \mathrm{U}(1)$.

The most general action of time reversal consistent with Eq. (2.22) is $\mathcal{T} : c^\dagger_{\boldsymbol{R}} \to \mathcal{T} c^\dagger_{\boldsymbol{R}} \mathcal{T}^{-1} = c^\dagger_{\boldsymbol{R}} U^{\mathcal{T}}_{\boldsymbol{R}}$, where

$$U^{\mathcal{T}}_{\boldsymbol{R}} = \begin{pmatrix} \alpha^{\mathcal{T}}_{\boldsymbol{R}1}(i\sigma^y) & 0 & 0 & 0 \\ 0 & \alpha^{\mathcal{T}}_{\boldsymbol{R}2}(i\sigma^y) & 0 & 0 \\ 0 & 0 & \alpha^{\mathcal{T}}_{\boldsymbol{R}3}(i\sigma^y) & 0 \\ 0 & 0 & 0 & \alpha^{\mathcal{T}}_{\boldsymbol{R}4}(i\sigma^y) \end{pmatrix}, \tag{2.24}$$

where $\alpha^{\mathcal{T}}_{\boldsymbol{R}i} \in \mathrm{U}(1)$. Using the fact that $\hat{U}_{T_{\boldsymbol{a}_i}} \mathcal{T} = \mathcal{T} \hat{U}_{T_{\boldsymbol{a}_i}}$, it is easy to show $\alpha^{\mathcal{T}}_{\boldsymbol{R}i} \equiv \alpha^{\mathcal{T}}_i$. Moreover, we can make a gauge transformation to set $\alpha^{\mathcal{T}}_i = 1$, and thus $\mathcal{T} : c^\dagger_{\boldsymbol{R}i} \to c^\dagger_{\boldsymbol{R}i}(i\sigma^y)$. The residual gauge freedom preserving the form of both translations and time reversal is still $c^\dagger_{\boldsymbol{R}i} \to \alpha^g_i c^\dagger_{\boldsymbol{R}i}$, but now each $\alpha^g_i \in \{\pm 1\}$.

The most general form of $C_{3,1}$ rotation consistent with the pseudospin transformations is

$$C_{3,1} : c^\dagger_{\boldsymbol{R}} \to \hat{U}_{C_{3,1}} c^\dagger_{\boldsymbol{R}} \hat{U}^\dagger_{C_{3,1}} = c^\dagger_{C_{3,1}\boldsymbol{R}} U^{C_{3,1}}_{\boldsymbol{R}}, \tag{2.25}$$

where the 8×8 matrix $U_{\boldsymbol{R}}^{C_{3,1}}$ is given in 2×2 block form by

$$U_{\boldsymbol{R}}^{C_{3,1}} = \begin{pmatrix} \alpha_{\boldsymbol{R}0}^{C} & 0 & 0 & 0 \\ 0 & 0 & 0 & \alpha_{\boldsymbol{R}1}^{C} \\ 0 & \alpha_{\boldsymbol{R}2}^{C} & 0 & 0 \\ 0 & 0 & \alpha_{\boldsymbol{R}3}^{C} & 0 \end{pmatrix}, \tag{2.26}$$

for $\alpha_{\boldsymbol{R}i}^{C} \in \mathrm{U}(1)$. This is simplified by noting that $\hat{U}_{C_{3,1}} \hat{U}_{T_{\boldsymbol{a}_i}} = \hat{U}_{T_{C_{3,1}\boldsymbol{a}_i}} \hat{U}_{C_{3,1}}$ implies $\alpha_{\boldsymbol{R}i}^{C} \equiv \alpha_i^{C}$, and $\mathcal{T}\hat{U}_{C_{3,1}} = \hat{U}_{C_{3,1}}\mathcal{T}$ gives $\alpha_i^{C} \in \{\pm 1\}$.

To proceed further, we employ the relation $[\hat{U}_{C_{3,1}}]^3 = -1$, where the minus sign reflects the $S = 1/2$ nature of electrons. This implies that $\alpha_1^{C} = -1$, and $\alpha_2^{C}\alpha_3^{C}\alpha_4^{C} = -1$. It is then possible set all $\alpha_i^{C} = -1$, by making a gauge transformation of the form $\alpha_1^{g} = 1$, and $\alpha_i^{g} \in \{\pm 1\}$ (for $i = 2, 3, 4$). The resulting form of $C_{3,1}$ rotation is still preserved by gauge transformations with $\alpha_1^{g} \in \{\pm 1\}$ and $\alpha_i^{g} = 1$ (for $i = 2, 3, 4$).

Next we consider the mirror reflection $M_{x\bar{y}}$, which acts on electron operators by

$$M_{x\bar{y}} : c_{\boldsymbol{R}}^{\dagger} \to \hat{U}_{M_{x\bar{y}}} c_{\boldsymbol{R}}^{\dagger} \hat{U}_{M_{x\bar{y}}}^{\dagger} = c_{M_{x\bar{y}}\boldsymbol{R}}^{\dagger} U_{\boldsymbol{R}}^{M_{x\bar{y}}}, \tag{2.27}$$

where

$$U^{M_{x\bar{y}}} = \begin{pmatrix} 0 & 0 & 0 & \alpha_{\boldsymbol{R}1}^{M}(i\sigma^y) \\ 0 & \alpha_{\boldsymbol{R}2}^{M}(i\sigma^y) & 0 & 0 \\ 0 & 0 & \alpha_{\boldsymbol{R}3}^{M}(i\sigma^y) & 0 \\ \alpha_{\boldsymbol{R}4}^{M}(i\sigma^y) & 0 & 0 & 0 \end{pmatrix}, \tag{2.28}$$

where $\alpha_{\boldsymbol{R}i}^{M} \in \mathrm{U}(1)$. The relation $\hat{U}_{M_{x\bar{y}}} \hat{U}_{T_{\boldsymbol{a}_i}} = \hat{U}_{T_{M_{x\bar{y}}\boldsymbol{a}_i}} \hat{U}_{M_{x\bar{y}}}$ implies $\alpha_{\boldsymbol{R}i}^{M} \equiv \alpha_i^{M}$, and $\mathcal{T}\hat{U}_{M_{x\bar{y}}} = \hat{U}_{M_{x\bar{y}}}\mathcal{T}$ gives $\alpha_i^{M} \in \{\pm 1\}$.

Viewing $M_{x\bar{y}}$ as the composition of a C_2 rotation and an inversion, we require the relation $[\hat{U}_{M_{x\bar{y}}}]^2 = -1$, which implies $\alpha_1^{M} = \alpha_4^{M}$. The relation $[\hat{U}_{M_{x\bar{y}}}\hat{U}_{C_{3,1}}]^4 = -1$ then implies $\alpha_2^{M} = -\alpha_3^{M}$. To fix the remaining free parameters, in addition to gauge freedom, we have the freedom to redefine $\hat{U}_{M_{x\bar{y}}} \to -\hat{U}_{M_{x\bar{y}}}$, which allows us to set $\alpha_2^{M} = -1$, $\alpha_3^{M} = 1$. We can then make a

gauge transformation of the form $\alpha_1^g \in \{\pm 1\}$, $\alpha_i^g = 1$ (for $i = 2, 3, 4$), to set $\alpha_1^M = \alpha_4^M = 1$, thus completely fixing the form of $\hat{U}_{M_{x\bar{y}}}$.

The only remaining generator is inversion, which acts on electron operators by

$$\mathcal{I} : c^\dagger_{\boldsymbol{R}i} \to \hat{U}_\mathcal{I} c^\dagger_{\boldsymbol{R}i} \hat{U}^\dagger_\mathcal{I} = c^\dagger_{[-\boldsymbol{R}+2(\boldsymbol{b}_1-\boldsymbol{b}_i)],i} \alpha^\mathcal{I}_{\boldsymbol{R}i}, \tag{2.29}$$

for $\alpha^\mathcal{I}_{\boldsymbol{R}i} \in \mathrm{U}(1)$. The relation $\hat{U}_{T_{\boldsymbol{a}_i}} \hat{U}_\mathcal{I} = \hat{U}_\mathcal{I} T_{-\boldsymbol{a}_i}$ implies $\alpha^\mathcal{I}_{\boldsymbol{R}i} \equiv \alpha^\mathcal{I}_i$, and $\mathcal{T}\hat{U}_\mathcal{I} = \hat{U}_\mathcal{I}\mathcal{T}$ gives $\alpha^\mathcal{I} \in \{\pm 1\}$.

To proceed further, considering the action of the relation $\hat{U}_\mathcal{I}\hat{U}_{C_{3,1}} = \hat{U}_{C_{3,1}}\hat{U}_\mathcal{I}$ on $c^\dagger_{\boldsymbol{R}i}$, for $\boldsymbol{R} = 0$, gives $\alpha^\mathcal{I}_2 = \alpha^\mathcal{I}_3 = \alpha^\mathcal{I}_4$. Similarly, acting on $c^\dagger_{0,0}$ with $\hat{U}_{T_{\boldsymbol{a}_3}}\hat{U}_\mathcal{I}\hat{U}_{M_{x\bar{y}}} = \hat{U}_{M_{x\bar{y}}}\hat{U}_\mathcal{I}$ gives $\alpha^\mathcal{I}_1 = \alpha^\mathcal{I}_4$, and thus all the $\alpha^\mathcal{I}_i$ are equal. We can then set $\alpha^\mathcal{I}_i = 1$ by exploiting the freedom to send $\hat{U}_\mathcal{I} \to -\hat{U}_\mathcal{I}$.

We have thus completely fixed the action of symmetry on electron operators. To summarize, we have obtained the following results:

$$T_{\boldsymbol{a}_i} : c^\dagger_{\boldsymbol{R}} \to c^\dagger_{\boldsymbol{R}+\boldsymbol{a}_i} \tag{2.30}$$

$$\mathcal{I} : c^\dagger_{\boldsymbol{R}i} \to c^\dagger_{[-\boldsymbol{R}+2(\boldsymbol{b}_1-\boldsymbol{b}_i)],i} \tag{2.31}$$

$$C_{3,1} : c^\dagger_{\boldsymbol{R}} \to c^\dagger_{C_{3,1}\boldsymbol{R}} U^{C_{3,1}} \tag{2.32}$$

$$M_{x\bar{y}} : c^\dagger_{\boldsymbol{R}} \to c^\dagger_{M_{x\bar{y}}\boldsymbol{R}} U^{M_{x\bar{y}}} \tag{2.33}$$

$$\mathcal{T} : c^\dagger_{\boldsymbol{R}i} \to c^\dagger_{\boldsymbol{R}i}(i\sigma^y), \tag{2.34}$$

where the 8×8 matrices $U^{C_{3,1}}$ and $U^{M_{x\bar{y}}}$ are given in 2×2 block form by

$$U^{C_{3,1}}_{\boldsymbol{R}} = \begin{pmatrix} -1 & 0 & 0 & 0 \\ 0 & 0 & 0 & -1 \\ 0 & -1 & 0 & 0 \\ 0 & 0 & -1 & 0 \end{pmatrix}, \tag{2.35}$$

$$U^{M_{x\bar{y}}} = \begin{pmatrix} 0 & 0 & 0 & (i\sigma^y) \\ 0 & -(i\sigma^y) & 0 & 0 \\ 0 & 0 & (i\sigma^y) & 0 \\ (i\sigma^y) & 0 & 0 & 0 \end{pmatrix}. \tag{2.36}$$

We have also obtained the same results directly from a microscopic analysis[99], but prefer the indirect approach presented here both for its greater technical simplicity, and the additional insight it provides.

2.5 Dipolar-octupolar nature of the doublets

Here, we consider the transformation of τ^μ under the D_{3d} site symmetry. We show that $\tau^{x,z}$ transform like m_z, the z-component of a magnetic dipole, while τ^y does not transform like any component of a magnetic dipole. Instead, τ^y transforms like a component of the magnetic octupole tensor $T_{\mu\nu\lambda}$. In this section, we will consider a fixed site $\boldsymbol{r}$. We consider dipole m_μ and octupole $T_{\mu\nu\lambda}$ tensors in the local coordinates introduced in Sec. 2.3, suppressing the basis index i to simplify the notation.

The D_{3d} site symmetry is generated by 3-fold rotation C_3, inversion $\mathcal{I}$, and a mirror plane M. (There are three different mirror planes; we arbitrarily choose one of these to be a generator.) The dipole m_μ transforms as a pseudovector under these operations, as does each index of $T_{\mu\nu\lambda}$. It follows from Sec. 2.4.1 that

$$C_3 : \tau^\mu \rightarrow \tau^\mu \tag{2.37}$$

$$M : \tau^{x,z} \rightarrow -\tau^{x,z} \tag{2.38}$$

$$M : \tau^y \rightarrow \tau^y \tag{2.39}$$

$$\mathcal{I} : \tau^\mu \rightarrow \tau^\mu. \tag{2.40}$$

It is clear that τ^μ does not transform as a pseudovector. We observe that τ^z and τ^x transform identically to one another, and also to m_z; therefore the $\mu = x, z$ components of τ^μ are dipolar. On the other hand, τ^y does not transform as any component of m_μ. Note that inversion does not play an important role, acting trivially on τ^μ, m_μ and $T_{\mu\nu\lambda}$.

Instead, τ^y transforms identically to a component of $T_{\mu\nu\lambda}$. To identify the appropriate com-

ponent, we change coordinates from $\mu = x, y, z$ to $\alpha = +, -, z$ by writing

$$m_\alpha = R_{\alpha\mu} m_\mu \tag{2.41}$$

$$T_{\alpha\beta\gamma} = R_{\alpha\mu} R_{\beta\nu} R_{\gamma\lambda} T_{\mu\nu\lambda}, \tag{2.42}$$

where

$$R = \begin{pmatrix} 1 & i & 0 \\ 1 & -i & 0 \\ 0 & 0 & 1 \end{pmatrix}. \tag{2.43}$$

We have transformation laws

$$C_3 : m_\pm \rightarrow e^{\pm 2\pi i/3} m_\pm \tag{2.44}$$

$$C_3 : m_z \rightarrow m_z \tag{2.45}$$

$$M : m_\pm \rightarrow e^{\pm i\phi_M} m_\mp \tag{2.46}$$

$$M : m_z \rightarrow -m_z, \tag{2.47}$$

with the same transformations holding for each index of $T_{\alpha\beta\gamma}$. Here, $\phi_M = \pi, \pi/3, -\pi/3$, depending on which of the three D_{3d} mirror planes is chosen for M. For our purposes, the phase factor ϕ_M is unimportant, as it drops out in the transformation of T_{+++} and T_{---}; that is

$$M : T_{+++} \rightarrow -T_{---} \tag{2.48}$$

$$M : T_{---} \rightarrow -T_{+++}. \tag{2.49}$$

Using these transformations, we can identify

$$\tau^y \sim i(T_{+++} - T_{---}). \tag{2.50}$$

As desired, the right-hand side is real and time-reversal odd, since time reversal $\mathcal{T} : m_\pm \rightarrow -m_\mp$.

2.6 Tight-binding model

Here we describe the symmetry allowed tight-binding model for itinerant electrons in DO doublets on the pyrochlore lattice, and provide more information on the analysis of the corresponding electron band structures.

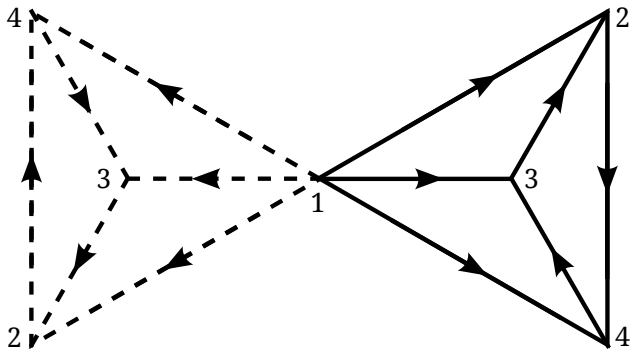

Figure 2.5: Orientations of nearest-neighbor bonds for which the nearest-neighbor hopping takes an identical form on every bond. The sites are numbered by basis index $i = 1, \ldots, 4$. The center of the tetrahedron on the right (solid line bonds) lies in the diamond A-sublattice, while that of the left-hand tetrahedron (dashed-line bonds) lies in the diamond B-sublattice.

Requiring $Fd\bar{3}m$ space group and time reversal symmetry, the symmetry transformations given in Sec. 2.4.2 can be used to determine the most general tight-binding model allowed by symmetry. The electron hopping has the general form given in Eq. (2) of the main text

$$H_{TB} = \sum_{(\boldsymbol{r},\boldsymbol{r}')} \left[c^\dagger_{\boldsymbol{r}} T_{\boldsymbol{r}\boldsymbol{r}'} c_{\boldsymbol{r}'} + h.c. \right], \tag{2.51}$$

where the sum is over all bonds, with some arbitrary but fixed choice of orientation for each bond. Time reversal symmetry implies $T_{\boldsymbol{r}\boldsymbol{r}'} = t^0_{\boldsymbol{r}\boldsymbol{r}'} + i t^\mu_{\boldsymbol{r}\boldsymbol{r}'} \sigma^\mu$. For nearest-neighbor bonds $\langle \boldsymbol{r}\boldsymbol{r}' \rangle$, space group symmetry implies

$$T_{\langle \boldsymbol{r}\boldsymbol{r}' \rangle} = i t^1_{nn} \sigma^x + i t^3_{nn} \sigma^z, \tag{2.52}$$

with the orientation shown in Fig. 2.5. The nearest-neighbor hopping Hamiltonian thus has an **identical** form on every bond. A pseudospin rotation about the local y_i axes can eliminate one hopping parameter, resulting in

$$H_{nn} = \sum_{\langle \boldsymbol{r}\boldsymbol{r}' \rangle} \tilde{c}^\dagger_{\boldsymbol{r}} (i \tilde{t}^3_{nn} \sigma^z) \tilde{c}_{\boldsymbol{r}'} + h.c., \tag{2.53}$$

where $\tilde{t}^3_{nn} = \sqrt{(t^1_{nn})^2 + (t^3_{nn})^2}$ and $\tilde{c}_{\boldsymbol{r}}, \tilde{c}^\dagger_{\boldsymbol{r}}$ are electron operators in the rotated basis.

The nearest-neighbor model at half-filling has a non-generic and highly unstable Fermi surface specified by $\cos\frac{k_x}{2} + \cos\frac{k_y}{2} + \cos\frac{k_z}{2} = 0$, which coincides with a surface of intersection between two bands. The corresponding band structure is plotted in Fig. 2.6(a). This highly fine-tuned Fermi surface is unstable to further-neighbor hopping, and it is thus crucial to include at least second-neighbor hopping in the tight-binding model.

Letting $(\boldsymbol{r}\boldsymbol{r}')_2$ label second-neighbor bonds, we specify the second-neighbor hopping by giving $T_{\boldsymbol{r}\boldsymbol{r}'}$ on a reference bond $(\boldsymbol{r}_0\boldsymbol{r}'_0)_2$, where $\boldsymbol{r}_0 = \boldsymbol{b}_2$, $\boldsymbol{r}'_0 = -\frac{1}{4}(1,1,1) - \boldsymbol{b}_4$. We have

$$T_{(\boldsymbol{r}_0\boldsymbol{r}'_0)_2} = w_0 + i w_x \sigma^x + i w_z \sigma^z, \tag{2.54}$$

where w_y is forbidden by the C_2 rotation symmetry taking the bond into itself. The reference bond can be mapped into any second-neighbor bond by an appropriate space group operation, so all $T_{(\boldsymbol{r}\boldsymbol{r}')_2}$ can be obtained from $T_{(\boldsymbol{r}_0\boldsymbol{r}'_0)_2}$. Unlike for nearest-neighbor hopping, the form of $T_{(\boldsymbol{r}\boldsymbol{r}')_2}$ varies

from bond to bond. The global pseudospin rotation resulting in Eq. (2.53) for nearest-neighbor hopping affects the second-neighbor hopping merely by transforming the parameters $(w_0, w_x, w_z) \to (\tilde{w}_0, \tilde{w}_x, \tilde{w}_z)$.

Including second-neighbor hopping, we find that the ground state is either a metal [Fig. 2.6(b)] or semimetal with isolated four-fold band touchings at the W-points. [Fig. 2.6(c)]. The phase diagram is discussed in the main text. The putative semi-metal phase is an incipient topological band insulator. Because there is a gap at all time reversal invariant momenta, the Z_2 invariant can be computed using the Fu-Kane formula [100], and is found to correspond to a strong topological insulator. This implies that **any** time reversal preserving perturbation that opens a full gap leads to a strong topological insulator.

In fact, the W point band touching in the semimetal phase is unstable, and its presence is an artifact of restriction to only first- and second-neighbor hopping. Upon including fourth-neighbor hopping, a gap opens at the W point, resulting in a strong topological insulator (third-neighbor hopping does not open a gap). To establish this, among the 6 distinct W points, we focus on $\boldsymbol{k}_W = (2\pi, \pi, 0)$. Letting $H(\boldsymbol{k})$ be the 8×8 Bloch Hamiltonian including first- and second-neighbor hopping, we observe that $H(\boldsymbol{k}_W)$ is block-diagonalized by the unitary transformation $\tilde{H}(\boldsymbol{k}) = U_W^\dagger H(\boldsymbol{k}) U_W$, where

$$U_W = \frac{1}{\sqrt{2}} \begin{pmatrix} 1 & 0 & 1 & 0 \\ 0 & 1 & 0 & 1 \\ i & 0 & -i & 0 \\ 0 & i & 0 & -i \end{pmatrix} \otimes \mathbb{1}_{2\times 2}. \tag{2.55}$$

Here $\mathbb{1}_{2\times 2}$ is the identity matrix acting in the DO doublet pseudospin space. We find, in 4×4 block form

$$\tilde{H}(\boldsymbol{k}_W) = \begin{pmatrix} \epsilon_F \mathbb{1}_{4\times 4} & 0 \\ 0 & K \end{pmatrix}, \tag{2.56}$$

where the upper-left block acts in the manifold of the 4-fold touching, ϵ_F is the Fermi energy, and K is a Hermitian 4×4 matrix with eigenvalues not equal to ϵ_F.

To proceed, we consider the 4×4 effective Hamiltonian $H_{\text{eff}}(\boldsymbol{q})$ that describes the splitting of the band touching for $\boldsymbol{k} = \boldsymbol{k}_W + \boldsymbol{q}$, where $\boldsymbol{q}$ is small compared to the Brillouin zone size. In principle, this can be constructed by expanding the Bloch Hamiltonian $H(\boldsymbol{k}_W + \boldsymbol{q})$ in powers of $\boldsymbol{q}$, and treating the $\boldsymbol{q}$-dependent terms via degenerate perturbation theory.

For the present purposes, it is more useful to determine the most general form of $H_{\text{eff}}(\boldsymbol{q})$ allowed by symmetry. The group of the wavevector for $\boldsymbol{k}_W$ is isomorphic to C_{4v}, and is generated by the four-fold rotation-reflection $S_{4y} = C_{3,1}M_{x\bar{y}}$ and the mirror reflection $M_x = \mathcal{I}C_{2x}$, where $C_{2x} \in T_d$ is a π-rotation about the (100) axis. In addition, the composition of inversion and time reversal $\mathcal{IT}$ is an anti-unitary symmetry leaving all $\boldsymbol{k}$-points invariant. Using the results of Sec. 2.4.2, and the transformation U_W, we determined the action of these symmetries in the 4-dimensional manifold of the band touching. To quote the results, we introduce the operators $T^\mu = \sigma^\mu \otimes \mathbb{1}_{2\times 2}$ and $\Sigma^\mu = \mathbb{1}_{2\times 2} \otimes \sigma^\mu$; any 4×4 Hermitian matrix can be written as a real linear combination of $\mathbb{1}_{4\times 4}$, T^μ, Σ^μ, and $T^\mu\Sigma^\nu$. The symmetries act as follows:

$$S_{4y} : \Sigma^{x,z} \rightarrow -\Sigma^{x,z} \tag{2.57}$$

$$S_{4y} : \Sigma^{y} \rightarrow \Sigma^{y} \tag{2.58}$$

$$S_{4y} : T^{x} \rightarrow -T^{y} \tag{2.59}$$

$$S_{4y} : T^{y} \rightarrow -T^{x} \tag{2.60}$$

$$S_{4y} : T^{z} \rightarrow -T^{z} \tag{2.61}$$

$$S_{4y} : (q_x, q_y, q_z) \rightarrow (q_z, -q_y, -q_x), \tag{2.62}$$

and

$$M_{x} : \Sigma^{\mu} \rightarrow \Sigma^{\mu} \tag{2.63}$$

$$M_{x} : T^{x} \rightarrow -T^{y} \tag{2.64}$$

$$M_{x} : T^{y} \rightarrow -T^{x} \tag{2.65}$$

$$M_{x} : T^{z} \rightarrow -T^{z} \tag{2.66}$$

$$M_{x} : (q_x, q_y, q_z) \rightarrow (-q_x, q_y, q_z), \tag{2.67}$$

and finally

$$\mathcal{IT} : \Sigma^\mu \rightarrow -\Sigma^\mu \tag{2.68}$$

$$\mathcal{IT} : T^x \rightarrow T^y \tag{2.69}$$

$$\mathcal{IT} : T^y \rightarrow T^x \tag{2.70}$$

$$\mathcal{IT} : T^z \rightarrow T^z \tag{2.71}$$

$$\mathcal{IT} : \boldsymbol{q} \rightarrow \boldsymbol{q}. \tag{2.72}$$

The most general Hamiltonian respecting $\mathcal{IT}$ is

$$H_{\text{eff}}(\boldsymbol{q}) = \epsilon_0(\boldsymbol{q})\mathbb{1}_{4\times 4} + f_a(\boldsymbol{q})\gamma_a, \tag{2.73}$$

where $a = 1, \ldots, 5$, the $f_a(\boldsymbol{q})$ are arbitrary functions of $\boldsymbol{q}$, and

$$\gamma_1 = \frac{1}{\sqrt{2}}\Sigma^x(T^x - T^y) \tag{2.74}$$

$$\gamma_2 = \frac{1}{\sqrt{2}}\Sigma^y(T^x - T^y) \tag{2.75}$$

$$\gamma_3 = \frac{1}{\sqrt{2}}\Sigma^z(T^x - T^y) \tag{2.76}$$

$$\gamma_4 = \frac{1}{\sqrt{2}}(T^x + T^y) \tag{2.77}$$

$$\gamma_5 = T^z. \tag{2.78}$$

The γ_a matrices satisfy the γ-matrix algebra $\{\gamma_a, \gamma_b\} = 2\delta_{ab}$, and it follows that the energy spectrum of $H_{\text{eff}}(\boldsymbol{q})$ is

$$E_\pm(\boldsymbol{q}) = \epsilon_0(\boldsymbol{q}) \pm \sqrt{\sum_{a=1}^{5}[f_a(\boldsymbol{q})]^2}, \tag{2.79}$$

where each (non-zero) energy level is two-fold degenerate. A band touching occurs at $\boldsymbol{q}$ only when $f_a(\boldsymbol{q}) = 0$ for all a. In the putative W-point semi-metal, there is an isolated touching at $\boldsymbol{q} = 0$, and $\epsilon_0(0) = \epsilon_F$.

The remaining symmetries S_{4y} and M_x constrain the form of the $f_a(\boldsymbol{q})$. Keeping terms up

through second order in $\boldsymbol{q}$, we find:

$$f_1(\boldsymbol{q}) = c_{1y}q_y + c_{1xx}(q_x^2 - q_z^2) \tag{2.80}$$

$$f_2(\boldsymbol{q}) = m + c_{2yy}q_y^2 + c_{2xx}(q_x^2 + q_z^2) \tag{2.81}$$

$$f_3(\boldsymbol{q}) = c_{3y}q_y + c_{3xx}(q_x^2 - q_z^2) \tag{2.82}$$

$$f_4(\boldsymbol{q}) = c_{4xz}q_xq_z \tag{2.83}$$

$$f_5(\boldsymbol{q}) = c_{5xz}q_xq_z \tag{2.84}$$

$$\epsilon_0(\boldsymbol{q}) = \epsilon_F + e_{0yy}q_y^2 + e_{0xx}(q_x^2 + q_z^2). \tag{2.85}$$

There is clearly a 4-fold touching at $\boldsymbol{q} = 0$ only if $m = 0$, so evidently it happens that m vanishes if we only include first- and second-neighbor hopping. This can be understood by recalling that first- and second-neighbor hopping do not involve the σ^y Pauli matrix in the DO doublet space, and thus the 8×8 Bloch Hamiltonian can be written in the form

$$H(\boldsymbol{k}) = M_0(\boldsymbol{k}) \otimes \mathbb{1}_{2\times 2} + M_1(\boldsymbol{k}) \otimes \sigma^x + M_3(\boldsymbol{k}) \otimes \sigma^z, \tag{2.86}$$

where the $M_{0,1,3}(\boldsymbol{k})$ are 4×4 Hermitian matrices. It follows from the form of U_W that also

$$\tilde{H}(\boldsymbol{k}) = \tilde{M}_0(\boldsymbol{k}) \otimes \mathbb{1}_{2\times 2} + \tilde{M}_1(\boldsymbol{k}) \otimes \sigma^x + \tilde{M}_3(\boldsymbol{k}) \otimes \sigma^z \tag{2.87}$$

Now, $H_{\text{eff}}(\boldsymbol{q} = 0)$ is simply the upper-left 4×4 block of $\tilde{H}(\boldsymbol{k}_W)$, and we thus see that Σ^y and $\Sigma^y T^\mu$ terms cannot appear. In particular, since $\gamma_2 = \Sigma^y(T^x - T^y)/\sqrt{2}$, this implies that $f_2(0) = 0$. This result holds unless we consider hopping that involves σ^y in the DO doublet space; it turns out that the shortest-range hopping for which this occurs is fourth-neighbor.

Now we consider the effect of a small $m \neq 0$ on the energy spectrum. We are interested in the presence or absence of a gap. We first note that, in the quadratic approximation for $f_a(\boldsymbol{q})$, and for generic values of the parameters c_{1y}, c_{1xx}, etc., $\sum_{a\neq 2}[f_a(\boldsymbol{q})]^2 \neq 0$ for $\boldsymbol{q} \neq 0$. Then since $f_2(0) = m$, $\sum_a [f_a(\boldsymbol{q})]^2 \neq 0$ for all $\boldsymbol{q}$, and a full gap is opened. For generic parameters, this result is also expected to hold beyond the quadratic approximation, since each $f_a(\boldsymbol{q}) = 0$ defines a surface in $\boldsymbol{q}$-space, and the four surfaces for $a = 1, 3, 4, 5$, apart from intersecting at $\boldsymbol{q} = 0$, are not expected to have other intersections.

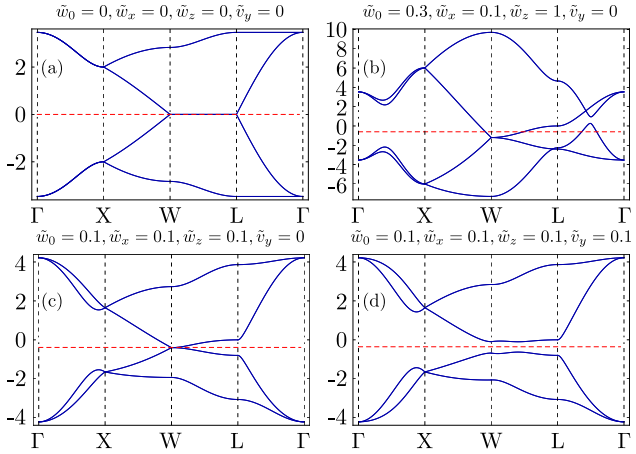

Figure 2.6: Band structure along high symmetry lines with energy in units of $\tilde{t}^3_{nn}$. (a) Only nearest-neighbor hopping is considered. (b) The metallic phase when both nearest-neighbor and second-neighbor hoppings are present. (c) The semimetal phase with W-point band touchings when nearest-neighbor and second-neighbor hoppings are present. (d) The strong topological insulator phase after the fourth-neighbor hopping is included on top of the nearest-neighbor and second-neighbor hopping. The topological invariant of the strong topological insulator is $(\nu; \nu_1, \nu_2, \nu_3) = (1; 0, 0, 0)$.

The above discussion implies that a small fourth-neighbor hopping will open a gap at the W point, which we have directly verified. A band structure illustrating this effect is shown in Fig. 2.6(d).

2.7 XYZ model and quantum spin ice

Here, we mention some features of the XYZ Hamiltonian

$$H_{\rm XYZ} = \sum_{\langle \boldsymbol{r}\boldsymbol{r}'\rangle} \tilde{J}_x \tilde{\tau}^x_{\boldsymbol{r}} \tilde{\tau}^x_{\boldsymbol{r}'} + \tilde{J}_y \tilde{\tau}^y_{\boldsymbol{r}} \tilde{\tau}^y_{\boldsymbol{r}'} + \tilde{J}_z \tilde{\tau}^z_{\boldsymbol{r}} \tilde{\tau}^z_{\boldsymbol{r}'}, \tag{2.88}$$

and discuss its dQSI and oQSI phases.

First, we note that $H_{\rm XYZ}$ has an extra $Z_2 \times Z_2$ spin symmetry, which is not expected to be preserved upon including longer-range or multi-spin exchange. Keeping this in mind, for simplicity we have confined our attention to the nearest-neighbor model.

The XYZ Hamiltonian has no quantum Monte Carlo sign problem over a substantial portion of its parameter space. This is seen upon expressing $H_{\rm XYZ}$ in terms of $\tilde{\tau}^z$ and $\tilde{\tau}^{\pm} = \tilde{\tau}^x \pm i\tilde{\tau}^y$, where

$$\begin{aligned} H_{\rm XYZ} \;=\; & \sum_{\langle \boldsymbol{r}\boldsymbol{r}'\rangle} \Big[J_{zz} \tilde{\tau}^z_{\boldsymbol{r}} \tilde{\tau}^z_{\boldsymbol{r}'} - J_{\pm} (\tilde{\tau}^+_{\boldsymbol{r}} \tilde{\tau}^-_{\boldsymbol{r}'} + h.c.) \\ & + J_{\pm\pm} (\tilde{\tau}^+_{\boldsymbol{r}} \tilde{\tau}^+_{\boldsymbol{r}'} + h.c.) \Big]. \end{aligned} \tag{2.89}$$

Here, $J_{zz} = \tilde{J}_z$, $J_{\pm} = -\frac{1}{4}(\tilde{J}_x + \tilde{J}_y)$, and $J_{\pm\pm} = \frac{1}{4}(\tilde{J}_x - \tilde{J}_y)$. The XYZ Hamiltonian is thus similar to the model discussed in Ref. [73], but is simpler in that it lacks the bond-dependent phase factors of the latter model. Because the transformation $\tilde{\tau}^+ \to i\tilde{\tau}^+$ sends $J_{\pm\pm} \to -J_{\pm\pm}$ without affecting the other terms, there will be no sign problem when $\tilde{J}_x + \tilde{J}_y < 0$, in world-line or stochastic series expansion quantum Monte Carlo. By cubic permutations, the sign problem is also absent when $\tilde{J}_y + \tilde{J}_z < 0$ or $\tilde{J}_x + \tilde{J}_z < 0$.

Now, we discuss quantum spin ice in the perturbative regime [53], where $J_{zz} > 0$ and $J_{zz} \gg |J_{\pm}|, |J_{\pm\pm}|$. In the limit of $J_{\pm} \to 0$ and $J_{\pm\pm} \to 0$, the resulting Hamiltonian produces an extensively degenerate ground state manifold that is spanned by the so-called "two-in-two-out" spin ice configurations.

Quantum dynamics is turned on with small $J_\pm$ and $J_{\pm\pm}$. Standard degenerate perturbation theory generates an effective low energy Hamiltonian that acts within the spin-ice manifold. The leading-order effective Hamiltonian is

$$H_{\text{eff}} = J_{\text{ring}} \sum_{\text{hexagon}} \left(\tilde{\tau}_1^+ \tilde{\tau}_2^- \tilde{\tau}_3^+ \tilde{\tau}_4^- \tilde{\tau}_5^+ \tilde{\tau}_6^- + h.c., \right) \tag{2.90}$$

where $1, 2, \cdots, 6$ label the 6 spins on the perimeter of a pyrochlore hexagon, and $J_{\text{ring}} \propto J_\pm^3 / J_{zz}^2$. $J_{\pm\pm}$ does not contribute to H_{eff} at third-order.

H_{eff} can be mapped to a U(1) lattice gauge theory [53] by writing

$$\tilde{\tau}_{\boldsymbol{r}}^z = E_{\mathbf{r}\mathbf{r}'}, \tag{2.91}$$

$$\tilde{\tau}_{\boldsymbol{r}}^\pm = e^{\pm i A_{\mathbf{r}\mathbf{r}'}}, \tag{2.92}$$

where the pyrochlore site $\boldsymbol{r}$ corresponds to the link $\mathbf{r}\mathbf{r}'$ of the dual diamond lattice, and E and A are a lattice electric field and vector potential defined on the diamond links. This definition holds for $\mathbf{r}$ in the diamond A-sublattice and $\mathbf{r}'$ in the diamond B-sublattice. In order to interpret E and A as lattice vector fields, we choose $E_{\mathbf{r}\mathbf{r}'} = -E_{\mathbf{r}'\mathbf{r}}$ and $A_{\mathbf{r}\mathbf{r}'} = -A_{\mathbf{r}'\mathbf{r}}$.

The Hamiltonian H_{eff} can be interpreted as the Maxwell term suppressing magnetic flux through each hexagon. We focus on $J_\pm \geq 0$, where $J_{\text{ring}} < 0$, which favors a ground state with zero flux through each hexagon.

Quantum spin ice can be understood as the deconfined phase of U(1) gauge theory [53], and is in fact the ground state of the ring exchange Hamiltonian H_{eff} [88]. The low-energy effective Hamiltonian density is simply $\mathcal{H} = K_e \vec{E}^2 + K_b \vec{B}^2$, where $\vec{E}$, $\vec{B}$ are continuum electric and magnetic fields. So far we have been describing dQSI. Upon permuting the axes in pseudospin space, the same discussion applies to oQSI, which arises when $\tilde{J}_y > 0$ is large. The difference lies only in the space group transformations of the electric and magnetic fields.

In the continuum theory, we consider transformations of $\vec{E}$ and $\vec{B}$ under the O_h point group to distinguish dQSI and oQSI. It is straightforward to identify the irreducible representations of O_h under which $\vec{E}$ and $\vec{B}$ transform. In dQSI, $\vec{E}$ transforms as Γ_4^+ (pseudovector representation)

with $\vec{B}$ transforming as Γ_4^- (vector representation). In oQSI, on the other hand, $\vec{E}$ transforms as Γ_5^+, with $\vec{B}$ transforming as Γ_5^-. In both dQSI and oQSI, $\vec{E}$ ($\vec{B}$) is odd (even) under time reversal.

The oQSI transformations can be simply understood by noting that $O_h = T_d \times Z_2$, where T_d is the group of symmetries of a pyrochlore tetrahedron, and the Z_2 is generated by inversion $\mathcal{I}$. Then any $g \in O_h$ can be uniquely written $g = \mathcal{I}^s t$, where $s = 0, 1$, and $t \in T_d$. Letting $D_{\Gamma_{4,5}^{\pm}}(g)$ be the representation matrices for $g \in O_h$, we have

$$D_{\Gamma_5^{\pm}}(t) = D_{\Gamma_4^{\mp}}(t) \tag{2.93}$$

$$D_{\Gamma_5^{\pm}}(\mathcal{I}t) = -D_{\Gamma_4^{\mp}}(\mathcal{I}t). \tag{2.94}$$

Therefore, we can say that Γ_5^+ agrees with the vector representation on T_d, but for $g \notin T_d$, the transformations come with an extra minus sign. Similarly, Γ_5^- agrees with the pseudovector representation on T_d.

In dQSI, equal-time dipolar spin correlations are given by $\langle \vec{E}\vec{E} \rangle$ electric field correlations, which fall off as $1/r^4$. The above results can be used to determine the corresponding (but more subtle) result for oQSI. First, we note that $\tau^z_{\boldsymbol{r}}$ can be viewed as a vector field on the diamond lattice, transforming as a time-reversal odd pseudovector (**i.e.** identical to $\vec{E}$ in dQSI). Therefore, in the long wavelength limit, $\tau^z_{\boldsymbol{r}}$ transforms as Γ_4^+.

To proceed, we need to construct the operator in the (Gaussian) oQSI continuum theory with smallest scaling dimension, that also transforms as Γ_4^+ and is time-reversal odd. We have $\dim \vec{E} = \dim \vec{B} = 2$, and $\dim \partial_\mu = 1$. Also, the derivative ∂_μ transforms as Γ_4^-. For example, we need to consider operators of the form $\partial_\mu \vec{E}_\nu$, which transforms as $\Gamma_4^- \otimes \Gamma_5^+$. Decomposing this into irreducible representations, we find that Γ_4^+ does not appear in the tensor product, and this operator does not contribute to the dipolar spin correlations. Proceeding in this fashion, the desired operator is instead of the form $\mathcal{O}_{\mu\nu\lambda} = \partial_\mu \partial_\nu (\vec{E})_\lambda$, with $\dim \mathcal{O}_{\mu\nu\lambda} = 4$. The corresponding correlations fall off as a power law with exponent twice the scaling dimension, so the oQSI dipolar correlations fall off as $1/r^8$.

This result ignores the role of long-range dipolar interaction, which is potentially significant

in f-electron systems, but its main purpose is to illustrate a sharp difference between dQSI and oQSI. In addition, if one restricts to the XYZ Hamiltonian only (**i.e.** includes no longer-range exchange), the $Z_2 \times Z_2$ symmetry actually implies that dipolar correlations fall off exponentially in oQSI, since both τ^z and τ^x transform non-trivially under $Z_2 \times Z_2$.

2.8 Gauge Mean Field Theory

The formalism of gauge mean field theory (gMFT) for the pyrochlore lattice was introduced in Refs. [72, 73]. This mean-field theory is anchored to the QSI phase known to occur in the easy-axis limit [88], and allows one to assess the competition between QSI and magnetically ordered phases. Here, we adapt the gMFT formalism specifically to the pyrochlore XYZ model.

2.8.1 Slave particles

The ground state of H_{eff} [Eq. (2.90)] is a U(1) quantum spin liquid whose low energy physics is described by compact quantum electrodynamics in $3+1$ dimensions[53, 88]. In the gauge theory language, the "two-in-two-out" spin ice rule becomes Gauss' law, and the $\tilde{\tau}^{\pm}_{\boldsymbol{r}}$ breaks the ice rule by creating electrically charged spinon excitations on neighboring tetrahedra. The $J_{\pm}$ term describes the hopping of spinons on the dual diamond lattice sites.

Following Refs. [72, 73], to make the spinons and gauge field explicit, we enlarge the physical Hilbert space by writing the spin operators as

$$\tilde{\tau}^{+}_{\mathbf{r},\mathbf{r}+\mathbf{e}_i} = \Phi^{\dagger}_{\mathbf{r}} s^{+}_{\mathbf{r},\mathbf{r}+\mathbf{e}_i} \Phi_{\mathbf{r}+\mathbf{e}_i} \tag{2.95}$$

$$\tilde{\tau}^{z}_{\mathbf{r},\mathbf{r}+\mathbf{e}_i} = s^{z}_{\mathbf{r},\mathbf{r}+\mathbf{e}_i}, \tag{2.96}$$

where $\mathbf{r}$ is an A sublattice site of the diamond lattice, and $\mathbf{e}_i$ connects $\mathbf{r}$ to its neighbors on the dual diamond lattice. $\Phi^{\dagger}_{\mathbf{r}}$ ($\Phi_{\mathbf{r}}$) is the spinon creation (annihilation) operator at site $\mathbf{r}$, and $s^{z}_{\mathbf{r}\mathbf{r}'}, s^{\pm}_{\mathbf{r}\mathbf{r}'}$ are spin-1/2 operators that act as gauge fields. Since the spinons are bosonic, we further write $\Phi^{\dagger}_{\mathbf{r}} = e^{i\phi_{\mathbf{r}}}$ ($\Phi_{\mathbf{r}} = e^{-i\phi_{\mathbf{r}}}$), where $\phi_{\mathbf{r}}$ is a 2π periodic angular variable and $\Phi^{\dagger}_{\mathbf{r}}\Phi_{\mathbf{r}} = 1$ by construction. In the above equations, the physical Hilbert space has been enlarged to the the combined space

of the spinons and gauge field. To project back to the physical Hilbert space, we implement the following constraint,

$$Q_{\mathbf{r}} = \eta_{\mathbf{r}} \sum_i s^z_{\mathbf{r},\mathbf{r}+\eta_{\mathbf{r}}\mathbf{e}_i}, \tag{2.97}$$

where $\eta_{\mathbf{r}} = \pm 1$ for $\mathbf{r} \in$ A/B sublattice. Here $Q_{\mathbf{r}}$ is the spinon number operator and satisfies

$$[\phi_{\mathbf{r}}, Q_{\mathbf{r}'}] = i\delta_{\mathbf{r}\mathbf{r}'}. \tag{2.98}$$

The XYZ model Hamiltonian [Eq. (2.89)] can be rewritten as

$$\begin{aligned} H_{\mathrm{XYZ}} &= \frac{J_{zz}}{2}\sum_{\mathbf{r}} Q^2_{\mathbf{r}} - J_{\pm}\sum_{\mathbf{r}}\sum_{i\neq j} \Phi^\dagger_{\mathbf{r}+\eta_{\mathbf{r}}\mathbf{e}_i}\Phi_{\mathbf{r}+\eta_{\mathbf{r}}\mathbf{e}_j} s^{-\eta_{\mathbf{r}}}_{\mathbf{r},\mathbf{r}+\eta_{\mathbf{r}}\mathbf{e}_i} s^{+\eta_{\mathbf{r}}}_{\mathbf{r},\mathbf{r}+\eta_{\mathbf{r}}\mathbf{e}_j} \\ &\quad + \frac{J_{\pm\pm}}{2}\sum_{\mathbf{r}}\sum_{i\neq j}\left(\Phi^\dagger_{\mathbf{r}}\Phi^\dagger_{\mathbf{r}}\Phi_{\mathbf{r}+\eta_{\mathbf{r}}\mathbf{e}_i}\Phi_{\mathbf{r}+\eta_{\mathbf{r}}\mathbf{e}_j} s^{\eta_{\mathbf{r}}}_{\mathbf{r},\mathbf{r}+\eta_{\mathbf{r}}\mathbf{e}_i} s^{\eta_{\mathbf{r}}}_{\mathbf{r},\mathbf{r}+\eta_{\mathbf{r}}\mathbf{e}_j} + h.c.\right) \\ &\quad + \text{constant}. \end{aligned} \tag{2.99}$$

The $J_{\pm\pm}$ term now appears as an interaction between spinons. The above Hamiltonian is manifestly invariant under the local U(1) gauge transformation ($\Phi_{\mathbf{r}} \to \Phi_{\mathbf{r}} e^{-i\chi_{\mathbf{r}}}, s^{\pm}_{\mathbf{r}\mathbf{r}'} \to s^{\pm}_{\mathbf{r}\mathbf{r}'} e^{\pm i(\chi_{\mathbf{r}'}-\chi_{\mathbf{r}})}$).

2.8.2 Mean field theory

Following Ref. [73], we now decouple the Hamiltonian in Eq. (2.99) by mean field theory. As an illustration, the spinon hopping term is decoupled as follows,

$$\begin{aligned} & \Phi^\dagger_{\mathbf{r}+\eta_{\mathbf{r}}\mathbf{e}_i}\Phi_{\mathbf{r}+\eta_{\mathbf{r}}\mathbf{e}_j} s^{-\eta_{\mathbf{r}}}_{\mathbf{r},\mathbf{r}+\eta_{\mathbf{r}}\mathbf{e}_i} s^{+\eta_{\mathbf{r}}}_{\mathbf{r},\mathbf{r}+\eta_{\mathbf{r}}\mathbf{e}_j} \\ \to\ & \left(\Phi^\dagger_{\mathbf{r}+\eta_{\mathbf{r}}\mathbf{e}_i}\Phi_{\mathbf{r}+\eta_{\mathbf{r}}\mathbf{e}_j} - \langle\Phi^\dagger_{\mathbf{r}+\eta_{\mathbf{r}}\mathbf{e}_i}\Phi_{\mathbf{r}+\eta_{\mathbf{r}}\mathbf{e}_j}\rangle\right)\langle s^{-\eta_{\mathbf{r}}}_{\mathbf{r},\mathbf{r}+\eta_{\mathbf{r}}\mathbf{e}_i}\rangle\langle s^{+\eta_{\mathbf{r}}}_{\mathbf{r},\mathbf{r}+\eta_{\mathbf{r}}\mathbf{e}_j}\rangle \\ +\ & \langle\Phi^\dagger_{\mathbf{r}+\eta_{\mathbf{r}}\mathbf{e}_i}\Phi_{\mathbf{r}+\eta_{\mathbf{r}}\mathbf{e}_j}\rangle\left(s^{-\eta_{\mathbf{r}}}_{\mathbf{r},\mathbf{r}+\eta_{\mathbf{r}}\mathbf{e}_i}\langle s^{+\eta_{\mathbf{r}}}_{\mathbf{r},\mathbf{r}+\eta_{\mathbf{r}}\mathbf{e}_j}\rangle + \langle s^{-\eta_{\mathbf{r}}}_{\mathbf{r},\mathbf{r}+\eta_{\mathbf{r}}\mathbf{e}_i}\rangle s^{+\eta_{\mathbf{r}}}_{\mathbf{r},\mathbf{r}+\eta_{\mathbf{r}}\mathbf{e}_j} - \langle s^{-\eta_{\mathbf{r}}}_{\mathbf{r},\mathbf{r}+\eta_{\mathbf{r}}\mathbf{e}_i}\rangle\langle s^{+\eta_{\mathbf{r}}}_{\mathbf{r},\mathbf{r}+\eta_{\mathbf{r}}\mathbf{e}_j}\rangle\right). \end{aligned} \tag{2.100}$$

Similar decouplings can also be made to the $J_{\pm\pm}$ term. The microscopic Hamiltonian is now reduced to mean field Hamiltonians for both spinon sector H_Φ and gauge sector H_s,

$$H_{\mathrm{XYZ}} \to H_{\mathrm{gMFT}} = H_\Phi + H_s. \tag{2.101}$$

Here, H_Φ is given by

$$\begin{aligned} H_\Phi &= \frac{J_{zz}}{2}\sum_{\mathbf{r}} Q_{\mathbf{r}}^2 - J_\pm \Delta^2 \sum_{\mathbf{r}} \Phi^\dagger_{\mathbf{r}+\eta_{\mathbf{r}}\mathbf{e}_i}\Phi_{\mathbf{r}+\eta_{\mathbf{r}}\mathbf{e}_j} \\ &+\frac{J_{\pm\pm}\Delta^2}{2}\sum_{\mathbf{r}\in \mathrm{A}}\sum_{i\neq j}\Big[\Phi^\dagger_{\mathbf{r}}\Phi^\dagger_{\mathbf{r}}\chi^{\mathrm{B}}_{ij} + \chi_0^{\mathrm{A}*}\Phi_{\mathbf{r}+\mathbf{e}_i}\Phi_{\mathbf{r}+\mathbf{e}_j} + 2\big(\Phi^\dagger_{\mathbf{r}}\Phi_{\mathbf{r}+\mathbf{e}_i}\xi_j + \Phi^\dagger_{\mathbf{r}}\Phi_{\mathbf{r}+\mathbf{e}_j}\xi_i\big) + h.c.\Big] \\ &+\frac{J_{\pm\pm}\Delta^2}{2}\sum_{\mathbf{r}\in \mathrm{B}}\sum_{i\neq j}\Big[\Phi^\dagger_{\mathbf{r}}\Phi^\dagger_{\mathbf{r}}\chi^{\mathrm{A}}_{ij} + \chi_0^{\mathrm{B}*}\Phi_{\mathbf{r}-\mathbf{e}_i}\Phi_{\mathbf{r}-\mathbf{e}_j} + 2\big(\Phi^\dagger_{\mathbf{r}}\Phi_{\mathbf{r}-\mathbf{e}_i}\xi^*_j + \Phi^\dagger_{\mathbf{r}}\Phi_{\mathbf{r}-\mathbf{e}_j}\xi^*_i\big) + h.c.\Big]. \end{aligned} \tag{2.102}$$

We have chosen a mean-field state where the spinons feel zero magnetic flux through each hexagon, as appropriate for $J_{\mathrm{ring}} < 0$ and $J_\pm < 0$, and have thus chosen a gauge in which the spinon hopping is uniform. We have introduced the sublattice mixing parameters,

$$\xi_i \equiv \langle \Phi^\dagger_{\mathbf{r}}\Phi_{\mathbf{r}+\eta_{\mathbf{r}}\mathbf{e}_i}\rangle \quad \text{for} \quad \mathbf{r}\in \mathrm{A}, \tag{2.103}$$

the onsite pairing parameters,

$$\chi_0^{\mathrm{A}} = \langle \Phi_{\mathbf{r}}\Phi_{\mathbf{r}}\rangle \quad \text{for} \quad \mathbf{r}\in \mathrm{A}, \tag{2.104}$$

$$\chi_0^{\mathrm{B}} = \langle \Phi_{\mathbf{r}}\Phi_{\mathbf{r}}\rangle \quad \text{for} \quad \mathbf{r}\in \mathrm{B}, \tag{2.105}$$

and the inter-site pairing

$$\chi^{\mathrm{A}}_{ij} = \langle \Phi_{\mathbf{r}-\mathbf{e}_i}\Phi_{\mathbf{r}-\mathbf{e}_j}\rangle \quad \text{for} \quad \mathbf{r}\in \mathrm{B}, \tag{2.106}$$

$$\chi^{\mathrm{B}}_{ij} = \langle \Phi_{\mathbf{r}+\mathbf{e}_i}\Phi_{\mathbf{r}+\mathbf{e}_j}\rangle \quad \text{for} \quad \mathbf{r}\in \mathrm{A}. \tag{2.107}$$

Finally, the parameter Δ is defined as $\Delta = \langle s^\pm_{\mathbf{r},\mathbf{r}\pm\mathbf{e}_i}\rangle$ is chosen uniformly on all bonds due to the above gauge choice. H_s only contains Zeeman terms for $s^\mu_{\mathbf{r}\mathbf{r}'}$ and is trivially solved, leading to $\Delta = 1/2$.

The ground state of H_Φ in Eq. (2.102) is then solved self-consistently under the constraint $\Phi^\dagger_{\mathbf{r}}\Phi_{\mathbf{r}} = 1$. The gMFT ground state is selected by optimizing the variational energy $\langle H_{\mathrm{XYZ}}\rangle$ in Eq. (2.99). Magnetic ordering appears when the spinon field is condensed with the physical order parameter given by $\langle \tilde{\tau}^+_{\mathbf{r},\mathbf{r}+\mathbf{e}_i}\rangle = \langle \Phi^\dagger_{\mathbf{r}}\rangle\langle s^+_{\mathbf{r},\mathbf{r}+\mathbf{e}_i}\rangle\langle \Phi_{\mathbf{r}+\mathbf{e}_i}\rangle$. We find that, the pairing parameters always

vanish when the spinon field is not condensed, indicating the absence of an intermediate Z_2 quantum spin liquid in this mean field approach. Therefore, the phase boundary of the phase diagram in the main text is obtained when the spinon field condensation takes place.

2.9 Conclusion and future work

The neutron data suggest the existence of dipolar-octupolar doublets in pyrochlore material. The dipolar component can be measured easily in the experiment. One important question is to understand the possible physical effect induced by the octupolar exchange interaction. How to probe the octupolar fluctuation is a challenging and exciting subject for future study.

Also, the physical effects of the dipolar-octupolar doublets to transport measurement is also interesting. How to understand the quantum nature of dipolar-octupolar doublets and its coupling with the itinerant electron is also important to study related materials.

Chapter 3

Theory of quantum Kagome ice and vison zero modes[1]

3.1 Introduction

Quantum spin liquids (QSLs) are remarkable zero-temperature phases of insulating spin systems.[101, 102, 18] These states lack any sort of symmetry-breaking order, but instead exhibit long-range quantum entanglement. Some QSLs are stable phases with gapless excitations, while others are gapped and topologically ordered, supporting fractional excitations, as in fractional quantum Hall liquids. Over the last several years, a number of candidate materials for gapless QSLs have emerged (see [[18]] and references therein). Recent Knight shift[103] and inelastic neutron scattering[104] measurements suggest a gapped spin liquid ground state in $ZnCu_3(OD)_6Cl_2$, but interpretation of these results is complicated by significant impurity effects, while other measurements point to a gapless state [18, 105, 106]. It remains an important problem to find candidate materials for gapped QSLs.

In a closely related development, numerical studies of simple and fairly realistic quantum spin models have found evidence for two types of gapped QSLs, namely Z_2 QSLs,[107, 108, 109, 110, 111, 112, 113, 114, 115] and chiral spin liquids.[**?**, **?**] There is evidence for a Z_2 QSL in the $S = 1/2$ kagome Heisenberg antiferromagnet,[116, 117, 118, 119] although there are also contrary indications that the ground state may be gapless.[120, 121, 122, 123] In the same model, a chiral spin liquid phase arises upon adding second and third neighbor interactions, with or without XXZ

[1] This section has been published as a portion of Yi-Ping Huang and Michael Hermele, Phys. Rev. B 95, 075130,[49] copyright 2017 American Physical Society, and is reproduced here in accord with the copyright policies of the American Physical Society.

anisotropy.[124, 125, 126] Recently, in the $S = 1/2$ $J_1 - J_2$ triangular Heisenberg antiferromagnet, density matrix renormalization group studies have found evidence of a gapped spin liquid,[127, 128] although a variational wave function approach favors a gapless spin liquid.[129] These works raise the prospects for finding gapped QSLs in real materials, and provide clues where to look for such states. However, especially given that gapped QSLs are not conclusively established in some of these models, it continues to be important to identify simple, fairly realistic candidate models for gapped QSLs.

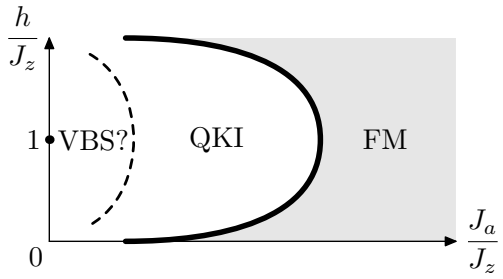

Figure 3.1: Schematic zero-temperature phase diagram of the XYZh model, based on the quantum Monte Carlo results of Ref. [50], showing quantum kagome ice (QKI), ferromagnetic (FM) and valence bond solid (VBS) states. Only $h > 0, J_a > 0$ is shown, as the phase diagram is symmetric under $h \to -h$ and J_a changes sign under unitary $\pi/2$ spin rotation. At small J_a/J_z, the system can be mapped to a honeycomb lattice quantum dimer model where we believe VBS order is the most likely possibility,[130] although VBS order was not observed in Ref. [50]; this point is discussed further in the text. The phase transition from QKI to FM was found to be first-order.

In an exciting addition to this body of work, Carasquilla, Hao and Melko (CHM) have identified a gapped, quantum disordered phase in a $S = 1/2$ XYZ model on the kagome lattice in a z-axis Zeeman magnetic field (XYZh model).[50] CHM proposed this state, dubbed quantum kagome ice, to be a gapped Z_2 QSL.

The XYZh model has potential relevance to f-electron pyrochlore magnets where effective spin-1/2 degrees of freedom transform not as magnetic dipoles, but instead as dipolar-octupolar Kramers doublets.[48] Together with G. Chen, we showed that such systems are described by a XYZ model, which was argued to be particularly relevant for $A_2B_2O_7$ pyrochlores with A = Nd;[48] experiments have found evidence for dipolar-octupolar doublets in some such systems.[83, 131, 132, 133] Following prior work on the "kagome ice" state of classical spin ice pyrochlores,[134,

135, 136, 137, 138, 139, 140, 141] CHM noted that the pyrochlore XYZ model descends to the XYZh model on approximately decoupled kagome layers upon applying a magnetic field.

In more detail, CHM considered the Hamiltonian

$$\begin{aligned} \mathcal{H}_{\text{XYZh}} &= \sum_{\langle \boldsymbol{r},\boldsymbol{r}'\rangle} J_z S^z_{\boldsymbol{r}} S^z_{\boldsymbol{r}'} - h\sum_{\boldsymbol{r}} S^z_{\boldsymbol{r}} \\ &- \sum_{\langle \boldsymbol{r},\boldsymbol{r}'\rangle} \left[\frac{J_\perp}{2}\left(S^+_{\boldsymbol{r}} S^-_{\boldsymbol{r}'} + h.c.\right) + \frac{J_a}{2}\left(S^+_{\boldsymbol{r}} S^+_{\boldsymbol{r}'} + h.c.\right)\right] \end{aligned} \tag{3.1}$$

where $J_z > 0$, $\boldsymbol{r}$ labels Kagome lattice sites, and $\langle \boldsymbol{r}, \boldsymbol{r}'\rangle$ denotes nearest-neighbor bonds. CHM set $J_\perp = 0$ and used quantum Monte Carlo to obtain the phase diagram as a function of J_a/J_z and h/J_z, finding two "lobes" of QKI centered at $h/J_z = \pm 1$, as shown in Fig. 3.1

CHM examined various candidate orders in the QKI state and concluded that it lacks symmetry-breaking order. Moreover, following prior works,[142, 72, 73] they showed that $\mathcal{H}_{\text{XYZh}}$ can be exactly rewritten as a U(1) gauge theory, with the J_a term a pair-hopping of spinons that can lead to condensation of spinon pairs and thus to a Z_2 QSL. Based on this insight, CHM described how to obtain this state within a gauge mean-field treatment.[72]

For small J_a/J_z, the XYZh model onto a honeycomb lattice quantum dimer model, which can be seen using degenerate perturbation theory. The phase diagram of two-dimensional bipartite dimer models, including on the honeycomb lattice,[130] is dominated by different types of valence bond solid (VBS) order, and we believe that a VBS state is likely present within the lobe for sufficiently small J_a. However, we are aware of no general argument ruling out, for instance, a Z_2 QSL or a trivial quantum paramagnet in the honeycomb dimer model. Indeed, it has recently been shown that a trivial paramagnet can occur for $S = 1/2$ spins on the honeycomb lattice. This is likely also possible for the dimer model, because it can viewed as an effective theory for such a spin model. It is important to note that CHM did not observe VBS order, but this may be due to a small temperature scale or problems with equilibration at small J_a.

The results of CHM are consistent with the hypothesis that quantum kagome ice is a Z_2 QSL, but this has not been directly confirmed or ruled out. No Lieb-Schultz-Mattis type theorem[143, 144, 145] is believed to hold for the XYZh model, so that a trivial quantum paramagnet is expected

to be a possible ground state[2] and is also consistent with the results of CHM. It is therefore important to devise signatures that can distinguish the Z_2 QSL and trivial paramagnet, as well as other possible states.

In this paper, we derive an effective gauge theory of QKI as a Z_2 QSL, study its properties, and use it to make a striking prediction that we expect can be tested in future quantum Monte Carlo studies. In particular, we show that lattice disclination defects host vison zero modes, **i.e.** there is no energy cost to insert a vison at a disclination. The resulting degeneracies only require the Z_2 Ising symmetry of the XYZh model for their protection, which is remarkable because a unitary Z_2 symmetry cannot protect degeneracies of local degrees of freedom. The vison zero modes lead to a Curie spin susceptibility localized at the defects. In addition, in a system without boundary where N_{dis} disclinations host vison zero modes, there are $2^{N_{dis}}/2$ degenerate states associated with the zero modes, where the factor of $1/2$ comes from the global constraint of an even number of visons. The resulting $(N_{dis}-1)\ln 2$ contribution to the entropy directly distinguishes vison zero modes from local doublets bound to disclinations, which would have a degeneracy of $2^{N_{dis}}$. We also discuss other possible signatures related to the symmetry properties of spinon and vison excitations, both within the Z_2 spin liquid phase and at phase transitions to nearby symmetry-breaking phases.

In Sec. 3.2 we derive the effective Z_2 gauge theory, starting from an exact rewriting of the XYZh model as a U(1) gauge theory.[50, 142, 72, 73] We then discuss the role of symmetry in the Z_2 QSL (Sec. 3.3). We find that the spinon has non-trivial symmetry fractionalization, while the symmetry fractionalization of the vison is trivial; the computation of the symmetry fractionalization is discussed in Appendix 3.7. Section 3.4 describes the vison zero modes at lattice disclinations their signatures in spin susceptibility and entropy. Other properties of the Z_2 QSL, including phase transitions to nearby phases, are discussed in Sec. 3.5, and the paper concludes with a brief discussion (Sec. 3.6).

We would like to note other current work on the theory the spin liquid state in the XYZh model, using an approach complementary to our own.[146]

[2] Our effective theory allows us to confirm this expectation.

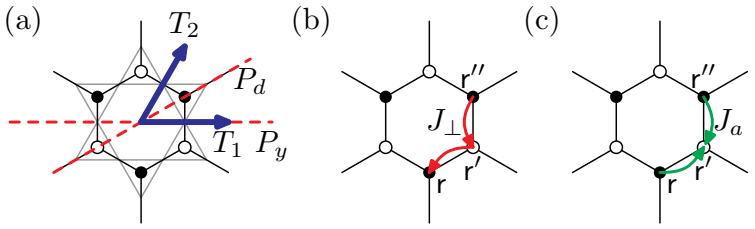

Figure 3.2: (a) The sites of the kagome lattice, where spins of the XYZh model reside, are identified with nearest-neighbor links of the honeycomb lattice. Honeycomb sites, which correspond to kagome triangles, naturally divide into A and B sublattices, shown as open and closed circles, due to the bipartite nature of the honeycomb lattice. The generators of the $p6m$ space group are shown, with P_d and P_y reflections (dashed lines) and T_1 and T_2 translations (thick arrows). (b) and (c) illustrate the hopping processes in the U(1) gauge theory that correspond to $J_\perp$ and J_a terms, respectively.

3.2 Derivation of effective gauge theory

Our effective gauge theory is based on an exact rewriting of the XYZh model as a U(1) gauge theory. Before getting into details, we motivate the rewriting by considering the classical limit $J_\perp = J_a = 0$ and $h = J_z$, where the ground states are configurations of $S^z_{\mathbf{r}}$ with two spins up and one spin down on every triangle. Kagome sites correspond to nearest-neighbor links of the dual honeycomb lattice, while kagome triangles correspond to honeycomb sites (Fig. 3.2a). We can view up-up-down spin configurations as dimer coverings of the honeycomb lattice, associating down spin (up spin) with presence (absence) of a dimer. Moving slightly away from the classical case by allowing $0 \neq J_a, J_\perp \ll J_z$, we obtain a honeycomb quantum dimer model, which is a U(1) gauge theory.

Now we proceed to rewrite the XYZh model as a U(1) gauge theory, without making any assumptions about the size of the various couplings in the Hamiltonian. This rewriting follows CHM,[50] who in turn followed Refs. [142, 72, 73]. We first introduce the Hilbert space and operators of the gauge theory, and then describe their relationship to the Hilbert space and spin operators of the XYZh model. We label the sites of the honeycomb lattice by sans serif letters r. On each honeycomb link we place a U(1) quantum rotor, with number $e_{\mathsf{r}\mathsf{r}'}$ that will be the electric field, and phase $a_{\mathsf{r}\mathsf{r}'}$ that will be the vector portential. On the same link, these operators satisfy the commutation relation $[a_{\mathsf{r}\mathsf{r}'}, e_{\mathsf{r}\mathsf{r}'}] = i$, and we define $e_{\mathsf{r}'\mathsf{r}} = -e_{\mathsf{r}\mathsf{r}'}$ (similarly for $a_{\mathsf{r}\mathsf{r}'}$). On honeycomb

sites we also place U(1) quantum rotors with number n_{r} and phase θ_{r}, satisfying $[\theta_{\mathsf{r}}, n_{\mathsf{r}}] = i$. The site degrees of freedom are matter fields carrying the U(1) gauge charge. To fully specify the gauge theory Hilbert space we need to specify the Gauss' law constraint, which we take to be

$$(\mathrm{div}\, e)_{\mathsf{r}} = 2\eta_{\mathsf{r}} + Q_{\mathsf{r}}, \tag{3.2}$$

where $Q_{\mathsf{r}} \equiv n_{\mathsf{r}}$ is the gauge charge at r, $2\eta_{\mathsf{r}}$ is a static background charge, and we have defined η_{r} to be 1 (-1) for r in the A (B) sublattice. The lattice divergence is defined by $(\mathrm{div}\, e)_{\mathsf{r}} = \sum_{\mathsf{r}' \sim \mathsf{r}} e_{\mathsf{r}\mathsf{r}'}$, where the sum is over the three neighbors of r.

The gauge theory Hilbert space is identical to that of the spin model, if we impose the additional "hardcore" constraint $e_{\mathsf{r}\mathsf{r}'} = 0, 1$, with r in the A sublattice. Then we impose the relation

$$e_{\mathsf{r}\mathsf{r}'} = \eta_{\mathsf{r}}(S^z_{\mathsf{r}\mathsf{r}'} + 1/2), \tag{3.3}$$

where we take $S^z_{\mathsf{r}\mathsf{r}'} \equiv S^z_{\mathsf{r}'\mathsf{r}}$. This says that Ising spin configurations are the same as electric field configurations. Gauss' law then determines Q_{r}, giving

$$Q_{\mathsf{r}} = \eta_{\mathsf{r}}\big(\sum_{\boldsymbol{r} \in \triangle} S^z_{\boldsymbol{r}} - 1/2\big), \tag{3.4}$$

where $\triangle$ is the triangle whose center is r. We see that Q_{r} is zero for triangles in an up-up-down spin configuration, and measures the deviation of the total spin on a triangle from $1/2$. In fact, we included the background charge $2\eta_{\mathsf{r}}$ in Gauss' law in order to make this property hold.

To complete the mapping between the gauge theory and spin model, we write

$$S^+_{\mathsf{r}\mathsf{r}'} = \exp\big(i\eta_{\mathsf{r}}(\theta_{\mathsf{r}} - \theta_{\mathsf{r}'} + a_{\mathsf{r}\mathsf{r}'})\big), \tag{3.5}$$

where again we take $S^+_{\mathsf{r}\mathsf{r}'} \equiv S^+_{\mathsf{r}'\mathsf{r}}$. This formula has a simple interpretation, namely that $S^+_{\mathsf{r}\mathsf{r}'}$ hops a gauge charge between two neighboring sites of the honeycomb lattice.

Taking $h = J_z$ for simplicity, which puts us at the center of one of the lobes of QKI, in terms

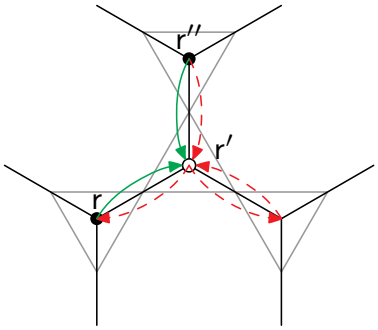

Figure 3.3: Illustration of how J_a and $J_\perp$ terms can combine to give nearest-neighbor charge-two hopping. Three different J_a coordinated hopping processes are shown. Two of these are shown with red dashed arrows, one with green solid arrows. Acting in succession with the two red/dashed processes gives a charge-one hopping from r'' to r, the same process as the $J_\perp$ term. Combining this with the green/solid process then gives a charge-two hopping from r'' to r'.

of the gauge theory degrees of freedom the XYZh Hamiltonian becomes

$$\begin{aligned}\mathcal{H}_{\text{gauge}} &= \frac{J_z}{2}\sum_{\mathsf{r}} n_{\mathsf{r}}^2 + U\sum_{\mathsf{r}\in A}\sum_{\mathsf{r}'\sim\mathsf{r}}(e_{\mathsf{r}\mathsf{r}'}-1/2)^2 \\ &- J_\perp \sum_{\langle\langle \mathsf{r},\mathsf{r}''\rangle\rangle} \cos(\theta_{\mathsf{r}}-\theta_{\mathsf{r}''}+a_{\mathsf{r}\mathsf{r}'}+a_{\mathsf{r}'\mathsf{r}''}) \\ &- J_a \sum_{\langle\langle \mathsf{r},\mathsf{r}''\rangle\rangle} \cos(2\theta_{\mathsf{r}'}-\theta_{\mathsf{r}}-\theta_{\mathsf{r}''}+a_{\mathsf{r}'\mathsf{r}}+a_{\mathsf{r}'\mathsf{r}''}).\end{aligned} \tag{3.6}$$

The sum in the latter two terms is over pairs of next-nearest neighbor honeycomb sites r,r'', with r' the site "in between" r and r'' as shown in Fig. 3.2b,c. In order to obtain a useful effective theory, we have softened the hardcore constraint on electric fields with the U term, which restores this constraint in the limit $U\to\infty$, where the original spin model is recovered. We see that the $J_\perp$ term is a next-nearest neighbor hopping of gauge charges (Fig 3.2b). The J_a term is a coordinated hopping, which moves unit charges from sites r and r'' together into site r' (Fig. 3.2c).

The coordinated J_a hopping can loosely be thought of as motion of a charge-two object. As was suggested for very similar U(1) gauge theories on the pyrochlore lattice,[73] and in the present context by CHM,[50] it is thus reasonable that J_a may drive condensation of a charge-two field, while leaving single charge excitations gapped. Such a condensation breaks the U(1) gauge structure down to Z_2,[147] thus leading to a Z_2 spin liquid.

We note that a nearest-neighbor charge-two hopping can indeed be generated from the J_a hopping process, or from J_a and $J_\perp$ processes together, as illustrated in Fig. 3.3. This motivates us to introduce a charge-two field with number N_{r} and phase Θ_{r}, which represents a bound state of two unit θ_{r} gauge charges. We add the following terms to the Hamiltonian:

$$\begin{aligned}\delta\mathcal{H} &= u_2\sum_{\mathsf{r}} N_{\mathsf{r}}^2 - \Delta\sum_{\mathsf{r}}\cos(\Theta_{\mathsf{r}}-2\theta_{\mathsf{r}}) \\ &- t_2\sum_{\langle\mathsf{r}\mathsf{r}'\rangle}\cos(\Theta_{\mathsf{r}}-\Theta_{\mathsf{r}'}+2a_{\mathsf{r}\mathsf{r}'}) - K\sum_{\hexagon}\cos((\nabla\times a)_{\hexagon}).\end{aligned} \tag{3.7}$$

The first term is a repulsive interaction for the new charge-two field. The second term corresponds to a process where two unit charges convert to a single double charge, and the third term is nearest-neighbor hopping of double charges. The last term is a Maxwell term for the U(1) gauge field, where

the sum is over honeycomb hexagons and $(\nabla \times a)_{\hexagon}$ is the discrete line integral of $a_{\mathsf{rr}'}$ around the perimeter of a hexagon. The discrete line integral of $a_{\mathsf{rr}'}$ around the perimeter of a hexagon is defined as

$$(\nabla \times a)_{\hexagon} = \sum_{\mathsf{rr}' \in \hexagon} a_{\mathsf{rr}'}. \tag{3.8}$$

The Maxwell term suppresses U(1) gauge fluctuations, and is the leading dynamical term generated in degenerate perturbation theory when $J_\perp, J_a \ll J_z$. While we do not work in that limit, the fact that the Maxwell term is generated there makes it reasonable to add it explicitly to our effective Hamiltonian. For consistency, we also redefine $Q_{\mathsf{r}} \equiv n_{\mathsf{r}} + 2N_{\mathsf{r}}$ in Eq. (3.2).

We now take the Δ and t_2 terms in $\delta\mathcal{H}$ to be large. The t_2 term drives condensation of the charge-two field, while Δ is taken large for convenience. Provided K is sufficiently large, this drives the system into the Z_2 QSL phase and allows us to obtain an effective gauge theory describing it.

Taking t_2 large and treating the cosine as a constraint, we have

$$a_{\mathsf{rr}'} = \frac{1}{2}\Theta_{\mathsf{r}'} - \frac{1}{2}\Theta_{\mathsf{r}} + \alpha_{\mathsf{rr}'}, \tag{3.9}$$

where $\alpha_{\mathsf{rr}'}$ takes values $0, \pi$. There is an ambiguity in multiplying a U(1) phase by $1/2$, which is the same as the ambiguity in defining the square root for complex numbers. We pick a branch by associating a U(1) phase ϕ with the corresponding real number lying in the interval $[-\pi, \pi)$, for which multiplication by $1/2$ is defined in the usual way.

The other effect of treating the t_2 term as a constraint is that only operators commuting with the term survive in the low-energy Hilbert space. In particular, $e_{\mathsf{rr}'}$ does not commute with the constraint, but

$$\sigma^x_{\mathsf{rr}'} \equiv \exp(i\pi e_{\mathsf{rr}'}) \tag{3.10}$$

does, and becomes the Z_2 electric field. We also define the Z_2 vector potential $\sigma^z_{\mathsf{rr}'} \equiv \exp(i\alpha_{\mathsf{rr}'})$, which anticommutes with $\sigma^x_{\mathsf{rr}'}$ on the same link, justifying the Pauli matrix notation.

Similarly, taking Δ large gives the constraint

$$\theta_{\mathsf{r}} = \frac{1}{2}\Theta_{\mathsf{r}} + t_{\mathsf{r}}, \tag{3.11}$$

where $t_{\mathsf{r}} = 0, \pi$ and we define $\tau^z_{\mathsf{r}} \equiv \exp(it_{\mathsf{r}})$. We also introduce $\tau^x_{\mathsf{r}} \equiv \exp(i\pi n_{\mathsf{r}})$, which, unlike n_{r} or N_{r}, commutes with the Δ term.

To write the low-energy effective Hamiltonian, those terms commuting with the constraints can straightforwardly be simplified using Eqs. (3.9,3.11). Terms not commuting with the constraint need to be replaced by new terms acting within the low-energy Hilbert space. Rather than try to determine those terms systematically, we simply write down the simplest such terms consistent with symmetry (taking input from Sec. 3.3), and use physical arguments to further constrain the corresponding parameters. The effective Hamiltonian is

$$\begin{aligned} \mathcal{H}_{\text{eff}} &= -K \sum_p B_p - J \sum_{\langle\langle \mathsf{r},\mathsf{r}'' \rangle\rangle} \tau^z_{\mathsf{r}} \sigma^z_{\mathsf{r}\mathsf{r}'} \sigma^z_{\mathsf{r}'\mathsf{r}''} \tau^z_{\mathsf{r}''} \\ &- v \sum_{\langle \mathsf{r}\mathsf{r}' \rangle} \sigma^x_{\mathsf{r}\mathsf{r}'} - u \sum_{\mathsf{r}} \tau^x_{\mathsf{r}}, \end{aligned} \tag{3.12}$$

where the first sum is over hexagonal plaquettes p and $B_p \equiv \prod_{\mathsf{r}\mathsf{r}' \in p} \sigma^z_{\mathsf{r}\mathsf{r}'}$. The first term is obtained directly from the K term in $\delta\mathcal{H}$, and the J term from the $J_\perp$ and J_a terms of the original Hamiltonian. The latter two terms are the simplest symmetry-allowed terms giving dynamics to $\sigma^z_{\mathsf{r}\mathsf{r}'}$ and τ^z_{r}, in accord with the discussion above. The Z_2 gauge constraint is obtained by exponentiating Eq. (3.2) and is $\prod_{\mathsf{r}' \sim \mathsf{r}} \sigma^x_{\mathsf{r}\mathsf{r}'} = \tau^x_{\mathsf{r}}$. It should be noted that the background U(1) gauge charge $2\eta_{\mathsf{r}}$ has dropped out.

We are free to choose $u, v > 0$ by making unitary transformations $\tau^x \to -\tau^x$ ($\sigma^x \to -\sigma^x$) to change the sign of u (v). Each of these transformations introduces a minus sign into the gauge constraint, which becomes $\prod_{\mathsf{r}' \sim \mathsf{r}} \sigma^x_{\mathsf{r}\mathsf{r}'} = \pm\tau^x_{\mathsf{r}}$, with an undetermined sign that we now fix below by a physical argument.

First, we need to describe the excitations of the Z_2 spin liquid phase that the model enters when K is sufficiently large compared to the other terms in $\mathcal{H}_{\text{eff}}$. This puts the Z_2 gauge field in its deconfined phase. There are two types of gapped excitations: spinons carrying the Z_2 gauge charge, and visons carrying the Z_2 gauge flux. $\tau^x = -1$ ($+1$) indicates the presence (absence) of a spinon, so that u controls the spinon gap. Visons reside on hexagons with $B_p = -1$.

To fix the sign of the gauge constraint, we recall our expectation that a VBS state is the most

likely possibility to occur adjacent to the Z_2 spin liquid for $J_a, J_\perp \ll J_z$, based on the mapping to the honeycomb quantum dimer model (see Sec. 3.1). We suppose that this VBS can be accessed by condensation of either the spinons or visons of the Z_2 spin liquid. In the same limit where VBS occurs, spinons correspond to defect triangles that violate the up-up-down constraint, and thus have a large energy gap. Therefore vison condensation is the only option to access the VBS.

We can integrate out spinons to obtain a pure Z_2 gauge theory, keeping only the K and u terms of $\mathcal{H}_{\text{eff}}$, with gauge constraint $\prod_{\mathsf{r}'\sim\mathsf{r}} \sigma^x_{\mathsf{r}\mathsf{r}'} = \pm 1$, corresponding to presence (-1) or absence $(+1)$ of a background gauge charge. It should be noted that this background charge has no direct connection to the background charge $2\eta_{\mathsf{r}}$ in the U(1) gauge theory. Visons reside on sites of the dual triangular lattice (honeycomb hexagons), and feel a background charge as a π flux. With zero flux, the minimum of the vison dispersion lies at the Γ point of the Brillouin zone, and we expect visons to condense at zero momentum if v is made sufficiently large. This leads to a confined phase without breaking lattice symmetry. On the other hand, visons hopping in background π flux have degenerate dispersion minima at the zone corners (K points), so that lattice symmetries are necessarily broken when large enough v drives their condensation, and the confined phase is a VBS. Therefore we take the gauge constraint to be

$$\prod_{\mathsf{r}'\sim\mathsf{r}} \sigma^x_{\mathsf{r}\mathsf{r}'} = -\tau^x_{\mathsf{r}}. \tag{3.13}$$

It should be noted that the presence of background Z_2 gauge charge is a non-universal feature of our effective theory, that in principle can be changed by tuning parameters (although it is not clear which parameter to tune in the XYZh model to achieve this). If v is reduced and eventually made negative, we can make a unitary transformation $\sigma^x_{\mathsf{r}\mathsf{r}'} \to -\sigma^x_{\mathsf{r}\mathsf{r}'}$ to again make the coefficient of σ^x negative in $\mathcal{H}_{\text{eff}}$, and remove the background charge from Gauss' law. This can be done while remaining within the Z_2 spin liquid phase, and can be thought of as simply reversing the sign of the vison hopping matrix element. From this new point in parameter space of the Z_2 spin liquid, it is clearly possible to condense visons at zero momentum and enter a trivial phase. This shows that a trivial quantum paramagnet is indeed possible in the XYZh model, although to access this phase

it may be necessary to add additional symmetry-allowed terms to the Hamiltonian. We remark that this situation is distinct from that occurring in effective theories for other Z_2 spin liquids. For instance, a gapped Z_2 spin liquid in the $S = 1/2$ kagome Heisenberg model [with SU(2) symmetry] necessarily has a background Z_2 gauge charge, which is tied to the odd number of $S = 1/2$ moments in each unit cell and to the impossibility of a trivial quantum paramagnet in such a model.[148]

We emphasize that the sign of the gauge constraint, as a non-universal property, does not affect the presence of vison zero modes at disclinations.

3.3 Symmetry in the Z_2 spin liquid

The symmetry group of the XYZh model is $G = Z_2^I \times Z_2^T \times p6m$, where Z_2^I (generated by $\mathcal{I}$) is the Ising spin symmetry given by a π rotation about the z-axis in spin space, and $p6m$ is the space group of the kagome lattice. While the Zeeman field h breaks the usual time reversal symmetry for spin systems, the XYZh Hamiltonian does enjoy a modified time reversal symmetry (Z_2^T, generated by $\mathcal{T}$) that leaves both $S^z_{\boldsymbol{r}}$ and $S^+_{\boldsymbol{r}}$ invariant; this is the natural time reversal operation if we view the XYZh model as a hardcore boson system.

	$S^z_{\boldsymbol{r}}$	$S^{\pm}_{\boldsymbol{r}}$	θ_{r}	n_{r}	$a_{\mathsf{rr}'}$	$e_{\mathsf{rr}'}$
g	$S^z_{g(\boldsymbol{r})}$	$S^{\pm}_{g(\boldsymbol{r})}$	$\epsilon_g\theta_{g(\mathsf{r})}$	$\epsilon_g n_{g(\mathsf{r})}$	$\epsilon_g a_{g(\mathsf{r}),g(\mathsf{r}')}$	$\epsilon_g e_{g(\mathsf{r}),g(\mathsf{r}')}$
$\mathcal{I}$	$S^z_{\boldsymbol{r}}$	$-S^{\pm}_{\boldsymbol{r}}$	θ_{r}	n_{r}	$a_{\mathsf{rr}'} + \pi$	$e_{\mathsf{rr}'}$
$\mathcal{T}$	$S^z_{\boldsymbol{r}}$	$S^{\pm}_{\boldsymbol{r}}$	$-\theta_{\mathsf{r}}$	n_{r}	$-a_{\mathsf{rr}'}$	$e_{\mathsf{rr}'}$
	-	-	τ^z_{r}	τ^x_{r}	$\sigma^z_{\mathsf{rr}'}$	$\sigma^x_{\mathsf{rr}'}$
g	-	-	$\tau^z_{g(\mathsf{r})}$	$\tau^x_{g(\mathsf{r})}$	$\sigma^z_{g(\mathsf{r}),g(\mathsf{r}')}$	$\sigma^x_{g(\mathsf{r}),g(\mathsf{r}')}$
$\mathcal{I}$	-	-	τ^z_{r}	τ^x_{r}	$-\sigma^z_{\mathsf{rr}'}$	$\sigma^x_{\mathsf{rr}'}$
$\mathcal{T}$	-	-	τ^z_{r}	τ^x_{r}	$\sigma^z_{\mathsf{rr}'}$	$\sigma^x_{\mathsf{rr}'}$

Table 3.1: Action of symmetry operations $g, \mathcal{I}, \mathcal{T}$ on the operators of the spin model and U(1) gauge theory (above double line), and Z_2 effective gauge theory (below double line). Here g is an element of the $p6m$ space group and $\epsilon_g = +1$ (-1) when g preserves (exchanges) the A and B honeycomb sublattices. The transformations of Θ_{r} and N_{r} are the same as those of θ_{r} and n_{r}.

Table 3.1 shows how the variables of the spin model and U(1) and Z_2 gauge theories transform under symmetry. Because θ_{r} and $a_{\mathsf{rr}'}$ are not gauge invariant, there is a gauge arbitrariness in choosing their symmetry transformations. We have made particular choices to simplify the dis-

cussion of the effective Z_2 gauge theory; it is possible to make other gauge-equivalent choices, but this has no effect on the physics and does not lead to different possible effective theories. The transformations in Table 3.1 can be obtained from the definitions of the operations quoted for spin operators, by using the expressions that relate the U(1) and Z_2 gauge theory variables to spin operators and to one another.

With the symmetry transformations in hand, we can compute the action of symmetry on the spinon and vison excitations of the Z_2 spin liquid. Because these are fractional excitations, their behavior under symmetry is an instance of **symmetry fractionalization**.[39, 149, 150, 151] By computing the symmetry fractionalization of the spinons and visons, we characterize the Z_2 spin liquid as a symmetry enriched topological (SET) phase,[39, 149, 152, 153] which is a starting point for determining its universal properties tied to symmetry.

To characterize the spinon and vison symmetry fractionalization, we first specify the symmetry group in terms of generators and relations. We choose generators $\mathcal{I}$, $\mathcal{T}$, P_d, P_y, T_1 and T_2, where the $p6m$ generators are described graphically in Fig. 3.2a. The generators obey the relations

$$\mathcal{I}^2 = \mathcal{T}^2 = \mathcal{I}\mathcal{T}\mathcal{I}\mathcal{T} = 1 \tag{3.14}$$

$$\begin{aligned} (P_d)^2 &= (P_y)^2 = (P_d P_y)^6 \\ &= T_1 T_2 T_1^{-1} T_2^{-1} = T_1 P_y T_1^{-1} P_y = 1 \end{aligned} \tag{3.15}$$

$$T_2 = P_d T_1 P_d; T_2 P_y = P_y T_1 T_2^{-1}. \tag{3.16}$$

In addition, there are six more relations dictating that $\mathcal{T}$ and $\mathcal{I}$ commute with P_d, P_y and T_1 (it then follows from the other relations that the internal symmetries also commute with T_2). Taken together, these relations completely specify the group multiplication.

We introduce operators $\mathcal{I}^e$ and $\mathcal{I}^m$, and similarly for the other generators, giving the action of symmetry on spinons (e) and visons (m). These operators obey the same relations up to minus signs, and the pattern of minus signs for all the relations specifies the symmetry fractionalization of the corresponding excitation. The spinon and vison symmetry fractionalizations are computed in Appendix 3.7. For the visons, we find that all the relations hold with positive signs; that is,

the vison has trivial symmetry fractionalization. On the other hand, the spinon has non-trivial symmetry fractionalization; we find

$$\mathcal{I}^e P_y^e = -P_y^e \mathcal{I}^e, \tag{3.17}$$

while all other relations hold with a positive sign. This means that, acting on spinons, the Ising symmetry anticommutes with space group operations that exchange the A and B sublattices, but commutes with operations not exchanging the sublattices.

There have been many studies of Z_2 spin liquids on the kagome lattice with continuous spin symmetry, either U(1) spin rotations about the z-axis, or full SU(2) symmetry. It is interesting to ask whether the QKI Z_2 spin liquid is related to any of these states. In fact, it is impossible to start with such a state, and obtain the QKI Z_2 spin liquid by weak explicit breaking of the continuous spin symmetry down to Z_2^I. This is so because with continuous spin symmetry, the $\mathcal{I}$ operation can be continuously deformed to the identity, so that $\mathcal{I}^e$ must commute with all the discrete symmetry generators, which is not consistent with Eq. (3.17).

3.4 Vison zero modes at disclinations

Here, we consider disclination defects of the crystal lattice, and show that the Z_2 QSL has symmetry-protected zero modes bound to these defects. These zero modes are visons that cost exactly zero energy as long as Ising symmetry is preserved. We describe observable signatures of the vison zero modes that can be probed in future quantum Monte Carlo studies. We note that very similar anyon zero modes at symmetry-flux defects of on-site symmetries, and also at lattice dislocations, have been described previously in Ref. [154].

Figure 3.4 shows a π disclination centered at a hexagon. The disclination is a defect of the lattice where points related by a π rotation at the disclination center are identified. Apart from identifying points related by the π rotation, we focus on a special type of disclination where the Hamiltonian density away from the disclination center is left unchanged, **i.e.** the Hamiltonian of the XYZh model on every site and link is the same as in the defect-free system. Such a disclination

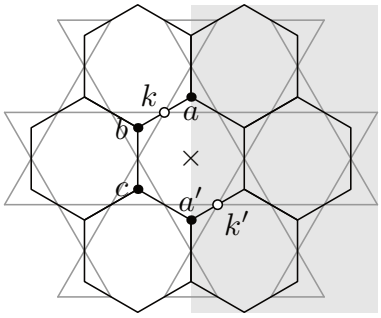

Figure 3.4: π disclination at a hexagon center of the kagome lattice, with the dual honeycomb lattice also shown. The disclination is a defect where the shaded region is cut out, and sites of the remaining lattice that are related by a π rotation about the disclination center are identified. Equivalently, rather than cut out the shaded region, we can simply identify all sites related by a π rotation, such as the kagome sites k and k'. Similarly, the honeycomb site a is identified with a'. The hexagonal honeycomb plaquette at the disclination center becomes a triangular plaquette with sides ab, bc, $ca' \simeq ca$.

preserves the Ising symmetry. All of our results continue to hold for more generic π disclinations, as long as Ising symmetry is preserved, and as long as the Hamiltonian density is unchanged in the far field of the defect. Our results also hold for any disclination that identifies sites in the A sublattice with sites in the B sublattice (**i.e.**, for $\pm\pi/3$ disclinations), but not for $\pm 2\pi/3$ disclinations that preserve the bipartite structure of the honeycomb lattice.

We first consider the effect of a single disclination in an infinite plane, using the effective Z_2 gauge theory of the Z_2 QSL. We go to the exactly solvable point of $\mathcal{H}_{\text{eff}}$ deep within the spin liquid phase, by setting $J = v = 0$.[3] At this point, the exact eigenstates are labeled by eigenvalues of the commuting operators τ^x_{r} and B_p, and the spinon and vison excitations do not propagate. We observe that all hexagonal plaquettes remain locally unchanged, except for the hexagon p_{dis} at the disclination center, which becomes a closed loop of **three** links. This implies that $B_{p_{dis}}$ is odd under the Ising symmetry, and in order to preserve Ising symmetry we must set the coupling K_{dis} of this term to zero. Therefore, putting a vison at the core of the disclination costs zero energy, and we have a pair of degenerate vison / no-vison states.

Remarkably, this vison zero mode is protected by the Z_2^I Ising symmetry; this is unusual because normally a unitary Z_2 symmetry cannot lead to symmetry-protected degeneracies. To see the symmetry protection, consider an effective 2×2 matrix Hamiltonian for the doublet of vison / no-vison states, $H_{\text{doublet}} = a_x\sigma^x + a_y\sigma^y + a_z\sigma^z$. a_z corresponds to K_{dis} and is forbidden by Ising symmetry. The off diagonal terms a_x and a_y are also forbidden, because no local operator we might use to perturb the Hamiltonian can create or destroy a vison and flip between σ^z eigenstates. The doublet therefore remains degenerate as long as Ising symmetry is preserved – no other symmetries are needed for its protection. While lattice rotation of the defect-free system plays an important role, allowing us to introduce the disclination in the first place, it and other point group symmetries are not needed to protect the zero mode.

We now turn to observable signatures of the vison zero modes. The degeneracy will be lifted

[3] At this point, the gauge theory is equivalent to the exactly solvable point of the toric code model on the honeycomb lattice. See Ref. [115] and Appendix 3.7.

if the Ising symmetry is broken explicitly, because $K_{dis} \neq 0$ is then allowed. Returning to the XYZh model, this can be achieved by adding a local transverse field

$$H_{\text{transverse}} = -\sum_{\boldsymbol{r}} h_x(\boldsymbol{r}) S^x_{\boldsymbol{r}}, \tag{3.18}$$

where $h_x(\boldsymbol{r})$ non-zero only near the disclination center. This implies that disclinations contribute a Curie term in the temperature dependence of the transverse spin susceptibility $\chi_{xx}(T)$. Since only the spins near the defect contribute to the Curie susceptibility, to detect this effect it is sufficient to look at the local susceptibility of spins in some region near the disclination. Indeed, looking at the local susceptibility is preferable to better separate bulk and impurity contributions to $\chi_{xx}(T)$; away from the disclination, $\chi_{xx}(T)$ goes to a constant as $T \to 0$. The Curie behavior should be observable within a temperature range $T_{\text{low}} < T < T_{\text{gap}}$, where T_{gap} is the lowest bulk energy gap of the XYZh model in temperature units, and T_{low} corresponds to the energy scale for interactions between vison zero modes on nearby disclinations. Such interactions require visons to tunnel through the bulk where they are gapped, and thus go to zero exponentially in the separation between disclinations.

The vison zero modes also have an interesting manifestation in entropy as measured by heat capacity. We consider a finite system without boundary, which has an even number N_{dis} of disclinations. Naïvely we might guess the total degeneracy is $2^{N_{dis}}$, but this is not correct due to the constraint that the total number of visons in the system must be even. This means that the total degeneracy is in fact $2^{N_{dis}-1}$. In principle, this should be observable in quantum Monte Carlo by measuring the heat capacity in a small transverse field, and integrating the resulting Schottky peak to obtain the entropy of $(N_{dis} - 1) \ln 2$ associated with the gapless defect modes.

This latter signature is important, as it differentiates vison zero modes from a collection of local doublets bound to disclinations (**e.g.** Kramers doublets), which would have a degeneracy of $2^{N_{dis}}$. Another way to differentiate these two scenarios would be to add perturbations, localized near disclinations, breaking all symmetries except Z_2^I.[4] Adding such perturbations will gap out local doublets (which cannot be protected by Ising symmetry alone), but will preserve the vison

[4] Unfortunately, it appears impossible to break Z_2^T while preserving Z_2^I, without introducing a Monte Carlo sign problem.

zero modes. We note that the presence of local doublets can also be interesting. For example, following Ref. [155], it can be shown that Kramers doublets bound to disclinations are a sign of a non-trivial symmetry protected topological phase, protected by the combination of D_6 point group and time reversal symmetry.[156]

The vison zero modes should be thought of as a consequence of the symmetry fractionalization of spinons and visons, and in particular of the non-trivial spinon symmetry fractionalization. We make this connection indirectly: Any Z_2 QSL in the same phase as the one described here can be adiabatically continued so that it is described by the same effective theory and has robust vison zero modes at disclinations, which are a property of the quantum phase. This Z_2 QSL is characterized as a SET phase by the spinon and vison symmetry fractionalization, and only the spinon symmetry fractionalization is non-trivial, so by process of elimination it must be responsible for the vison zero modes. For example, if we modified the action of Ising symmetry to be trivial on σ^x and σ^z, we would obtain trivial symmetry fractionalization, and nothing would forbid $K_{dis} \neq 0$, so there would be no vison zero modes. This argument is indirect, and it would certainly be desirable to have a more direct and explicit connection between symmetry fractionalization and vison zero modes, as obtained in Ref. [154] for on-site and translation symmetries. We have not currently made such a connection, which we leave for future work.

3.5 Other properties of the Z_2 spin liquid

Here we use our effective theory to discuss other properties of the Z_2 QSL. Some of these properties are likely challenging to test in quantum Monte Carlo, but may instead be accessible to other numerical approaches.

First, we focus on direct consequences of the non-trivial spinon symmetry fractionalization within the spin liquid phase. Every state in the single-spinon spectrum is at least doubly degenerate, because a non-degenerate state is not consistent with anticommuting symmetry generators as in Eq. (3.17). While the single-spinon spectrum cannot be directly probed, its degeneracies lead to characteristic features in the two-spinon continuum. Previous works elucidated this structure in

cases where translations have non-trivial commutation with other symmetry generators, and found an enhanced periodicity of the two-spinon density of states in crystal momentum.[157, 158, 159] Here, acting on a single spinon, translations commute with other generators. Nonetheless, similar structure is present in the density of states, and can be resolved by point group and Ising quantum numbers.

For simplicity, we focus on P_y and $\mathcal{I}$ symmetries, and follow the analysis of Ref. [159]. We consider a two-spinon scattering state $|\psi\rangle$, whose energy is such that single spinon excitations cannot decay (this will always be true near the bottom of the two-spinon continuum). Without loss of generality, we take $|\psi\rangle$ to be an eigenstate of P_y and $\mathcal{I}$, with eigenvalues $\sigma_P = \pm 1$ and $\sigma_{\mathcal{I}} = \pm 1$, respectively. The action of symmetry operations on $|\psi\rangle$ factorizes into a product of actions on the two individual spinons, for example

$$P_y|\psi\rangle = P_y^e(1)P_y^e(2)|\psi\rangle. \tag{3.19}$$

We then consider the effect on σ_P of transforming just one of the spinons by the Ising operation,

$$|\psi'\rangle = \mathcal{I}^e(1)|\psi\rangle. \tag{3.20}$$

We have

$$P_y|\psi'\rangle = P_y^e(1)P_y^e(2)|\psi'\rangle = -\sigma_P|\psi'\rangle, \tag{3.21}$$

and we see that $\sigma_P \to -\sigma_P$. Now, $|\psi'\rangle$ is an eigenstate with the same energy as $|\psi\rangle$, because $\mathcal{I}^e(1)$ is a symmetry operation, and the two spinons do not interact in a scattering state. Similarly, we can find a state of the same energy with $\sigma_{\mathcal{I}} \to -\sigma_{\mathcal{I}}$.

This discussion can be summarized by defining $\mathcal{N}_{\sigma_P,\sigma_{\mathcal{I}}}(\omega)$ to be the density of two-spinon scattering states with P_y-eigenvalue σ_P and $\mathcal{I}$-eigenvalue $\sigma_{\mathcal{I}}$. We have shown that $\mathcal{N}_{\sigma_P,\sigma_{\mathcal{I}}}(\omega)$ is independent of σ_P and $\sigma_{\mathcal{I}}$. In particular, the low-energy threshold for the two-spinon continuum is the same in all four symmetry sectors.

Another signature of the spinon symmetry fractionalization involves reduction to a one-dimensional SPT state.[160, 161] We roll the system into a cylinder, so that P_y acts effectively

as an on-site symmetry of the one-dimensional system, **i.e.** it does not exchange two ends of the cylinder. Then $\mathcal{I}$ and P_y generate a $Z_2 \times Z_2$ on-site symmetry, which can protect a single non-trivial SPT phase, the Haldane phase.[162, 163, 30, 31, 32, 33, 34, 35] In this phase, there are degenerate end states acting on which $\mathcal{I}$ and P_y anticommute, just as in Eq. (3.17). We consider two different minimally entangled states (MES) of the Z_2 spin liquid, that are related by creating a pair of spinons and dragging them to opposite ends of the cylinder. Equivalently, we can start with one MES and act on it with the string operator transporting a spinon along the cylinder. One of these MES will be in the trivial $Z_2 \times Z_2$ SPT phase, while the other will be in the Haldane phase, and the difference can be detected via the entanglement spectrum.[31]

Now we turn to the properties of continuous quantum phase transitions that may occur between the Z_2 QSL and nearby conventional ordered phases. To access such a transition, we can either condense spinons or visons. The particle that does not condense is gapped at the transition and plays no role there.

To study condensation of visons, we integrate out gapped spinon degrees of freedom, which reduces $\mathcal{H}_{\text{eff}}$ to a pure Z_2 gauge theory obtained from Eq. (3.12) by dropping the u and J terms, and replacing the gauge constraint with $\prod_{\mathsf{r}' \sim \mathsf{r}} \sigma^x_{\mathsf{r}\mathsf{r}'} = -1$. Condensation of visons in this theory, which is sometimes referred to as "odd" Z_2 gauge theory, has been studied before in [[164, 165]]. The simplest possibility, which is driven by nearest-neighbor hopping of visons on the triangular dual of the honeycomb lattice, is for visons to condense at the Brillouin zone corners (K points), which can lead either to columnar or plaquette valence bond solid (VBS) order, depending on the sign of an anisotropy term. The transition is in the XY universality class, where the physical VBS order parameter is bilinear in the XY field. Ref. [165] also studied transitions to other types of VBS states that can be driven by adding additional terms to the gauge theory.

In the present context, VBS order is likely for small J_a due to the mapping to the honeycomb lattice quantum dimer model (see Fig. 3.1). If this order can be found in quantum Monte Carlo, depending on the type of VBS order, there could be a continuous transition between the VBS and Z_2 QSL states.

Turning to condensation of spinons, the first step is to integrate out the gapped vison degrees of freedom. Before doing that, it is convenient to make a new gauge choice for the action of Ising symmetry, where

$$\mathcal{I} : \sigma^z_{\mathsf{rr}'} \rightarrow \sigma^z_{\mathsf{rr}'} \tag{3.22}$$

$$\mathcal{I} : \tau^z_{\mathsf{r}} \rightarrow -\tau^z_{\mathsf{r}}, \qquad \mathsf{r} \in \mathrm{A} \tag{3.23}$$

$$\mathcal{I} : \tau^z_{\mathsf{r}} \rightarrow \tau^z_{\mathsf{r}}, \qquad \mathsf{r} \in \mathrm{B}. \tag{3.24}$$

The difference from the form given in Table 3.1 is that we have "moved" (by gauge transformation) the action of $\mathcal{I}$ from the gauge field to the matter fields. Integrating out visons corresponds to freezing the magnetic fluctuations of the gauge field, so we set $\sigma^z_{\mathsf{rr}'} = 1$, and drop the K and v terms in $\mathcal{H}_{\text{eff}}$. The new gauge choice for Ising symmetry makes this procedure manifestly compatible with the symmetries of the problem.

The effective theory thus becomes two decoupled transverse field Ising models, on the A and B triangular sublattices of the honeycomb lattice. For simplicity, we assume $J > 0$ so that these Ising models are ferromagnetic. The two Ising models will be coupled by other allowed terms not included in $\mathcal{H}_{\text{eff}}$, as is easily taken into account upon passing to a continuum field theory. We denote the continuum fields for the two Ising models by ϕ_A and ϕ_B. To construct a Lagrangian for ϕ_A and ϕ_B, we need to discuss the action of microscopic symmetries. Both fields change sign under global Z_2 gauge transformations. On the other hand, ϕ_A changes sign under Ising symmetry while ϕ_B is invariant. Some of the lattice symmetries (such as P_y) exchange A and B sublattices, and therefore take $\phi_A \leftrightarrow \phi_B$. Taking these symmetries into account, and working in $2+1$-dimensional Euclidean space time with coordinates $\mu = \tau, x, y$, the continuum Lagrangian is

$$\mathcal{L} = \frac{1}{2}\left[(\partial_\mu \phi_A)^2 + (\partial_\mu \phi_B)^2\right] + \frac{m}{2}(\phi_A^2 + \phi_B^2) \tag{3.25}$$

$$+ \lambda(\phi_A^2 + \phi_B^2)^2 + \lambda' \phi_A^2 \phi_B^2. \tag{3.26}$$

Here we have included all quadratic terms with two or fewer derivatives, and all quartic terms with no derivatives.

For $\lambda' = -2\lambda$, $\mathcal{L}$ reduces to two decoupled ϕ^4 field theories, which are constrained by symmetry to have the same parameters. One can contemplate an Ising $\times$ Ising transition, but the $\phi_A^2\phi_B^2$ coupling is relevant at this fixed point, so the Ising $\times$ Ising transition can only exist as a multicritical point.

Setting instead $\lambda' = 0$, we have a XY model. The λ' term is a four-fold anisotropy that is known to be irrelevant at the XY critical point (see [[166]] and references therein). This suggests that there can be a continuous transition in the XY universality class between the Z_2 QSL, where $\langle\phi_A\rangle = \langle\phi_B\rangle = 0$, and an ordered state with a ϕ_A, ϕ_B condensate. To establish this conclusively, it would be necessary to consider allowed higher derivative terms and show they are irrelevant.

The nature of the ordered state depends on the sign of λ'. For $\lambda' > 0$, the condensate can take on four values, namely

$$\langle\phi_A\rangle = \pm\phi_0 \quad , \quad \langle\phi_B\rangle = 0 \tag{3.27}$$

$$\langle\phi_A\rangle = 0 \quad , \quad \langle\phi_B\rangle = \pm\phi_0. \tag{3.28}$$

The overall sign of the condensate is not physical, because it can be changed by a global Z_2 gauge transformation, so there are two distinct ground states. In this phase, Ising symmetry is preserved, but those point group symmetries exchanging the A and B sublattices are broken. A microscopic realization of this ordering pattern is a density wave of $S^+_{\boldsymbol{r}} S^+_{\boldsymbol{r}'}$ on nearest-neighbor kagome bonds, where $\langle S^+_{\boldsymbol{r}} S^+_{\boldsymbol{r}'}\rangle = c \pm \delta$, with the positive (negative) sign on bonds contained in up-pointing (down-pointing) triangles.

For $\lambda' < 0$, up to Z_2 gauge transformations there are two distinct states, with

$$\langle\phi_A\rangle = \pm\langle\phi_B\rangle. \tag{3.29}$$

Here, Ising symmetry is broken, and all lattice symmetries are preserved, so this is the same ferromagnetic state observed by CHM in the XYZh model.[50] There, a first-order transition was found between the QKI regime and the ferromagnetic state. Our analysis suggests that this transition could potentially be made continuous, and in the XY universality class, by some suitable modification of the XYZh model.

3.6 Discussion

In this paper, we derived an effective Z_2 gauge theory to explore the hypothesis that the QKI state observed in the XYZh model is a Z_2 QSL.[50] In addition to other properties, we found that lattice disclination defects in the Z_2 QSL host vison zero modes, which lead to striking observable signatures in the spin susceptibility and entropy. It would be exciting if these predictions can be tested in future numerical studies of the XYZh model.

The possibility of anyon zero modes at symmetry defects, including flux defects of on-site symmetries and lattice dislocations, has already been pointed out in Ref. [154]. However, it appears that little attention has been given to such phenomena so far. In part because anyon zero modes can give rise to striking observable consequences, as we discussed here, further work on this topic may be worthwhile.

3.7 Computation of spinon and vison symmetry fractionalization

In the main text, symmetry fractionalization was described in terms of operators giving the action of symmetry on a single spinon or vison. For exactly solvable toric code type models, such operators can be explicitly constructed, and used to compute the symmetry fractionalization of spinons and visons.[167] Here, using the fact that the QKI Z_2 spin liquid has a solvable point that is equivalent to a toric code model, we compute the symmetry fractionalization, largely following Ref. [167].

The Z_2 gauge theory $\mathcal{H}_{\text{eff}}$ of Eq. (3.12) is exactly solvable when $J = v = 0$, because B_p and τ^x_{r} commute with $\mathcal{H}_{\text{eff}}$ and form a complete set of commuting operators. To make contact with Ref. [167], we now exploit the well-known mapping between Z_2 gauge theories and toric code models,[115] which maps the solvable point of the gauge theory to a solvable toric code.

The toric code Hilbert space has a single Ising spin on each link of the honeycomb lattice, for which we write Pauli operators $\mu^z_{\mathsf{r}\mathsf{r}'}$, $\mu^x_{\mathsf{r}\mathsf{r}'}$. The Hilbert space is a tensor product of single-spin Hilbert spaces; there are no gauge constraints. The mapping between gauge theory and toric code

Hilbert spaces is given by

$$\mu^z_{\mathsf{rr}'} = \tau^z_{\mathsf{r}}\sigma^z_{\mathsf{rr}'}\tau^z_{\mathsf{r}'} \tag{3.30}$$

$$\mu^x_{\mathsf{rr}'} = \sigma^x_{\mathsf{rr}'}. \tag{3.31}$$

It follows that

$$\tau^x_{\mathsf{r}} = -\prod_{\mathsf{r}'\sim\mathsf{r}} \mu^x_{\mathsf{rr}'}, \tag{3.32}$$

where we used the gauge constraint Eq. (3.13). From these mappings and TABLE. 3.1, it is straightforward to determine the action of symmetry on $\mu^z_{\mathsf{rr}'}$ and $\mu^x_{\mathsf{rr}'}$. We have

$$g : \mu^{x,z}_{\mathsf{rr}'} \rightarrow \mu^{x,z}_{g(\mathsf{r}),g(\mathsf{r}')} \tag{3.33}$$

$$\mathcal{T} : \mu^{x,z}_{\mathsf{rr}'} \rightarrow \mu^{x,z}_{\mathsf{rr}'} \tag{3.34}$$

$$\mathcal{I} : \mu^{z}_{\mathsf{rr}'} \rightarrow -\mu^{z}_{\mathsf{rr}'} \tag{3.35}$$

$$\mathcal{I} : \mu^{x}_{\mathsf{rr}'} \rightarrow \mu^{x}_{\mathsf{rr}'}, \tag{3.36}$$

where g is a $p6m$ space group operation.

The gauge theory Hamiltonian $\mathcal{H}_{\text{eff}}$ maps to the toric code Hamiltonian

$$\tilde{\mathcal{H}}_{\text{toric}} = u\sum_{\mathsf{r}} A_{\mathsf{r}} - K\sum_{p} B_p, \tag{3.37}$$

where $A_{\mathsf{r}} \equiv \prod_{\mathsf{r}'\sim\mathsf{r}} \mu^x_{\mathsf{rr}'}$ and $B_p = \prod_{\mathsf{rr}'\in p} \mu^z_{\mathsf{rr}'}$. The only difference from the usual toric code on the honeycomb lattice is the sign of the A_{r} term. We can change this sign by making a basis change, using the unitary transformation $U = \prod_{\mathsf{rr}'} \mu^z_{\mathsf{rr}'}$, which sends $\mu^x \rightarrow -\mu^x$, and results in

$$\mathcal{H}_{\text{toric}} = -u\sum_{\mathsf{r}} A_{\mathsf{r}} - K\sum_{p} B_p. \tag{3.38}$$

The action of the symmetry operations on the Pauli operators remains unchanged in the new basis.

To summarize, we have mapped the problem to the usual toric code model on the honeycomb lattice. Space group and time reversal act in a trivial way on Pauli operators, but Ising symmetry acts non-trivially on μ^z. We can therefore anticipate that the subgroup $p6m \times Z_2^T$ has trivial symmetry fractionalization for both spinons and visons, and that any non-trivial part of the symmetry

fractionalization must involve the Ising symmetry. We now outline a more detailed calculation of the symmetry fractionalization, which confirms this expectation.

Before describing the calculation, we first give a more detailed description of what is meant by the spinon ("e-particle") symmetry fractionalization.[149] (The description for visons is identical.) The generators ($\mathcal{I}$, $\mathcal{T}$, P_d, P_y, T_1 and T_2) and relations of the symmetry group are described in Sec. 3.3. We introduce operators $\mathcal{I}^e$, $\mathcal{T}^e$, P_d^e, P_y^e, T_1^e and T_2^e giving the action of each generator on a single spinon. These operators obey the same relations as in the symmetry group, but only up to Z_2-valued phase factors. That is,

$$(\mathcal{I}^e)^2 = \sigma^e_{\mathcal{I}}, \qquad (\mathcal{T}^e)^2 = \sigma^e_{\mathcal{T}} \tag{3.39}$$

$$\mathcal{I}^e\mathcal{T}^e\mathcal{I}^e\mathcal{T}^e = \sigma^e_{\mathcal{I}\mathcal{T}} \tag{3.40}$$

$$(P_d^e)^2 = \sigma^e_{pd}, \qquad \left(P_y^e\right)^2 = \sigma^e_{py} \tag{3.41}$$

$$\left(P_d^e P_y^e\right)^6 = \sigma^e_{pdpy} \tag{3.42}$$

$$T_1^e T_2^e T_1^{e-1} T_2^{e-1} = \sigma^e_{t1t2} \tag{3.43}$$

$$T_1^e P_y^e T_1^{e-1} P_y^e = \sigma^e_{t1py} \tag{3.44}$$

$$T_1^e \mathcal{I}^e T_1^{e-1} \mathcal{I}^{e-1} = \sigma^e_{t1\mathcal{I}} \tag{3.45}$$

$$P_d^e \mathcal{I}^e P_d^{e-1} \mathcal{I}^{e-1} = \sigma^e_{pd\mathcal{I}} \tag{3.46}$$

$$P_y^e \mathcal{I}^e P_y^{e-1} \mathcal{I}^{e-1} = \sigma^e_{py\mathcal{I}} \tag{3.47}$$

$$T_1^e \mathcal{T}^e T_1^{e-1} \mathcal{T}^{e-1} = \sigma^e_{t1\mathcal{T}} \tag{3.48}$$

$$P_d^e \mathcal{T}^e P_d^{e-1} \mathcal{T}^{e-1} = \sigma^e_{pd\mathcal{T}} \tag{3.49}$$

$$P_y^e \mathcal{T}^e P_y^{e-1} \mathcal{T}^{e-1} = \sigma^e_{py\mathcal{T}} \tag{3.50}$$

$$T_2 = P_d T_1 P_d \tag{3.51}$$

$$T_2 P_y = P_y T_1 T_2^{-1}. \tag{3.52}$$

Here, each σ^e parameter can be either $+1$ or -1. The generators can be redefined by a minus sign without affecting any physical properties; for example, $T_1^e \to -T_e^1$ is an allowed redefinition. The σ^e parameters are invariant under such redefinitions, and specifying all 14 σ^e's gives the spinon

fractionalization class, which is an element of $H^2(G, Z_2) \simeq (Z_2)^{14}$. The last two relations have no σ^e parameters because the generators can be suitably redefined to remove any phase factors.

We find that all the σ^e's are unity, except $\sigma^e_{py\mathcal{I}} = -1$. Since P_y is the only $p6m$ generator that exchanges the A and B honeycomb sublattices, it follows that $\mathcal{I}^e$ anticommutes with precisely those $p6m$ operations exchanging the two sublattices, while it commutes with operations taking A to A and B to B. For the vison, we find that all the σ parameters are unity; that is, the vison fractionalization class is trivial.

We now describe how the spinon symmetry fractionalization is computed. We omit the computation of the vison symmetry fractionalization, as it can be straightforwardly obtained by the same means. We first follow Ref. [167] to obtain the σ^e's involving only unitary operations. We then determine the σ^e's involving time-reversal by a different argument.

In the ground state of the toric code, $A_{\mathsf{r}} = 1$, and spinons reside at honeycomb sites with $A_{\mathsf{r}} = -1$. To create a pair of spinons at r_1 and r_2, we act on the ground state with a string operator $\mathcal{L}^e_s$, where s is a path of links on the lattice joining r_1 and r_2, and $\mathcal{L}^e_s$ is a product of $\mu^z_{\mathsf{r}\mathsf{r}'}$ over this path. Such string operators also transport a spinon from one site to another. We consider two-spinon states

$$|\psi_e(s)\rangle = \mathcal{L}^e_s|\psi_0\rangle, \tag{3.53}$$

where for simplicity we assume the ground state $|\psi_0\rangle$ is invariant under all symmetry operations. The state $|\psi_e(s)\rangle$ only depends on the endpoints of the path s.

We let $\mathfrak{g}$ be a unitary element of the symmetry group, realized by the operator $U_{\mathfrak{g}}$. Ref. [167] showed that we can find operators $U^e_{\mathfrak{g}}(\mathsf{r})$ giving the action of $\mathfrak{g}$ on the spinon at r, satisfying

$$U_{\mathfrak{g}}|\psi_e(s)\rangle = U^e_{\mathfrak{g}}(\mathsf{r}_1)U^e_{\mathfrak{g}}(\mathsf{r}_2)|\psi_e(s)\rangle. \tag{3.54}$$

In general,

$$U^e_{\mathfrak{g}}(\mathsf{r}) = f_{\mathfrak{g}}(\mathsf{r})\mathcal{L}^e_{s_{\mathfrak{g}}(\mathsf{r})}, \tag{3.55}$$

where $f_{\mathfrak{g}}(\mathsf{r}) \in \{\pm 1\}$, and $s_{\mathfrak{g}}(\mathsf{r})$ is a path joining r to $\mathfrak{g}(\mathsf{r})$. Only the action of $U^e_{\mathfrak{g}}(\mathsf{r})$ on states of the form $|\psi_e(s)\rangle$ is of any consequence, and different choices of $U^e_{\mathfrak{g}}(\mathsf{r})$ having the same action are

considered equivalent. For the toric code model we are considering here, the choice of path $s_{\mathfrak{g}}(\mathsf{r})$ (for fixed endpoints) does not affect the action of $U^e_{\mathfrak{g}}(\mathsf{r})$ on $|\psi_e(s)\rangle$, so we can completely specify $U^e_{\mathfrak{g}}(\mathsf{r})$ by $f_{\mathfrak{g}}(\mathsf{r})$.

It was shown in Ref. [167] that the operators $U^e_{\mathfrak{g}}(\mathsf{r})$ have a unique action on states $|\psi_e(s)\rangle$ up to projective transformations $U^e_{\mathfrak{g}}(\mathsf{r}) \to \lambda(\mathfrak{g})U^e_{\mathfrak{g}}(\mathsf{r})$, where $\lambda(\mathfrak{g}) \in \{\pm 1\}$. Working in terms of generators and relations, these transformations simply express the freedom to redefine $U^e_{\mathfrak{g}}(\mathsf{r})$ by a minus sign for $\mathfrak{g}$ a generator.

The σ^e parameters can then be calculated by acting with appropriate products of $U^e_{\mathfrak{g}}(\mathsf{r})$ on a state $|\psi_e(s)\rangle$. For example, to calculate σ^e_{py}, we write

$$U^e_{P_y}[P_y(\mathsf{r}_1)]U^e_{P_y}(\mathsf{r}_1)|\psi_e(s)\rangle = \sigma^e_{py}|\psi_e(s)\rangle, \tag{3.56}$$

and evaluate the left-hand side.

As mentioned above, the operators $U^e_{\mathfrak{g}}(\mathsf{r})$ are completely specified by $f_{\mathfrak{g}}(\mathsf{r})$. It is not difficult to see that

$$f_g(\mathsf{r}) = 1, \tag{3.57}$$

for g any space group operation, including the generators T_1, T_2, P_y and P_d. For the Ising symmetry, we have

$$f_{\mathcal{I}}(\mathsf{r}) = \begin{cases} +1, & \mathsf{r} \in \mathrm{A} \\ -1, & \mathsf{r} \in \mathrm{B} \end{cases}. \tag{3.58}$$

With this information, it is straightforward to follow the prescription described above and determine all the σ^e parameters not involving time reversal. We find that they are all equal to unity except $\sigma^e_{py\mathcal{I}} = -1$.

It would not be difficult to extend the formalism of Ref. [167] to incorporate time reversal, but to maximize efficiency and minimize the introduction of new formalism, we use a different set of arguments to determine the remaining five σ^e parameters involving $\mathcal{T}$. All of these parameters are associated with particular symmetry-protected degeneracies in the single-spinon spectrum that we now show are not present.

First, we consider $\sigma^e_{\mathcal{T}}$. If this parameter were -1, spinons would be Kramers doublets, but a spinon localized on the lattice site r is clearly non-degenerate, implying $\sigma^e_{\mathcal{T}} = 1$. Similarly, we must also have $\sigma^e_{\mathcal{I}\mathcal{T}} = 1$, since otherwise $\mathcal{I}^e$ and $\mathcal{T}^e$ would anticommute, and a spinon localized to r would have at least a two-fold degeneracy.

The remaining σ^e parameters involving time reversal are $\sigma^e_{t1\mathcal{T}}$, $\sigma^e_{pd\mathcal{T}}$ and $\sigma^e_{py\mathcal{T}}$. These parameters involve the space group generators, which in general are not symmetries of a spinon localized at r. Instead, it is convenient to consider single-spinon plane wave states. We perturb the toric code Hamiltonian by adding $\delta H = -\tilde{h}\sum_{\mathsf{r}\mathsf{r}'} \mu^z_{\mathsf{r}\mathsf{r}'}$, which breaks Z_2^I but preserves $p6m \times Z_2^T$. This term is a nearest-neighbor hopping for spinons, and results in a spinon dispersion with a non-degenerate minimum at $\boldsymbol{k} = 0$. If any of $\sigma^e_{t1\mathcal{T}}$, $\sigma^e_{pd\mathcal{T}}$ or $\sigma^e_{py\mathcal{T}}$ were equal to -1, time reversal would anticommute with some space group operations, which is inconsistent with having a non-degenerate single-spinon energy eigenstate. Therefore, all of the σ^e parameters involving time reversal are equal to $+1$.

3.8 Conclusion and future work

The gauge theory description gives some hints to the physics of anisotropic exchange. However, it is certainly interesting to study the anisotropic exchange further since it is the simplest term to capture the spin-orbit coupling effect for the pseudo-spin model.

Furthermore, it will be interesting to combine numerical methods to search Z_2 topological order in the parameter space and find vison zero modes.

Chapter 4

High-energy electronic excitations in Sr_2IrO_4 observed by Raman scattering[1]

The two most relevant energy scale for strongly correlated electrons are the bandwidth t and the onsite U which capture the Coulomb interaction between electrons. The competition between the two energy scale leads to various interesting phenomena such as metal-insulator transition[168], superconductivity[169], Kondo effects[170] ... e.t.c. The 3d transition metal oxides are the ideal playground to study the correlated electrons and have been extensively studied for decades.

On the other hand, the discovery of topological insulator exhibits the non-trivial physics emerges from strong spin-orbit coupling (SOC). SOC is a relativistic effect which entangles the orbital and spin wave function. It scales as Z^4, where Z is the atomic number. SOC is usually considered as a small perturbation in 3d transition metal oxides. However, for heavy elements, the quantitative change in SOC could lead to striking qualitative effect.

The two research topics come together in the heavy transition metal compounds with 4d or 5d ions[52]. As the atomic number increases, the SOC coupling increases. On the other hand, because the orbital wave function is more and more extended, the Coulomb repulsion reduces as the atomic number increases. It turns out in 4d and 5d transition metal compounds, the three energy scale, bandwidth t, on-site U and the SOC λ are all relevant. Thus, in search of new phases of matter, heavy element compound such as iridates plays an important role.

The Sr_2IrO_4 is one of the materials that attracts much attention due to the unusual effect of

[1] This section has been published as a portion of Jhih-An Yang, Yi-Ping Huang, Michael Hermele, Tongfei Qi, Gang Cao, and Dmitry Reznik, Phys. Rev. B 91, 195140,[51] copyright 2015 American Physical Society, and is reproduced here in accord with the copyright policies of the American Physical Society.

SOC. The material is an insulator. According to DFT calculation, it is necessary to include SOC to open the band gap using reasonable parameters. Sr_2IrO_4 is thus considered as a SOC-induced insulator[78]. In addition to the non-trivial effect of SOC, Sr_2IrO_4 has a local electronic configuration that reminiscent the electronic configuration of cuprates which is the mother compound of the high-Tc superconductor[171]. The Raman experiment on this material will be useful for future experimental or theoretical studies.

In this project, the Raman spectroscopy found two peaks with distinct polarization signals which cannot be described by simple selection rules of magnon or phonon. We would like to understand what the observed Raman signal suggest about the electronic structure. We propose two possible excitations that could be responsible for the observed signal. Both of them are electronic excitation. One scenario corresponds to onsite d-d transitions between different crystal field levels and the other scenario corresponds to the inter-site electronic transition between an onsite wave function and a cluster state. From the observed selection rule, the onsite d-d transition should also contribute to polarization A_{2g} and B_{2g}. The fact that those component are not observed suggest the second scenario is a more nature explanation. However, from the symmetry analyze, we cannot rule out the possibility that the electronic transitions contribute to A_{2g} and B_{2g} polarization are not forbidden by symmetry but with a small cross-section. To finalize the answer, we need more experiments in the future. The theoretical ideas that are essential to derive the above physical picture will be explained in the following sections.

4.1 Experimental facts

From the data measured by Yang. The high-energy Raman peak is observed in $xx(A_{1g}+B_{1g})$, $x'x'(A_{1g}+B_{2g})$ and $x'y'(A_{2g}+B_{1g})$ channel. As shown in FIG. 4.1 The Raman peak is absent in $A_{2g}+B_{2g}$ channel. Looking at the data more carefully, the big Raman peak at xx is actually two different peak separated by $10meV$ with A_{1g} peak at 690 meV and B_{1g} peak at 680 meV. Here, the representation are the irreducible representation of D_{4h} point group.

This big Raman signal is also observed in cuprate[172]. The charge transfer gap in cuprate

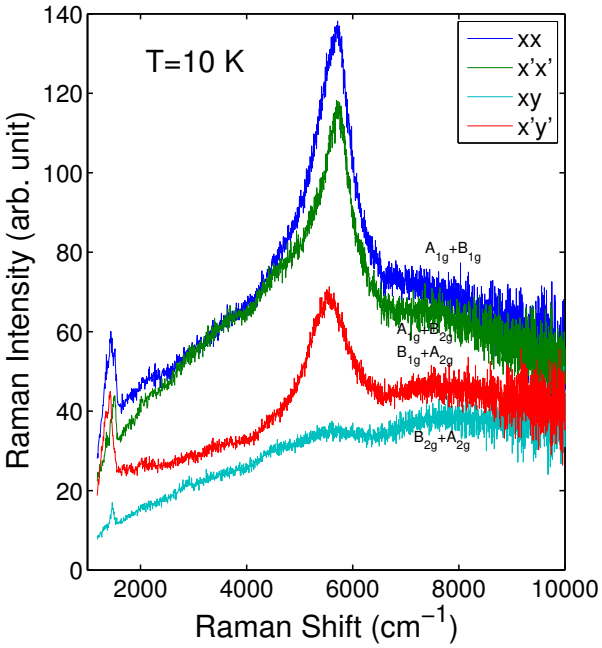

Figure 4.1: Raman spectra with incident laser wave-length 457.9 nm in four different scattering configurations measured at 10 K. Broad peaks around 5600 cm1 are electronic (see text) and peaks around 1400 cm1 are two-phonon scattering. xx probes $A_{1g} + B_{1g}$ symmetry, x'x'($A_{1g} + B_{2g}$), x'y'($B_{1g} + A_{2g}$), xy ($B_{2g} + A_{2g}$).

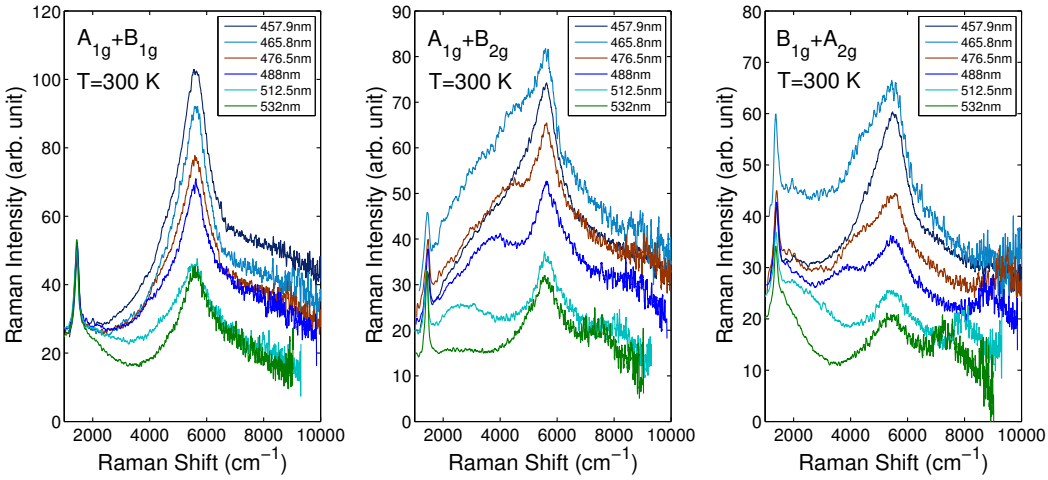

Figure 4.2: Raman spectra with different excitation energies in xx, x'x', and x'y' scattering configurations. The A_{1g} and B_{1g} peaks keep their positions at different laser energies, indicating that these peaks are real Raman signals. The spectra were normalized to the same power of incident lasers.

is $1.7 \sim 2eV$. The onsite U is about $5eV$. Since this big Raman peak is also observed in iridate, it is nature to ask in what aspects the cuprate and iridate are similar such that we can see this big Raman peak in both materials?

4.2 The crystal structure: space group and corresponding point group.

4.2.1 Space group of the material

There are several experiments about the determination of this material. However, we assume the essential structure for our modeling to be of the space group 142 and the corresponding point group to be D_{4h} [173]. The corresponding structure is shown in FIG. 4.2.1. There are three positions for oxygen ion. The ratio between O_1 and O_2 is 861:139.

However, the site symmetry which is the symmetry that leaves the site invariant will have lower symmetry than the corresponding point group, D_{4h}, of the space group. In this material, the bending of bond angle lowers the symmetry from D_{4h} to C_{4h}.

Here, we describe the symmetry elements explicitly. D_{4h} had C_{4z} and C_{2z} rotation along z-axis. C_{2x}, C_{2y} rotation along local x and y-axes. C_{2xy} and $C_{2x\bar{y}}$ rotation along local $(1,1,0)$ and $(1,-1,0)$ axis and inversion, I. The rest elements are the combination of the operation IC_{2x}, IC_{2xy}, IC_{2z}, $IC_{2z}C_{4z}$.

C_{4h} is the sub group of D_{4h} without group elements C_{2x}, C_{2y}, C_{2xy} and $C_{2x\bar{y}}$.

4.2.2 Crystalline electric field(CEF)

The iridium is surrounded by octahedral crystal field with D_{4h} distortion due to the elongation along c-axis. The distortion of CEF can be captured by three independent parameter B_4, B_2^0 and B_4^0[75].

$$H_{tetra} = \underbrace{B_4\left(O_4^0 + 5O_4^4\right)}_{cubic} + \underbrace{B_2^0 O_2^0 + B_4^0 O_4^0}_{tetragonal} + 48B_4 + 48B_4^0 + 3B_2^0, \tag{4.1}$$

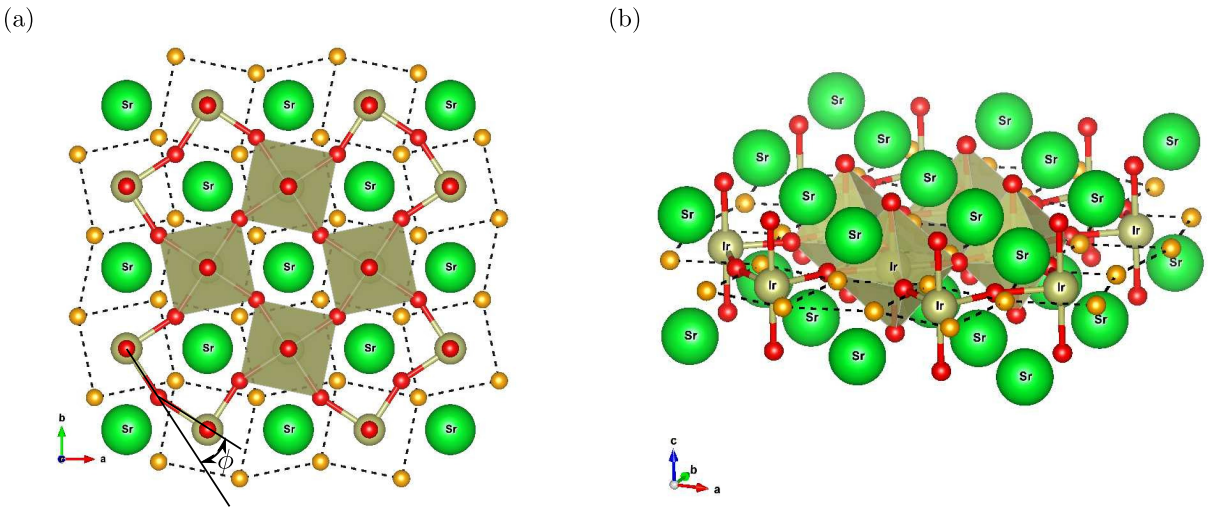

Figure 4.3: (a) Top view.(b) Side view. The red circle denote the most probable oxygen location. The orange oxygen is the defect of oxygen.

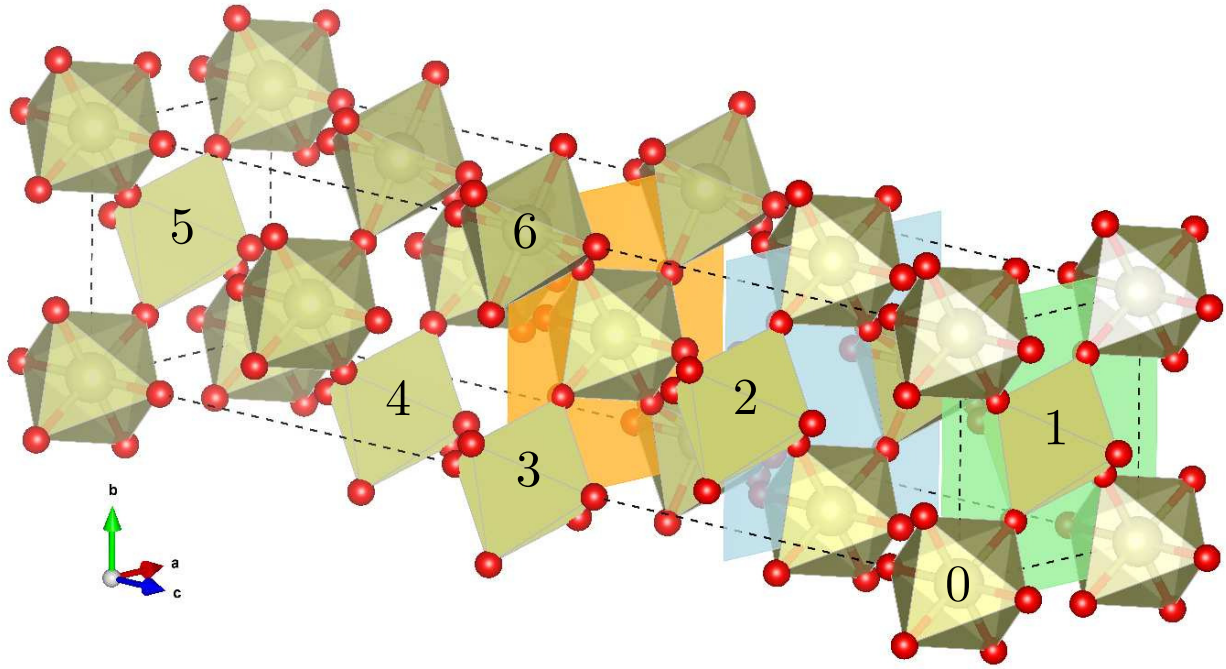

Figure 4.4: The space group structure. To show the structure explicitly, we label some sites. The site $1 \sim 5$ are related by four fold screw axis with $x = y = 0.5$. 0 to 1 is by glide a, 0 to 2 by glide c, 0 to 6 by glide d. Thus, the space group is $I4_1/acd$.

where the operators O are composed of orbital angular momentum operators

$$\begin{aligned} O_4^0 &= 35L_z^4 - 30L(L+1)L_z^2 + 25L_z^2 - 6L(L+1) + 3L^2(L+1)^2 \\ O_4^4 &= \frac{1}{2}\left(L_+^4 + L_-^4\right) \\ O_2^0 &= 3L_z^2 - L(L+1) \\ O_2^2 &= \frac{1}{2}\left(L_+^2 + L_-^2\right). \end{aligned} \tag{4.2}$$

The constant shift is just a redefinition of zero energy orbitals to be yz, zx. If we project the angular momentum operators into the d orbitals, and arrange our basis by $yz, zx, xy, 3z^2 - r^2, x^2 - y^2$, the angular momentum are represented by

$$L_x = \begin{pmatrix} 0 & 0 & 0 & -i\sqrt{3} & -i \\ 0 & 0 & i & 0 & 0 \\ 0 & -i & 0 & 0 & 0 \\ i\sqrt{3} & 0 & 0 & 0 & 0 \\ i & 0 & 0 & 0 & 0 \end{pmatrix},$$

$$L_y = \begin{pmatrix} 0 & 0 & -i & 0 & 0 \\ 0 & 0 & 0 & i\sqrt{3} & -i \\ i & 0 & 0 & 0 & 0 \\ 0 & -i\sqrt{3} & 0 & 0 & 0 \\ 0 & i & 0 & 0 & 0 \end{pmatrix},$$

$$L_z = \begin{pmatrix} 0 & i & 0 & 0 & 0 \\ -i & 0 & 0 & 0 & 0 \\ 0 & 0 & 0 & 0 & 2i \\ 0 & 0 & 0 & 0 & 0 \\ 0 & 0 & -2i & 0 & 0 \end{pmatrix}. \tag{4.3}$$

For future convenience, we redefine the parameters

$$\begin{aligned} \Delta &= 9B_2^0 + 60B_4^0 \\ \Delta' &= 12B_2^0 - 60B_4^0 \\ 120B_4 &= 10Dq, \end{aligned} \tag{4.4}$$

where B_4 control the E_g and T_{2g} energy splitting and Δ, Δ' are the parameters control the tetragonal distortion.

$$H_{tetra} = \begin{pmatrix} 0 & 0 & 0 & 0 & 0 \\ 0 & 0 & 0 & 0 & 0 \\ 0 & 0 & \Delta & 0 & 0 \\ 0 & 0 & 0 & \Delta - \Delta' + 120B_4 & 0 \\ 0 & 0 & 0 & 0 & \Delta + 120B_4 \end{pmatrix} \tag{4.5}$$

The relation between CEF and SOC are represented in Fig.4.5. According to experimental evidence

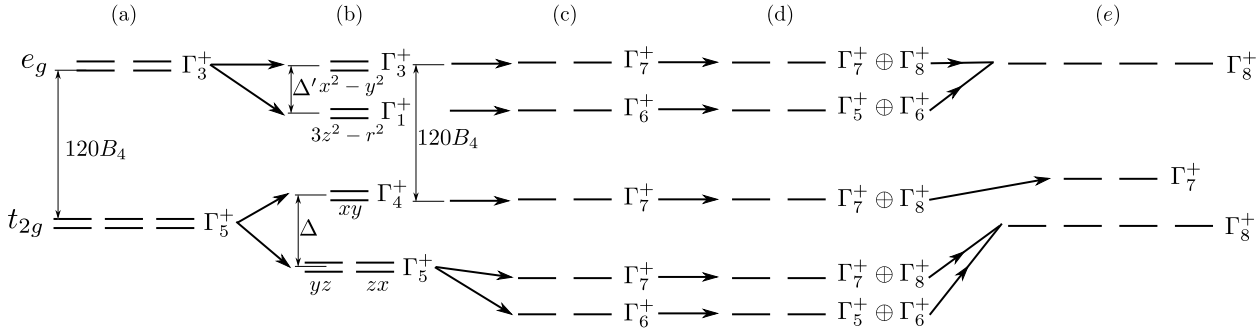

Figure 4.5: (a)Cubic(O_h) CEF.(b)Tetragonal distorted(D_{4h}) CEF. (c)Tetragonal distorted CEF(D_{4h})+SOC.(d)C_{4h} CEF+SOC (e) Cubic(O_h) CEF+ SOC

which suggest $\Delta \sim 0.075eV, \lambda \sim 0.4eV$ [174], $\Delta' \sim 2eV$ and $120B_4 \sim 4eV$[175]. For Ir^{4+} which had valence electron configuration $5d^5$, the filled state will be in Γ_7^+ for tetragonal distorted CEF and SOC are considered.

4.2.3 t_{2g} orbital splitting with spin-orbit coupling and tetragonal distortion(D_{4h}).

If we assume the e_g orbitals are completely decoupled with t_{2g} orbitals, we can diagonalize the spin-orbit coupling and tetragonal crystal field distortion analytically at the same time.

Within the t_{2g} Hilbert space, we can write down the tetragonally distorted crystal field as

$$H_{tetra} = \begin{pmatrix} 1 & 0 \\ 0 & 1 \end{pmatrix} \otimes \begin{pmatrix} 0 & 0 & 0 \\ 0 & 0 & 0 \\ 0 & 0 & \Delta \end{pmatrix} = \begin{pmatrix} 0 & 0 & 0 & 0 & 0 & 0 \\ 0 & 0 & 0 & 0 & 0 & 0 \\ 0 & 0 & \Delta & 0 & 0 & 0 \\ 0 & 0 & 0 & 0 & 0 & 0 \\ 0 & 0 & 0 & 0 & 0 & 0 \\ 0 & 0 & 0 & 0 & 0 & \Delta \end{pmatrix}. \tag{4.6}$$

Here, Δ represent the energy splitting between xy and yz, zx orbitals and should not be confused with the 10Dq splitting. The orbital basis of this representation is arranged as yz, zx, xy. The spin basis is arranged as $+, -$. In order to make our expression consistent with other notation, we change basis as

$$\begin{aligned} |\tilde{0}\rangle &= id_{xy} \\ |\pm\tilde{1}\rangle &= \frac{1}{\sqrt{2}}\left(\mp id_{yz} + d_{zx}\right). \end{aligned} \tag{4.7}$$

Under this basis, the fictitious angular momentum operator can be represented as

$$l_x = \begin{pmatrix} 0 & 0 & \frac{1}{\sqrt{2}} \\ 0 & 0 & \frac{1}{\sqrt{2}} \\ \frac{1}{\sqrt{2}} & \frac{1}{\sqrt{2}} & 0 \end{pmatrix}; l_y = \begin{pmatrix} 0 & 0 & -\frac{i}{\sqrt{2}} \\ 0 & 0 & \frac{i}{\sqrt{2}} \\ \frac{i}{\sqrt{2}} & -\frac{i}{\sqrt{2}} & 0 \end{pmatrix}; l_z = \begin{pmatrix} 1 & 0 & 0 \\ 0 & -1 & 0 \\ 0 & 0 & 0 \end{pmatrix}. \tag{4.8}$$

The spin-orbit interaction can thus be written as $H_{SOC} = \sum_i -\lambda s_i \otimes l_i$.

$$H_{SOC} = \begin{pmatrix} -\frac{\lambda}{2} & 0 & 0 & 0 & 0 & 0 \\ 0 & \frac{\lambda}{2} & 0 & 0 & 0 & -\frac{\lambda}{\sqrt{2}} \\ 0 & 0 & 0 & -\frac{\lambda}{\sqrt{2}} & 0 & 0 \\ 0 & 0 & -\frac{\lambda}{\sqrt{2}} & \frac{\lambda}{2} & 0 & 0 \\ 0 & 0 & 0 & 0 & -\frac{\lambda}{2} & 0 \\ 0 & -\frac{\lambda}{\sqrt{2}} & 0 & 0 & 0 & 0 \end{pmatrix} \tag{4.9}$$

The complete single particle Hamiltonian is

$$H = H_{SOC} + H_{tetra} = \begin{pmatrix} -\frac{\lambda}{2} & 0 & 0 & 0 & 0 & 0 \\ 0 & \frac{\lambda}{2} & 0 & 0 & 0 & -\frac{\lambda}{\sqrt{2}} \\ 0 & 0 & \Delta & -\frac{\lambda}{\sqrt{2}} & 0 & 0 \\ 0 & 0 & -\frac{\lambda}{\sqrt{2}} & \frac{\lambda}{2} & 0 & 0 \\ 0 & 0 & 0 & 0 & -\frac{\lambda}{2} & 0 \\ 0 & -\frac{\lambda}{\sqrt{2}} & 0 & 0 & 0 & \Delta \end{pmatrix}. \tag{4.10}$$

The full Hilbert space is arranged as $\tilde{1},+;-\tilde{1},+;\tilde{0},+;\tilde{1},-;-\tilde{1},-;\tilde{0},-$. Or

$$H = \begin{pmatrix} 0 & \frac{i\lambda}{2} & 0 & 0 & 0 & -\frac{\lambda}{2} \\ -\frac{1}{2}(i\lambda) & 0 & 0 & 0 & 0 & \frac{i\lambda}{2} \\ 0 & 0 & \Delta & \frac{\lambda}{2} & -\frac{1}{2}(i\lambda) & 0 \\ 0 & 0 & \frac{\lambda}{2} & 0 & -\frac{1}{2}(i\lambda) & 0 \\ 0 & 0 & \frac{i\lambda}{2} & \frac{i\lambda}{2} & 0 & 0 \\ -\frac{\lambda}{2} & -\frac{1}{2}(i\lambda) & 0 & 0 & 0 & \Delta \end{pmatrix}. \tag{4.11}$$

with basis choice $yz,+;zx,+;xy,+;yz,-;zx,-,xy,-$. The eigenvectors that diagonalize H can

be parameterized by $\frac{\Delta}{\lambda}$. Here we define some functions for our future convenience.

$$\begin{aligned} f(p) &= \sqrt{(1-2p)^2+8}-(1-2p) \\ sin\delta &= \frac{f(\frac{\Delta}{\lambda})}{\sqrt{f(\frac{\Delta}{\lambda})^2+8}} \\ cos\delta &= \frac{2\sqrt{2}}{\sqrt{f(\frac{\Delta}{\lambda})^2+8}} \end{aligned} \tag{4.12}$$

The eigenvectors can be written as

$$\begin{pmatrix} |A_{\Gamma_7^+,+}\rangle \\ |A_{\Gamma_7^+,-}\rangle \\ |B_{\Gamma_7^+,+}\rangle \\ |B_{\Gamma_7^+,-}\rangle \\ |C_{\Gamma_6^+,+}\rangle \\ |C_{\Gamma_6^+,-}\rangle \end{pmatrix}$$

$$= \begin{pmatrix} 0 & e^{i(a+a')}\cos(\delta) & 0 & 0 & 0 & -e^{i(a+a')}\sin(\delta) \\ 0 & 0 & e^{ia}\sin(\delta) & -e^{ia}\cos(\delta) & 0 & 0 \\ 0 & -ie^{i(b+b')}\sin(\delta) & 0 & 0 & 0 & -ie^{i(b+b')}\cos(\delta) \\ 0 & 0 & -ie^{ib}\cos(\delta) & -ie^{ib}\sin(\delta) & 0 & 0 \\ -ie^{i(c+c')} & 0 & 0 & 0 & 0 & 0 \\ 0 & 0 & 0 & 0 & -ie^{ic} & 0 \end{pmatrix} \begin{pmatrix} |+\tilde{1},+\rangle \\ |-\tilde{1},+\rangle \\ |\ \ \tilde{0},+\rangle \\ |+\tilde{1},-\rangle \\ |-\tilde{1},-\rangle \\ |\ \ \tilde{0},-\rangle \end{pmatrix}$$

$$= \begin{pmatrix} \frac{ie^{i(a+a')}\cos(\delta)}{\sqrt{2}} & \frac{e^{i(a+a')}\cos(\delta)}{\sqrt{2}} & 0 & 0 & 0 & -ie^{i(a+a')}\sin(\delta) \\ 0 & 0 & ie^{ia}\sin(\delta) & \frac{ie^{ia}\cos(\delta)}{\sqrt{2}} & -\frac{e^{ia}\cos(\delta)}{\sqrt{2}} & 0 \\ \frac{e^{i(b+b')}\sin(\delta)}{\sqrt{2}} & -\frac{ie^{i(b+b')}\sin(\delta)}{\sqrt{2}} & 0 & 0 & 0 & e^{i(b+b')}\cos(\delta) \\ 0 & 0 & e^{ib}\cos(\delta) & -\frac{e^{ib}\sin(\delta)}{\sqrt{2}} & -\frac{ie^{ib}\sin(\delta)}{\sqrt{2}} & 0 \\ -\frac{e^{i(c+c')}}{\sqrt{2}} & -\frac{ie^{i(c+c')}}{\sqrt{2}} & 0 & 0 & 0 & 0 \\ 0 & 0 & 0 & \frac{e^{ic}}{\sqrt{2}} & -\frac{ie^{ic}}{\sqrt{2}} & 0 \end{pmatrix} \begin{pmatrix} |yz,+\rangle \\ |zx,+\rangle \\ |xy,+\rangle \\ |yz,-\rangle \\ |zx,-\rangle \\ |xy,-\rangle \end{pmatrix} \tag{4.13}$$

D_{4h}	E	C_{4z}	C_{2z}	C_{2x}	C_{2xy}	I	$\mathcal{T}$
Γ_1^+	1	1	1	1	1	1	1
Γ_3^+	1	-1	1	1	-1	1	-1
Γ_6^+	$\begin{pmatrix} 1 & 0 \\ 0 & 1 \end{pmatrix}$	$\begin{pmatrix} w & 0 \\ 0 & w^* \end{pmatrix}$	$\begin{pmatrix} i & 0 \\ 0 & -i \end{pmatrix}$	$\begin{pmatrix} 0 & -i \\ -i & 0 \end{pmatrix}$	$\begin{pmatrix} 0 & w \\ -w^* & 0 \end{pmatrix}$	$\begin{pmatrix} 1 & 0 \\ 0 & 1 \end{pmatrix}$	$\begin{pmatrix} 0 & -1 \\ 1 & 0 \end{pmatrix}$
Γ_7^+	$\begin{pmatrix} 1 & 0 \\ 0 & 1 \end{pmatrix}$	$\begin{pmatrix} -w & 0 \\ 0 & -w^* \end{pmatrix}$	$\begin{pmatrix} i & 0 \\ 0 & -i \end{pmatrix}$	$\begin{pmatrix} 0 & -i \\ -i & 0 \end{pmatrix}$	$\begin{pmatrix} 0 & -w \\ w^* & 0 \end{pmatrix}$	$\begin{pmatrix} 1 & 0 \\ 0 & 1 \end{pmatrix}$	$\begin{pmatrix} 0 & -1 \\ 1 & 0 \end{pmatrix}$
Γ_5^-	$\begin{pmatrix} 1 & 0 \\ 0 & 1 \end{pmatrix}$	$\begin{pmatrix} i & 0 \\ 0 & -i \end{pmatrix}$	$\begin{pmatrix} -1 & 0 \\ 0 & -1 \end{pmatrix}$	$\begin{pmatrix} 0 & i \\ -i & 0 \end{pmatrix}$	$\begin{pmatrix} 0 & -1 \\ -1 & 0 \end{pmatrix}$	$\begin{pmatrix} -1 & 0 \\ 0 & -1 \end{pmatrix}$	$\begin{pmatrix} 0 & 1 \\ 1 & 0 \end{pmatrix}$
Γ_6^-	$\begin{pmatrix} 1 & 0 \\ 0 & 1 \end{pmatrix}$	$\begin{pmatrix} w^* & 0 \\ 0 & w \end{pmatrix}$	$\begin{pmatrix} -i & 0 \\ 0 & i \end{pmatrix}$	$\begin{pmatrix} 0 & 1 \\ -1 & 0 \end{pmatrix}$	$\begin{pmatrix} 0 & w \\ -w^* & 0 \end{pmatrix}$	$\begin{pmatrix} -1 & 0 \\ 0 & -1 \end{pmatrix}$	$\begin{pmatrix} 0 & -1 \\ 1 & 0 \end{pmatrix}$
Γ_7^-	$\begin{pmatrix} 1 & 0 \\ 0 & 1 \end{pmatrix}$	$\begin{pmatrix} -w^* & 0 \\ 0 & -w \end{pmatrix}$	$\begin{pmatrix} -i & 0 \\ 0 & i \end{pmatrix}$	$\begin{pmatrix} 0 & -1 \\ 1 & 0 \end{pmatrix}$	$\begin{pmatrix} 0 & w \\ -w^* & 0 \end{pmatrix}$	$\begin{pmatrix} -1 & 0 \\ 0 & -1 \end{pmatrix}$	$\begin{pmatrix} 0 & -1 \\ 1 & 0 \end{pmatrix}$

Table 4.1: The double group representation for D_{4h} point group. $w = \frac{1+i}{\sqrt{2}}$

with eigenenergies

$$\begin{aligned} E_A &= \frac{1}{4}\left(2\Delta + \lambda + \sqrt{(2\Delta-\lambda)^2 + 8\lambda^2}\right) \\ E_B &= \frac{1}{4}\left(2\Delta + \lambda - \sqrt{(2\Delta-\lambda)^2 + 8\lambda^2}\right) \\ E_C &= -\frac{\lambda}{2}. \end{aligned} \tag{4.14}$$

Here, we use A,B,C to represent different doublets. For Ir^{4+}, we focus on A doublets.

If Γ_6^+ had the energy between the two Γ_7^+, we require $(E_C - E_A)(E_C - E_B) < 0$. After some algebra, that corresponds to the constraint $\Delta\lambda < 0$.

Here, the phase factors, a, a', b, b', c, c'(prime are the relative phase factors),are defined such that time-reversal operator can be written as $\mathcal{T} = -i\sigma^2 K$. The time-reversal operator is represented as

$$\begin{pmatrix} 0 & e^{-i(2b+b')} \\ -e^{-i(2b+b')} & 0 \end{pmatrix}. \tag{4.15}$$

We choose $a = 0$,$b = c = \frac{\pi}{2}$, $a' = \pi$, $b' = c' = 0$ as our phase choice.

Under the phase convention, the relevant representation of D_{4h} can be constructed(Table 4.1).

Note that, the subscript Γ_6^+ and Γ_7^+ labeled how the states transform under symmetry. The reason we emphasize this is because the confusion when we truncated the e_g orbitals. When only t_{2g} orbitals are considered, the matrix element of REAL angular momentum operator just looks like the $l = 1$ angular momentum operator with an additional minus sign, $\boldsymbol{L}_{t_{2g}} = -\boldsymbol{L}_{l=1}$. That helps

us to label the spin-orbital wave function by j_{eff}. However, this labeling is sometimes confusing.

The real wave function transform according to $|t_{2g}\rangle \otimes |s = \frac{1}{2}\rangle \equiv -|l = 1\rangle \otimes |s = \frac{1}{2}\rangle$. In most literature, they use $|j_{eff}\rangle = |l = 1\rangle \otimes |s = \frac{1}{2}\rangle = |j_{eff} = \frac{3}{2}\rangle \oplus |j_{eff} = \frac{1}{2}\rangle$ to label the states. However, the minus sign is important when considering the representation. We should keep in mind that the symmetry operation representation constructed by the j_{eff} had a minus sign difference with how the state really transform. For example, the real C_4 rotation should be constructed as $-\langle j_{eff}|exp\left[i\theta j_{eff}\right]|j_{eff}\rangle$ instead of $\langle j_{eff}|exp\left[i\theta j_{eff}\right]|j_{eff}\rangle$. Thus, in the j_{eff} notation, $|j_{eff} = \frac{1}{2}, \pm\frac{1}{2}\rangle$ and $|j_{eff} = \frac{3}{2}, \pm\frac{1}{2}\rangle$ actually did not transform according to real spin. Instead, it is $|j_{eff} = \frac{3}{2}, \pm\frac{3}{2}\rangle$ transform as real spin. (Note that in the definition we have the minus sign. However, the definition of C_2 should be consistent with the definition of C_4 which is $C_4.C_4$, and the extra minus sign is canceled.)

4.2.4 t_{2g} orbital splitting with spin-orbit coupling and C_{4h} site symmetry considered.

Within the t_{2g} orbitals, the C_{4h} CEF can be parameterized by

$$H_{C_{4h}} = \begin{pmatrix} \delta_1 & 0 & 0 \\ 0 & \delta_1 & 0 \\ 0 & 0 & \delta_2. \end{pmatrix} \tag{4.16}$$

Here, the basis is ordered as yz, zx, xy. The matrix is constrained by the time-reversal and C_{4z} operation. For the d orbitals, under C_{4z} constrain

$$H_{C_{4h}} = \begin{pmatrix} \delta_1 & i\delta_1' & 0 & 0 & 0 \\ -i\delta_1' & \delta_1 & 0 & 0 & 0 \\ 0 & 0 & \delta_2 & 0 & \Delta_5 \\ 0 & 0 & 0 & \delta_3 & 0 \\ 0 & 0 & \Delta_5^* & 0 & \delta_4 \end{pmatrix}. \tag{4.17}$$

C_{4h}	C_{4z}	C_{2z}
Γ_5^+	w	i
Γ_6^+	w^*	$-i$
Γ_7^+	$-w$	i
Γ_8^+	$-w^*$	$-i$

Table 4.2: Relevant irreducible representation of C_{4h}. Here $w = exp[i\frac{\pi}{4}]$.

Here, all δ_i are real parameters, Δ_5 can, in general, be a complex number. Once time-reversal symmetry is considered

$$H_{C_{4h}} = \begin{pmatrix} \delta_1 & 0 & 0 & 0 & 0 \\ 0 & \delta_1 & 0 & 0 & 0 \\ 0 & 0 & \delta_2 & 0 & \delta_5 \\ 0 & 0 & 0 & \delta_3 & 0 \\ 0 & 0 & \delta_5 & 0 & \delta_4 \end{pmatrix}, \tag{4.18}$$

we need only five real parameters to describe the C_{4h} crystal fields. However, if we truncated the Hilbert space into t_{2g} manifold, the system did not have the ability to distinguish D_{4h} and C_{4h} crystal field environment. The only method for d_{xy} orbital to notice the difference between D_{4h} and C_{4h} is through the coupling with $d_{x^2-y^2}$ orbitals. Here, $10Dq \sim 4eV$. The influence of C_{4h} environment is relevant only when $\delta_5 \sim 4eV$. In our system, it is very unlikely to happen. Thus, we will have the conclusion that the influence of C_{4h} crystal field effectively change the relative energies of xy and yz, zx orbitals without changing the symmetry properties of the wave function significantly. **Thus, the effects of C_{4h} environment on t_{2g} orbitals is to renormalize the value of Δ without changing the wave function symmetry properties from D_{4h} irreducible representation significantly.**

4.3 On-site electronic Raman effect- group structure and selection rule

In FIG.4.5, we see that the local levels have different schemes of separation. The various schemes of separation correspond to different selection rules for the electron Raman scattering. Here we will consider the simplified case without bond angle distortion first. In that case, the site

symmetry is consistent with the point group D_{4h}. We develop the corresponding selection rule for D_{4h} point group first. The situation with C_{4h} will be considered later.

4.3.1 Tetragonal distorted cubic CEF(D_{4h}) and selection rule

For tetragonal distorted CEF, d orbitals will split into doublets which transform according to irreducible representation Γ_6^+ or Γ_7^+ of D_{4h} point group. The initial and final state for electron Raman scattering can be described as the FIG. 4.6.

Next, we consider the possible transition and the corresponding polarization. The lowest and the fourth doublet transform according to Γ_6^+, others transform according to Γ_7^+. Therefore, the $\Gamma_7^+ \to \Gamma_7^+$ are (a)(c)(h), $\Gamma_7^+ \to \Gamma_6^+$ are (b)(g), $\Gamma_6^+ \to \Gamma_7^+$ are (d)(f), $\Gamma_6^+ \to \Gamma_6^+$ are (e). According to the Koster's table[81]

$$\begin{aligned}
\Gamma_7^+ \times \Gamma_7^+ &= \Gamma_1^+ + \Gamma_2^+ + \Gamma_5^+ \\
\Gamma_7^+ \times \Gamma_6^+ &= \Gamma_3^+ + \Gamma_4^+ + \Gamma_5^+ \\
\Gamma_6^+ \times \Gamma_6^+ &= \Gamma_1^+ + \Gamma_2^+ + \Gamma_5^+
\end{aligned} \tag{4.19}$$

The corresponding polarization are

$$\begin{aligned}
\Gamma_1^+(A_{1g}) &= \begin{pmatrix} a & 0 & 0 \\ 0 & a & 0 \\ 0 & 0 & b \end{pmatrix}; \Gamma_2^+(A_{2g}) = \begin{pmatrix} 0 & c & 0 \\ -c & 0 & 0 \\ 0 & 0 & 0 \end{pmatrix}; \Gamma_3^+(B_{1g}) = \begin{pmatrix} d & 0 & 0 \\ 0 & -d & 0 \\ 0 & 0 & 0 \end{pmatrix} \\
\Gamma_4^+(B_{2g}) &= \begin{pmatrix} 0 & e & 0 \\ e & 0 & 0 \\ 0 & 0 & 0 \end{pmatrix}; \Gamma_5^+(E_g) = \begin{pmatrix} 0 & 0 & f \\ 0 & 0 & 0 \\ g & 0 & 0 \end{pmatrix} \begin{pmatrix} 0 & 0 & 0 \\ 0 & 0 & f \\ 0 & g & 0 \end{pmatrix}.
\end{aligned} \tag{4.20}$$

When time-reversal symmetry is considered, only $\Gamma_1^+(A_{1g})$ and $\Gamma_3^+(B_{1g})$ component are allowed. The derivation of those matrices is in the appendix 4.5.1.

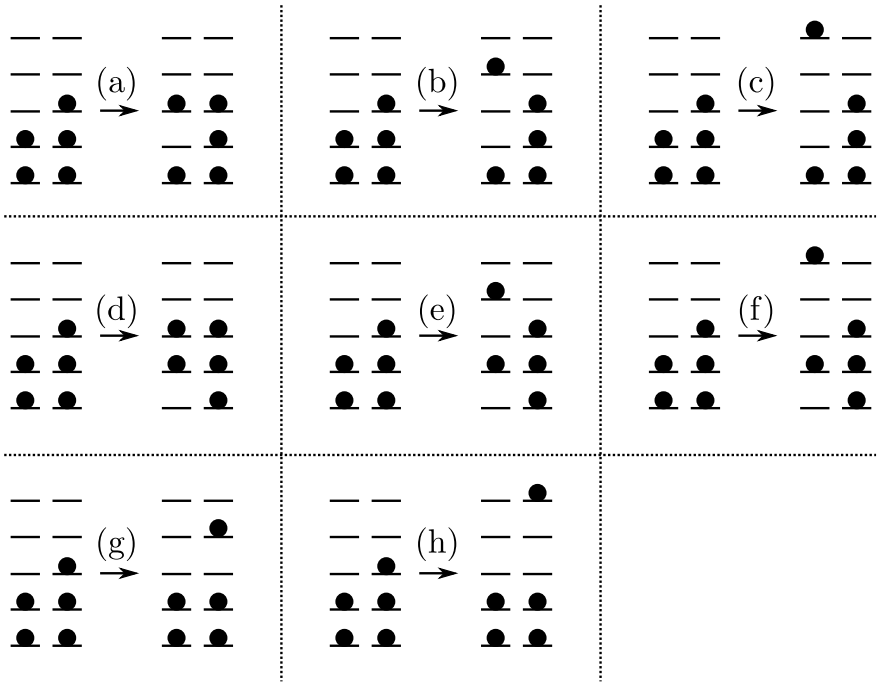

Figure 4.6: Different initial and final state for electron Raman scattering. The doublets are arranged according to FIG. 4.5 (c).

From above relation, we know those electron transitions should produce peaks that are observable at the specific polarization. For example, the Γ_7^+, Γ_7^+ transition should produce a peak that contains Γ_1^+ component. The polarization dependence of the single-ion cross section without z direction can be obtained from reference.

$$\begin{aligned} \Gamma_7^+ \to \Gamma_7^+ \quad &: \quad |a\,(\boldsymbol{e}_s^x \boldsymbol{e}_i^x + \boldsymbol{e}_s^y \boldsymbol{e}_i^y)\,|^2 \\ \Gamma_6^+ \to \Gamma_7^+ \quad &: \quad |d\,(\boldsymbol{e}_s^x \boldsymbol{e}_i^x - \boldsymbol{e}_s^y \boldsymbol{e}_i^y)\,|^2 \end{aligned} \tag{4.21}$$

In the experiments, we have xx,$x'x'$,xy,$x'y'$ where $\boldsymbol{e}_x = (1,0,0), \boldsymbol{e}_y = (0,1,0), \boldsymbol{e}_{x'} = (\frac{1}{\sqrt{2}}, \frac{1}{\sqrt{2}}, 0), \boldsymbol{e}_{y'} = (-\frac{1}{\sqrt{2}}, \frac{1}{\sqrt{2}}, 0)$. Hence, the experiments should be able to be described by those parameters

$$\begin{aligned} xx \quad &: |a|^2 + |d|^2 \\ x'x' \quad &: |a|^2 \\ xy \quad &: 0 \\ x'y' \quad &: |d|^2. \end{aligned} \tag{4.22}$$

However, this symmetry argument just gives the possible selection rule but did not provide the relative amplitude of those components. To estimate the relative intensity we need to do more detailed calculation. Only processes $(a)(d)$ fit into the right energy window. (a) can contribute the $\Gamma_1^+(A_{1g})$, (b) can contributes the $\Gamma_3^+(B_{1g})$ signal.

4.3.2 C_{4h} site symmetry of Ir site and selection rule

The real site symmetry is C_{4h}. The compatibility relation of D_{4h} and C_{4h} is $\Gamma_6^+ = \Gamma_5^+ + \Gamma_6^+$ and $\Gamma_7^+ = \Gamma_7^+ + \Gamma_8^+$. Similarly, we can find the corresponding polarization components. From the reference, the polarization dependence of the single-ion cross section without z direction can be obtained from references.

$$\begin{aligned} \Gamma_5^+ + \Gamma_6^+ \to \Gamma_5^+ + \Gamma_6^+ (\Gamma_7^+ + \Gamma_8^+ \to \Gamma_7^+ + \Gamma_8^+) \quad &: 2\Gamma_1^+ + \Gamma_3^+ + \Gamma_4^+ \\ \Gamma_5^+ + \Gamma_6^+ \to \Gamma_7^+ + \Gamma_8^+ \quad &: 2\Gamma_2^+ + \Gamma_3^+ + \Gamma_4^+. \end{aligned} \tag{4.23}$$

Here,

$$\Gamma_1^+ = \begin{pmatrix} a & c & 0 \\ -c & a & 0 \\ 0 & 0 & b \end{pmatrix}; \Gamma_2^+ = \begin{pmatrix} d & e & 0 \\ e & -d & 0 \\ 0 & 0 & 0 \end{pmatrix}; \Gamma_3^+ + \Gamma_4^+ = \begin{pmatrix} 0 & 0 & f \\ 0 & 0 & h \\ g & i & 0 \end{pmatrix} \begin{pmatrix} 0 & 0 & -h \\ 0 & 0 & f \\ -i & g & 0 \end{pmatrix} \quad (4.24)$$

The detail is shown in 4.5.2

4.3.3 Band structure argument

The intra-site Raman process can happen when the intermediate state is parity odd. However, the possible intra-site Raman process will create a hole in the $j_{eff} = \frac{3}{2}$ band. Since the bandwidth of $j_{eff} = \frac{3}{2}$ band is much larger than $j_{eff} = \frac{1}{2}$ band. The corresponding peak width for intra-site transition will roughly be of the same order of the bandwidth for $j_{eff} = \frac{3}{2}$ band. Thus, in the experiment, the peak is too broad to be observed.

Because of that, we are supposed to look for inter-site transition which happened within the $j_{eff} = \frac{1}{2}$ band and is possible to be observed in the Raman experiments.

4.4 Inter-site electronic Raman effect

4.4.1 The cluster picture

D_{4h}:Ir^{4+} ring cluster

The previous process is the intra-site transition. For the inter-site transition, we can try to apply the cluster picture. For simplicity, we assume the site symmetry is identical with the point group symmetry D_{4h} of the oxygen cage. When electron tunnel from one Ir^{4+} to another, it can tunnel to its four neighbors with equal probability. Thus, the final state supposes to be the linear combination of the four local state, the A doublets, which transform according to Γ_7^+ of D_{4h} as shown in FIG. 4.7.

The wave function of the outer 4 Ir^{4+} can generally be written as

$$|\psi_{out}, \sigma\rangle = \frac{1}{N}\left(c_1|1, A, \sigma\rangle + c_2|2, A, \sigma\rangle + c_3|3, A, \sigma\rangle + c_4|4, A, \sigma\rangle\right), \quad (4.25)$$

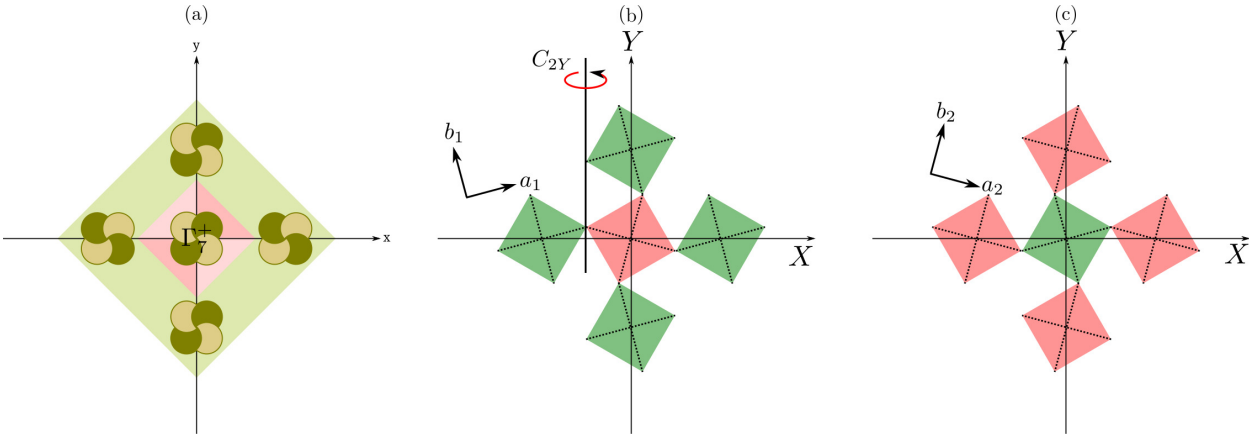

Figure 4.7: (a)The cluster of Ir^{4+} ion. The light green zone means the wave function of the four Ir^{4+} is the linear superposition of the site wave function which transforms according to Γ_7^+ of D_{4h} group. The pink region represents the three-dimensional cluster cage which is formed by oxygen p orbitals.(b) The real situation where the site symmetry is C_{4h}. Here, C_{2Y} is the C_2 rotation along the global Y axis. (c) The case where the distortion is in another direction.

where N is the normalization factor and $|c_i|^2 = 1$ are the phase factors. σ is the pseudo spin index. Since the wave function at different sites, in general, may not be orthogonal, $|N|^2 = \sum_{i,j} c_i^* c_j \langle i, \Gamma_7^+ | j, \Gamma_7^+ \rangle$. We temporally switch the label of sites into $\{1,2,3,4\} \equiv \{+x, +y, -x, -y\}$ for notation convenience.

Now we assume the overlap between Γ_7^+ for different sites is small. The transformation properties should not depend on the magnitude of lattice constant. Under that situation, we will focus on the choice of relative phase factor in the linear combination.

Now, we will discuss how that phase choice transforms under D_{4h} point group. The two trivial choice are $\frac{1}{2}(1,1,1,1)$ which transform according to Γ_1^+ and $\frac{1}{2}(1,-1,1,-1)$ which transform according to Γ_3^+.

The two-dimensional irreducible representation can be constructed as follow. Let's assume $w = exp\left[i\frac{\pi}{4}\right]$. $|1\rangle = \frac{1}{2}\left(w^7, w^5, w^3, w\right)$ represent the coefficient for site 1,2,3,4. Another state $|2\rangle = \frac{1}{2}\left(w, w^3, w^5, w^7\right)$. Those two state form a two-dimensional irreducible representation of D_{4h}. We can construct the matrix representation of $\langle i|C_4|j\rangle$ and they are listed below.

$$C_4 \sim \begin{pmatrix} i & 0 \\ 0 & -i \end{pmatrix}; C_2 \sim \begin{pmatrix} -1 & 0 \\ 0 & -1 \end{pmatrix}; C_{2x} \sim \begin{pmatrix} 0 & i \\ -i & 0 \end{pmatrix}; C_{x=y} \sim \begin{pmatrix} 0 & -1 \\ -1 & 0 \end{pmatrix};$$
$$I \sim \begin{pmatrix} -1 & 0 \\ 0 & -1 \end{pmatrix} \tag{4.26}$$

From that representation, we can see $|1\rangle$ and $|2\rangle$ form a two-dimensional representation, Γ_5^-.

After giving the representation and basis explicitly above, we are going to argue the three irreducible representation above is complete.

For one-dimensional irreducible representation, only $\Gamma_{1,3}^{\pm}$ are possible. Since for (c_1, c_2, c_3, c_4), the matrix element of C_{2x} is $\frac{1}{4}(1 + 1 + c_2^* c_4 + c_2 c_4^*)$. This value can never be -1. Thus we rule out half of the one-dimensional irreducible representation. Also, for inversion, the matrix element will be $\frac{1}{4}(c_1^* c_3 + c_3 c_1^* + c_2^* c_4 + c_4 c_2^*) = \frac{1}{4}\left(|c_1 + c_3|^2 + |c_2 + c_4|^2 - 4\right)$. This quantity can be -1 only when $c_1 + c_3 = c_2 + c_4 = 0$. If it is true, we can construct the character for C_4 rotation, it will be

$\frac{1}{2}(c_2^* c_1 - c_1^* c_2)$ which is a pure imaginary number or zero. No one-dimensional irreducible representation satisfied this requirement, so it must be some part of higher dimensional representation.

For two-dimensional irreducible representation, only Γ_5^- can be created by this method. Choosing the two-dimensional basis to be (c_1, c_2, c_3, c_4) and (d_1, d_2, d_3, d_4), we can calculate the character for C_{2x}. The character will be $\frac{1}{4}\left(|c_2 + c_4|^2 + |d_2 + d_4|^2\right)$. From the character table, we require this to be zero for both $\Gamma_5^{\pm}$. Thus, we have $c_2 = -c_4$ and $d_2 = -d_4$. Similarly for C_{2y} we will have the constraints $c_1 = -c_3$ and $d_1 = -d_3$. With those constraints, the character for inversion can be derived to be -2. Thus only Γ_5^- is possible.

Thus the ring cluster state, which including the phase factor and the local A doublets, can only transform according to

$$\begin{aligned}
|\alpha_1, \pm\rangle &= \frac{1}{2}\left(|1, A, \pm\rangle + |2, A, \pm\rangle + |3, A, \pm\rangle + |4, A, \pm\rangle\right) \sim \Gamma_1^+ \otimes \Gamma_7^+ \sim \Gamma_7^+ \\
|\alpha_2, \pm\rangle &= \frac{1}{2}\left(|1, A, \pm\rangle - |2, A, \pm\rangle + |3, A, \pm\rangle - |4, A, \pm\rangle\right) \sim \Gamma_3^+ \otimes \Gamma_7^+ \sim \Gamma_6^+ \\
|\beta_1, \pm\rangle &= \frac{1}{2}\left(w^{\mp 7}|1, A, \pm\rangle + w^{\mp 5}|2, A, \pm\rangle + w^{\mp 3}|3, A, \pm\rangle + w^{\mp 1}|4, A, \pm\rangle\right) \sim \Gamma_6^- \\
|\beta_2, \pm\rangle &= \frac{1}{2}\left(w^{\pm 7}|1, A, \pm\rangle + w^{\pm 5}|2, A, \pm\rangle + w^{\pm 3}|3, A, \pm\rangle + w^{\pm 1}|4, A, \pm\rangle\right) \sim \Gamma_7^- \\
|\beta\rangle &\sim \Gamma_5^- \otimes \Gamma_7^+ \sim \Gamma_6^- + \Gamma_7^- \sim |\beta_1\rangle + |\beta_2\rangle.
\end{aligned} \tag{4.27}$$

Since the initial state transforms like Γ_7^+, the final state should be $|\alpha_i\rangle$ because of the parity should be identical for Raman process. On the other hand, the intermediate state should be Raman forbidden which could be $|\beta_i\rangle$ for Ir-Ir-Ir process.

C_{4h}:

(A small surprise: Under C_{4h}, the Γ_7^+ will turn into $\Gamma_7^+ + \Gamma_8^+$, which transform according to $|-\frac{3}{2}\rangle$ and $|\frac{3}{2}\rangle$.)

Since C_{4h} is a proper subgroup of D_{4h}, I would guess the relation is similar

$$\begin{aligned}
|\alpha_1'\rangle \sim &\quad \Gamma_1^+ \otimes (\Gamma_7^+ + \Gamma_8^+) \sim \Gamma_7^+ + \Gamma_8^+ \sim |\pm\frac{3}{2}\rangle \\
|\alpha_2'\rangle \sim &\quad \Gamma_2^+ \otimes (\Gamma_7^+ + \Gamma_8^+) \sim \Gamma_5^+ + \Gamma_6^+ \sim |\pm\frac{1}{2}\rangle \\
|\beta'\rangle \sim &\quad (\Gamma_3^- + \Gamma_4^-) \otimes (\Gamma_7^+ + \Gamma_8^+) \sim (\Gamma_5^- + \Gamma_6^-) + (\Gamma_7^- + \Gamma_8^-).
\end{aligned} \tag{4.28}$$

4.4.2 Selection rules(Site symmetry D_{4h})

The selection rules of the inter-site process are identical with the intra-site process. Only diagonal component are allowed under D_{4h} and time-reversal symmetry.

4.4.3 Selection rules(Site symmetry C_{4h})

Following the conclusion of the inter-site process, the off-diagonal components are allowed if we only consider site symmetry.

Next, we notice the bond angle is not perfect 180°. We now try to consider a unit cell with two Ir^{4+} where the two CEF are rotated counterclockwise and clockwise as the left green one and the central red one in FIG.4.8 (b). Also we label the local axis of the sublattice 1(green) as a_1, b_1, c_1 and sublattice 2(red) as a_2, b_2, c_2. Now consider initial state as $|I_B\rangle = |B_1, \sigma\rangle \otimes |B_2, -\sigma\rangle$ and $|I_C\rangle = |C_1, \sigma\rangle \otimes |C_2, -\sigma\rangle$. Final state as $|F_B\rangle = \frac{1}{\sqrt{2}} (|A_1, \sigma\rangle \otimes |B_2, -\sigma\rangle + |B_1, \sigma\rangle \otimes |A_2, -\sigma\rangle)$ and $|F_C\rangle = \frac{1}{\sqrt{2}} (|A_1, \sigma\rangle \otimes |C_2, -\sigma\rangle + |C_1, \sigma\rangle \otimes |A_2, -\sigma\rangle)$. The fermionic anti-symmetric properties can be shown by projecting to real space by $\frac{1}{\sqrt{2}}(\langle|r_1|\langle r_2| - \langle r_2|\langle r_1|)$.

The Raman operator is $R^{\mu\nu} = R_1^{\mu\nu} \otimes \mathbf{1}_2 + \mathbf{1}_1 \otimes R_2^{\mu\nu}$.

$$\langle F_s|R^{\mu\nu}|I_s\rangle = \frac{1}{\sqrt{2}} \left[\langle A_1, \sigma|R_1^{\mu\nu}|s_1, \sigma\rangle + \langle A_2, -\sigma|R_2^{\mu\nu}|s_2, -\sigma\rangle\right], \tag{4.29}$$

here, $s = B, C$ as the initial state.

Now, if we consider the C_{2Y} rotation which is equivalent to interchange site 1 and 2 after making a local C_{2y} rotation. Also, the local C_{2y} and C_{2x} rotation just switch the pseudo spin and add a phase factor for all doublets we are interests in.

$$\begin{aligned} C_{2x} &: |\pm\rangle \to -i|\mp\rangle \\ C_{2y} &: |\pm\rangle \to \pm|\mp\rangle \end{aligned} \tag{4.30}$$

We can see that

$$\begin{aligned} \langle A_2, -\sigma|R_2^{\mu\nu}|s_2, -\sigma\rangle &= \langle A_2, -\sigma|C_{2Y}^{-1}C_{2Y}R_2^{\mu\nu}C_{2Y}^{-1}C_{2Y}|s_2, -\sigma\rangle \\ &= \langle A_1, \sigma|(C_{2Y}R_2^{\mu\nu}C_{2Y}^{-1})|s_1, \sigma\rangle. \end{aligned} \tag{4.31}$$

For the X, Y component of the Raman operator, $C_{2Y} R_2^{XY} C_{2Y}^{-1} = -R_1^{XY}$, which means $\langle F_s | R^{\mu\nu} | I_s \rangle = 0$ when $\mu = X, \nu = Y$. Therefore, even though the site symmetry does not have the C_{2x}, C_{2y} symmetry, the space group has the symmetry C_{2X}, C_{2Y} which provides similar effect to cancel the off diagonal elements.

4.5 Selection rules

4.5.1 D_{4h} case

Here, we discuss the selection rule for doublets Γ_6^+ and Γ_7^+ for D_{4h} point group. The part that determined the selection rule is the Raman tensor $R^{\mu\nu}$. In the experiment, we only care about the case where $\mu, \nu = x, y$.

The initial and final states can be $|\Gamma_6^+, \pm\rangle$ or $|\Gamma_7^+, \pm\rangle$. We want to analyze how $\langle F | R^{\mu\nu} | I \rangle$ transform under D_{4h} symmetry.

$\Gamma_j \to \Gamma_j$

For C_{2z},

$$\begin{aligned}
\langle \Gamma_j, \pm | xx | \Gamma_j, \pm \rangle &\xrightarrow{C_{2z}} \langle \Gamma_j, \pm | (\mp i)(-x)(-x)(\pm i) | \Gamma_j, \pm \rangle = \langle \Gamma_j, \pm | xx | \Gamma_j, \pm \rangle, \\
\langle \Gamma_j, \pm | xx | \Gamma_j, \mp \rangle &\xrightarrow{C_{2z}} \langle \Gamma_j, \pm | (\mp i)(-x)(-x)(\mp i) | \Gamma_j, \mp \rangle = -\langle \Gamma_j, \pm | xx | \Gamma_j, \mp \rangle, \\
\langle \Gamma_j, \pm | xy | \Gamma_j, \pm \rangle &\xrightarrow{C_{2z}} \langle \Gamma_j, \pm | (\mp i)(-x)(-y)(\pm i) | \Gamma_j, \pm \rangle = \langle \Gamma_j, \pm | xy | \Gamma_j, \pm \rangle, \\
\langle \Gamma_j, \pm | xy | \Gamma_j, \mp \rangle &\xrightarrow{C_{2z}} \langle \Gamma_j, \pm | (\mp i)(-x)(-y)(\mp i) | \Gamma_j, \mp \rangle = -\langle \Gamma_j, \pm | xy | \Gamma_j, \mp \rangle. \qquad (4.32)
\end{aligned}$$

Thus, $R^{\mu\nu}$ is diagonal in spin space.

For C_{4z},

$$\begin{aligned}
\langle \Gamma_j, \pm | xx | \Gamma_j, \pm \rangle &\xrightarrow{C_{4z}} \langle \Gamma_j, \pm | (-1)^j (exp[\pm i \frac{\pi}{4}])(y)(y)(-1)^j (exp[\mp i \frac{\pi}{4}]) | \Gamma_j, \pm \rangle \\
&= \langle \Gamma_j, \pm | yy | \Gamma_j, \pm \rangle \\
\langle \Gamma_j, \pm | xy | \Gamma_j, \pm \rangle &\xrightarrow{C_{4z}} \langle \Gamma_j, \pm | (-1)^j (exp[\pm i \frac{\pi}{4}])(y)(-x)(-1)^j (exp[\mp i \frac{\pi}{4}]) | \Gamma_j, \pm \rangle \\
&= -\langle \Gamma_j, \pm | yx | \Gamma_j, \pm \rangle. \qquad (4.33)
\end{aligned}$$

The off diagonal symmetry part is forbidden, only asymmetry component exist.

For C_{2x},

$$\begin{aligned}
\langle\Gamma_j,\pm|xx|\Gamma_j,\pm\rangle &\xrightarrow{C_{2x}} \langle\Gamma_j,\mp|(i)xx(-i)|\Gamma_j,\mp\rangle = \langle\Gamma_j,\mp|xx|\Gamma_j,\mp\rangle,\\
\langle\Gamma_j,\pm|xy|\Gamma_j,\pm\rangle &\xrightarrow{C_{2x}} \langle\Gamma_j,\mp|(i)x(-y)(-i)|\Gamma_j,\mp\rangle = -\langle\Gamma_j,\mp|xy|\Gamma_j,\mp\rangle.
\end{aligned} \tag{4.34}$$

For C_{2xy},

$$\begin{aligned}
\langle\Gamma_j,\pm|xx|\Gamma_j,\pm\rangle &\xrightarrow{C_{2xy}} \langle\Gamma_j,\mp|(-1)^j(exp[\mp i\frac{\pi}{4}])yy(-1)^j(exp[\pm i\frac{\pi}{4}])|\Gamma_j,\mp\rangle = \langle\Gamma_j,\mp|yy|\Gamma_j,\mp\rangle,\\
\langle\Gamma_j,\pm|xy|\Gamma_j,\pm\rangle &\xrightarrow{C_{2xy}} \langle\Gamma_j,\mp|(-1)^j(exp[\mp i\frac{\pi}{4}])yx(-1)^j(exp[\pm i\frac{\pi}{4}])|\Gamma_j,\mp\rangle = \langle\Gamma_j,\mp|yx|\Gamma_j,\mp\rangle.
\end{aligned} \tag{4.35}$$

C_{2x} and C_{2xy} did not give further constrain to the matrix R.

Above relation suggest

$$R = \begin{pmatrix} a & c & ? \\ -c & a & ? \\ ? & ? & ? \end{pmatrix}, \tag{4.36}$$

for $\Gamma_j \to \Gamma_j$ transition without time-reversal symmetry.

When time reversal symmetry is considered,

$$\langle\Gamma_j,\pm|xy|\Gamma_j,\pm\rangle \xrightarrow{\mathcal{T}} \langle\Gamma_j,\mp|(\pm1)xy(\pm1)|\Gamma_j,\mp\rangle = \langle\Gamma_j,\mp|xy|\Gamma_j,\mp\rangle. \tag{4.37}$$

Together with C_{2x}, no off-diagonal components are allowed for $\Gamma_j \to \Gamma_j$.

$$R = \begin{pmatrix} a & 0 & ? \\ 0 & a & ? \\ ? & ? & ? \end{pmatrix}, \tag{4.38}$$

when both D_{4h} symmetry and time-reversal symmetry is considered.

$\Gamma_j \to \Gamma_{j'}$

For C_{2z}, Γ_j and $\Gamma_{j'}$ transform in the same way. Thus,

$$\begin{aligned}
\langle\Gamma_j,\pm|xx|\Gamma_{j'},\pm\rangle &\xrightarrow{C_{2z}} \langle\Gamma_j,\pm|(\mp i)(-x)(-x)(\pm i)|\Gamma_{j'},\pm\rangle = \langle\Gamma_j,\pm|xx|\Gamma_{j'},\pm\rangle,\\
\langle\Gamma_j,\pm|xx|\Gamma_{j'},\mp\rangle &\xrightarrow{C_{2z}} \langle\Gamma_j,\pm|(\mp i)(-x)(-x)(\mp i)|\Gamma_{j'},\mp\rangle = -\langle\Gamma_j,\pm|xx|\Gamma_{j'},\mp\rangle,\\
\langle\Gamma_j,\pm|xy|\Gamma_{j'},\pm\rangle &\xrightarrow{C_{2z}} \langle\Gamma_j,\pm|(\mp i)(-x)(-y)(\pm i)|\Gamma_{j'},\pm\rangle = \langle\Gamma_j,\pm|xy|\Gamma_{j'},\pm\rangle,\\
\langle\Gamma_j,\pm|xy|\Gamma_{j'},\mp\rangle &\xrightarrow{C_{2z}} \langle\Gamma_j,\pm|(\mp i)(-x)(-y)(\mp i)|\Gamma_{j'},\mp\rangle = -\langle\Gamma_j,\pm|xy|\Gamma_{j'},\mp\rangle. \qquad (4.39)
\end{aligned}$$

Thus, $R^{\mu\nu}$ is diagonal in spin space, also.

For C_{4z},

$$\begin{aligned}
\langle\Gamma_j,\pm|xx|\Gamma_{j'},\pm\rangle &\xrightarrow{C_{4z}} \langle\Gamma_j,\pm|(-1)^j(exp[\pm i\frac{\pi}{4}])(y)(y)(-1)^{j'}(exp[\mp i\frac{\pi}{4}])|\Gamma_{j'},\pm\rangle\\
&= -\langle\Gamma_j,\pm|yy|\Gamma_{j'},\pm\rangle\\
\langle\Gamma_j,\pm|xy|\Gamma_{j'},\pm\rangle &\xrightarrow{C_{4z}} \langle\Gamma_j,\pm|(-1)^j(exp[\pm i\frac{\pi}{4}])(y)(-x)(-1)^{j'}(exp[\mp i\frac{\pi}{4}])|\Gamma_{j'},\pm\rangle\\
&= \langle\Gamma_j,\pm|yx|\Gamma_{j'},\pm\rangle. \qquad (4.40)
\end{aligned}$$

The off diagonal asymmetry part is forbidden, only symmetry component exist.

For C_{2x},Γ_6^+ and Γ_7^+ transform in the same way. Thus,

$$\begin{aligned}
\langle\Gamma_j,\pm|xx|\Gamma_{j'},\pm\rangle &\xrightarrow{C_{2x}} \langle\Gamma_j,\mp|(i)xx(-i)|\Gamma_{j'},\mp\rangle = \langle\Gamma_j,\mp|xx|\Gamma_{j'},\mp\rangle,\\
\langle\Gamma_j,\pm|xy|\Gamma_{j'},\pm\rangle &\xrightarrow{C_{2x}} \langle\Gamma_j,\mp|(i)x(-y)(-i)|\Gamma_{j'},\mp\rangle = -\langle\Gamma_j,\mp|xy|\Gamma_{j'},\mp\rangle. \qquad (4.41)
\end{aligned}$$

For C_{2xy},

$$\begin{aligned}
\langle\Gamma_j,\pm|xx|\Gamma_{j'},\pm\rangle &\xrightarrow{C_{2xy}} \langle\Gamma_j,\mp|(-1)^j(exp[\mp i\frac{\pi}{4}])yy(-1)^{j'}(exp[\pm i\frac{\pi}{4}])|\Gamma_{j'},\mp\rangle = -\langle\Gamma_j,\mp|yy|\Gamma_j,\mp\rangle,\\
\langle\Gamma_j,\pm|xy|\Gamma_{j'},\pm\rangle &\xrightarrow{C_{2xy}} \langle\Gamma_j,\mp|(-1)^j(exp[\mp i\frac{\pi}{4}])yx(-1)^{j'}(exp[\pm i\frac{\pi}{4}])|\Gamma_{j'},\mp\rangle = -\langle\Gamma_j,\mp|yx|\Gamma_{j'},\mp\rangle.
\end{aligned} \qquad (4.42)$$

C_{2x} and C_{2xy} did not give further constrain to the matrix R.

Above relation suggest

$$R = \begin{pmatrix} d & e & ? \\ e & -d & ? \\ ? & ? & ? \end{pmatrix}, \qquad (4.43)$$

for $\Gamma_j \to \Gamma_{j'}$ transition without time-reversal symmetry.

When time reversal symmetry is considered,

$$\langle \Gamma_j, \pm|xy|\Gamma_{j'}, \pm\rangle \quad \xrightarrow{\mathcal{T}} \quad \langle \Gamma_j, \mp|(\pm 1)xy(\pm 1)|\Gamma_{j'}, \mp\rangle = \langle \Gamma_j, \mp|xy|\Gamma_{j'}, \mp\rangle. \tag{4.44}$$

Together with C_{2x}, no off-diagonal components are allowed for $\Gamma_j \to \Gamma_{j'}$.

$$R = \begin{pmatrix} d & 0 & ? \\ 0 & -d & ? \\ ? & ? & ? \end{pmatrix}, \tag{4.45}$$

when both D_{4h} symmetry and time-reversal symmetry is considered.

4.5.2 C_{4h} case

For C_{4h}, the symmetry operation C_{2x} and C_{2xy} cannot be used. From Koster's table, we can know that, under C_{2z}, the eigen states transform exactly as those in D_{4h} case. Thus, R matrix is diagonal in spin space. Only C_{4z} needs to be discussed.

Note that, the basis is chosen such that time reversal operator satisfied

$$\begin{aligned} \mathcal{T}|\Gamma_5\rangle &= |\Gamma_6\rangle; \mathcal{T}|\Gamma_6\rangle = -|\Gamma_5\rangle \\ \mathcal{T}|\Gamma_7\rangle &= |\Gamma_8\rangle; \mathcal{T}|\Gamma_8\rangle = -|\Gamma_7\rangle. \end{aligned} \tag{4.46}$$

$\Gamma_{5/6} \to \Gamma_{5/6}$ or **$\Gamma_{7/8} \to \Gamma_{7/8}$**

$$\begin{aligned} \langle \Gamma_{5/6}|xx|\Gamma_{5/6}\rangle &\xrightarrow{C_{4z}} \langle \Gamma_{5/6}|(t^*)yy(t)|\Gamma_{5/6}\rangle = \langle \Gamma_{5/6}|yy|\Gamma_{5/6}\rangle, \\ \langle \Gamma_{5/6}|xy|\Gamma_{5/6}\rangle &\xrightarrow{C_{4z}} -\langle \Gamma_{5/6}|(t^*)yx(t)|\Gamma_{5/6}\rangle = -\langle \Gamma_{5/6}|yx|\Gamma_{5/6}\rangle \end{aligned} \tag{4.47}$$

. Here, t is just the complex phase factor. The same relation holds for $\Gamma_{7/8} \to \Gamma_{7/8}$.

Next, time-reversal symmetry implies $\langle \Gamma_{5/6}|xx|\Gamma_{5/6}\rangle \xrightarrow{\mathcal{T}} \langle \Gamma_{6/5}|xx|\Gamma_{6/5}\rangle$ and $\langle \Gamma_{5/6}|xy|\Gamma_{5/6}\rangle \xrightarrow{\mathcal{T}}$

$\langle\Gamma_{6/5}|xy|\Gamma_{6/5}\rangle$. This constrain also applies on $\Gamma_{7/8} \to \Gamma_{7/8}$. Thus,

$$R = \begin{pmatrix} a & c & ? \\ -c & a & ? \\ ? & ? & ? \end{pmatrix}. \tag{4.48}$$

$\mathbf{\Gamma_{5/6} \to \Gamma_{7/8}}$

$$\begin{aligned} \langle\Gamma_{5/6}|xx|\Gamma_{7/8}\rangle &\xrightarrow{C_{4z}} \langle\Gamma_{5/6}| - (k^*)yy(k)|\Gamma_{7/8}\rangle = -\langle\Gamma_{5/6}|yy|\Gamma_{7/8}\rangle, \\ \langle\Gamma_{5/6}|xy|\Gamma_{7/8}\rangle &\xrightarrow{C_{4z}} = -\langle\Gamma_{5/6}| - (k^*)yx(k)|\Gamma_{7/8}\rangle = \langle\Gamma_{5/6}|yx|\Gamma_{7/8}\rangle \end{aligned} \tag{4.49}$$

. Here, k is just the complex phase factor.

Next, time-reversal symmetry implies $\langle\Gamma_{5/6}|xx|\Gamma_{7/8}\rangle \xrightarrow{\mathcal{T}} \langle\Gamma_{6/5}|xx|\Gamma_{8/7}\rangle$ and $\langle\Gamma_{5/6}|xy|\Gamma_{7/8}\rangle \xrightarrow{\mathcal{T}} \langle\Gamma_{6/5}|xy|\Gamma_{8/7}\rangle$.

Thus,

$$R = \begin{pmatrix} d & e & ? \\ e & -d & ? \\ ? & ? & ? \end{pmatrix}. \tag{4.50}$$

4.6 Results and discussion

4.6.1 Selection rules for intra-site and inter-site transitions.

First we compare these results to a simple calculation of what types of on-site and near neighbor hopping electronic transitions appear in what symmetry and then discuss how the interpretation of the RIXS data proposed in Ref. [176] needs to be reconsidered in light of the Raman results.

The Raman intensity is proportional to [177]:

$$I \propto \frac{1}{Z} \sum_{I,F} \left|\langle F|R_{\mu\nu}|I\rangle\right|^2 e^{-E_I/k_BT} \delta(E_F - E_I - \hbar\omega), \tag{4.51}$$

where I, F label energy eigenstates of the electronic system with energies E_I, E_F, ω is the Raman shift, and Z is the partition function. $R_{\mu\nu}$ is the Raman tensor, with $\mu, \nu = x, y, z$ giving the direction of linear polarization of scattered and incident light in our experiment, respectively. The electronic Raman cross section is typically dominated by the first two terms in perturbation theory [see Eq. (13) of Ref. [177]]. Fig. 4.2 shows that the intensity of the peaks of interest has a strong laser energy-dependence. Since the first order term does not depend on the laser energy , the second order term must dominate. Thus we focus on this contribution, which is given by:

$$R_{\mu\nu} = p_\mu \frac{1}{E_I + \hbar\omega_I - H_{el}} p_\nu, \tag{4.52}$$

where H_{el} is the electronic Hamiltonian, p_μ the electron momentum operator, and ω_I is the frequency of incident light. [Note that we have dropped an additional non-resonant second-order term; see Eq. (13) of Ref. [177].]

In the presence of tetragonal crystal field (CF) and SOC, the t_{2g} manifold splits into three Kramer doublets labeled with j_1, j_2 and $\bar{j}_2$ (Fig. 4.8(a)) [178, 179, 180]. The j ($J^z_{\text{eff}} = \pm 1/2$) and $\bar{j}$ ($J^z_{\text{eff}} = \pm 3/2$) doublets transform differently under D_{4h} symmetry and time reversal (See Appendix B). Note that J^2_{eff} is not a good quantum number under D_{4h} CF.

We adopt a tight-binding description of the electronic states, with $f^\dagger_{\boldsymbol{r}\alpha}$ creating an electron at the Ir lattice site $\boldsymbol{r}$ in the local spin-orbital state α. Here, the spin-orbital state $\alpha \equiv (a, \sigma)$, where $a = j_1, j_2, \bar{j}_2$ labels the local doublets, and $\sigma = 1, 2$ is the pseudo-spin. We work in real-space. In our description of the Raman process, a photon is absorbed near a lattice site $\boldsymbol{r}$, with the resulting excited intermediate state propagating over some distance before emission of a photon near site $\boldsymbol{r}'$. Far enough away from resonance, the intermediate state will propagate only over a short distance; this leads to the expansion

$$R_{\mu\nu} = \sum_{\boldsymbol{r}} M^{\alpha\beta}_{0;\mu\nu}(\boldsymbol{r}) f^\dagger_{\boldsymbol{r}\alpha} f_{\boldsymbol{r}\beta} + M^{\alpha\beta}_{1;\mu\nu}(\boldsymbol{r}) c^\dagger_{\boldsymbol{r}\alpha} f_{\boldsymbol{r}\beta} + \cdots. \tag{4.53}$$

Here the first term represents on-site transitions, while the second term describes inter-site processes, in which an electron moves from a site $\boldsymbol{r}$ to a cluster state created by $c^\dagger_{\boldsymbol{r}\alpha}$. The cluster state

	Non-pseudospin-flip	Pseudospin-flip
$j_2 \to j_1$	xx, $x'x'$ (A_{1g})	xy, $x'y'$ (A_{2g})
$\bar{j}_2 \to j_1$	xx, $x'y'$ (B_{1g})	$x'x'$, xy (B_{2g})

Table 4.3: Polarization and symmetry of on-site Raman transitions with D_{4h} site symmetry. The row indicates the doublets between which the transition occurs, and the column indicates whether a pseudospin flip is involved.

is a linear superposition of spin-orbital states on the four Ir sites nearest to $\boldsymbol{r}$. Sums over repeated indices α, β are implied. Longer range terms have been dropped.

To interpret the experimental results, we assume significant local antiferromagnetic correlations to temperatures well above the Neel temperature ($T_N = 240$ K), focusing here on $T > T_N$, as the gross features of the Raman spectrum remain largely unchanged as T is lowered through T_N. In the low-temperature antiferromagnetic state, the moments lie in the ab-plane, with small canting out of the plane that we ignore [79, 181, 182, 183].

We first consider an idealized situation, where the Ir-O-Ir bond angle is 180° and the site symmetry is D_{4h}. We focus on on-site transitions within the t_{2g} manifold, so $j_2 \to j_1$ and $\bar{j}_2 \to j_1$ are relevant (the energy of the main peak is likely too large for purely magnetic $j_1 \to j_1$ transitions)(Fig. 4.8(a)). The pseudospin structure of each transition is described by the appropriate 2×2 block of the 6×6 matrix $M_{0;\mu\nu}(\boldsymbol{r})$. We always find this 2×2 matrix to be either proportional to the identity matrix (no pseudospin flip), or to the σ^z Pauli matrix (pseudospin flip).

For the on-site transitions, both non-pseudospin-flip and pseudospin-flip processes can occur (See Appendix A). The former should appear in A_{1g} and B_{1g} symmetry and the latter in A_{2g} and B_{2g} symmetry (Table 4.3).

For the inter-site transitions, we consider hopping between j_1 doublets on neighboring sites. An electron hops from site $\boldsymbol{r}$ into a parity-even cluster state, constructed by superposing j_1 doublets on the four neighboring sites (Fig. 4.8(b)). There are two such Raman-active cluster states, one with s-wave symmetry and the other with $d_{x^2-y^2}$ symmetry. In addition, there can be an infrared-active, Raman inactive transition to a p-wave cluster state. The s-wave/$d_{x^2-y^2}$ cluster state transforms identically to the on-site $j/\bar{j}$ doublet. This means the $\boldsymbol{r} \to s/\boldsymbol{r} \to d_{x^2-y^2}$ inter-site process has the

same selection rules as the on-site $j_2 \rightarrow j_1/\bar{j}_2 \rightarrow j_1$ transition respectively. Note that pseudospin-flip processes are forbidden by the combination of local antiferromagnetic correlations and the Pauli principle (see Fig. 4.8(b)).

So far we assumed D_{4h} site symmetry, but, in reality, the Ir-O-Ir bond angle is away from 180° by 22°, lowering the site symmetry to C_{4h} (the point group remains D_{4h}). In this case, both $j_2 \rightarrow j_1$ and $\bar{j}_2 \rightarrow j_1$ transitions (and corresponding inter-site transitions) may produce a non-pseudospin-flip contribution in xy polarization. That this is not seen suggests the site symmetry is effectively D_{4h} to a good approximation.

4.6.2 Discussion

Raman scattering has different matrix elements from RIXS, and thus highlights different excitations. RIXS data are consistent with two dispersing modes whose spectral intensity can be controlled by the scattering angle. These have been assigned (in our notation) to excitons associated with $j_2 \rightarrow j_1$ and $\bar{j}_2 \rightarrow j_1$ intra-site transitions. However, these transitions should produce four distinct excitations, considering that the pseudospin flip and non-flip transitions should have different energies in the presence of magnetic-order. Here we propose that modes seen in RIXS as well as in our data can also originate from inter-site excitations whose energy would correspond to on-site repulsion. Thus more analysis and data are needed to understand the signal seen in RIXS.

In the on-site transitions scenario this means that both pseudospin non-flip transitions are seen close to 0.7 eV with $j_2 \rightarrow j_1/\bar{j}_2 \rightarrow j_1$ appearing in the A_{1g}/B_{1g} symmetry respectively. This scenario necessitates that one or both corresponding pseudospin-flip transitions contribute to the RIXS peak at 0.6 eV and their Raman matrix element is so small that they are not seen in the XY-polarized Raman spectrum where they would appear. While this scenario cannot be ruled out without a better understanding of the Raman matrix elements, we would like to point out that the Raman data were taken over a wide range of laser energies, which always produced no signal in this scattering geometry. We will attempt to look for these excitations covering a wider range of

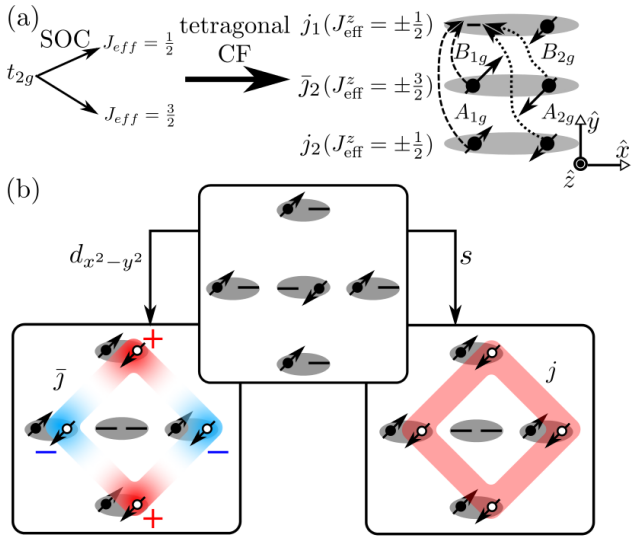

Figure 4.8: Schematic of the on-site and inter-site transitions. (a) Local states and on-site transitions: The SOC and tetragonal CF split the t_{2g} orbitals into three doublets labeled with j_1, $\bar{j}_2$, and j_2. The non-pseudo-spin-flip electronic transition contributes to the A_{1g} and B_{1g} signal, and the pseudo-spin-flip process contributes the A_{2g} and B_{2g} signal. (b) Inter-site transitions: The ground state configuration is described in the top block. The electron can tunnel from the central site to the s-wave/$d_{x^2-y^2}$ cluster state which transforms identically to the on-site $j/\bar{j}$ doublet respectively. The gray oval encloses the states on the same site.

both laser energies and Raman shifts in a future study. This scenario also implies that the splitting between the j_2 and $\bar{j}_2$ levels is 30 meV, not 137 meV as proposed in Ref. [176].

Another possibility is that the RIXS experiments reveal excitons associated with inter-site transitions. In this case three peaks come out naturally with transitions to the s-wave/d-wave cluster states making up the A_{1g}/B_{1g} peaks and the transitions to the p-wave cluster making up the Raman-inactive peak at a lower energy. We note that pseudospin-flip transitions in this scenario are not allowed due to the Pauli exclusion principle.

The third possibility is that the three peaks come from some combination of inter-site and intra-site transitions. We think that this possibility is least likely, because it implies that the on-site repulsion energy should be very similar to the intra-site level splitting, which would be an unlikely coincidence.

Chapter 5

Summary and perspectives

Two questions entangle with the search of topological order. First, where to find the topological order? Second, how to probe topological order? By carefully constructing the microscopic models, we find it is valuable to investigate the strong spin-orbit coupled system and to analyze the symmetry fractionalization pattern of the symmetry enriched topological order.

In this thesis, we study the strong spin-orbit coupled materials. On the most frustrated three-dimensional lattice, pyrochlore lattice, we found the space group allows the existence of the novel dipolar-octupolar doublets. The dipolar-octupolar doublets realize a long-sought realistic model which support quantum spin ices. By applying a magnetic field, we can reduce the pyrochlore lattice to layers of Kagome lattice which could achieve a symmetry-enriched Z_2 topological order. The spin-orbit coupling breaks the continuous spin rotational symmetry and leads to a non-trivial symmetry fractionalization pattern with striking response to classical disclination defect. The symmetry enriched topological orders are robust against perturbations. Spin-orbit coupling might lower the symmetry of the system and make the system difficult to analyze. However, it could be useful to realize signals that can be detected in future numerics and experiments. The pyrochlore and Kagome lattice model indicates the subtle relation between space group symmetry and onsite symmetry when the spin-orbit coupling is included. At the level of modeling, the space group gives non-trivial constraint to the local degrees of freedom. At the level of studying the symmetry fractionalization pattern, the combination of space group and discrete onsite symmetry leads to the vison zero modes.

At this stage, the general experiment method to identify topological order is still lacking. In the future, it is interesting to find other realistic models with similar physics and study the general structure of using space group defects and onsite discrete symmetry to probe topological order.

The nontrivial physics can be traced back to the dipolar-octupolar doublets in the material. The pseudo spin operator can have very different symmetry properties depends on the quantum states. Spin-orbit coupling gives another energy scale to select the novel degrees of freedom and leads to dramatically different model. The mixed multipolar nature of the novel degrees of freedom also raises another perspective to understand the well-studied classical spin ice materials. How the new quantum model changes our understanding of the experiments is also an attractive direction. More broadly, this mechanism could exist in other materials, and its physical consequences are relatively unexplored.

Bibliography

[1] Piers Coleman. Emergence and reductionism: an awkward baconian alliance. arXiv preprint arXiv:1702.06884, 2017.

[2] P. W. Anderson. More is different. Science, 177(4047):393–396, 1972.

[3] Michael Berry. Asymptotics, singularities and the reduction of theories. Studies in Logic and the Foundations of Mathematics, 134:597–607, 1995.

[4] LD Landau. Zur theorie der phasenumwandlungen ii. Phys. Z. Sowjetunion, 11:26–35, 1937.

[5] Paul M Chaikin and Tom C Lubensky. Principles of condensed matter physics. Cambridge university press, 2000.

[6] V. L. Berezinskiĭ. Destruction of Long-range Order in One-dimensional and Two-dimensional Systems having a Continuous Symmetry Group I. Classical Systems. Soviet Journal of Experimental and Theoretical Physics, 32:493, 1971.

[7] V. L. Berezinskiĭ. Destruction of Long-range Order in One-dimensional and Two-dimensional Systems Possessing a Continuous Symmetry Group. II. Quantum Systems. Soviet Journal of Experimental and Theoretical Physics, 34:610, 1972.

[8] J. M. Kosterlitz and D. J. Thouless. Ordering, metastability and phase transitions in two-dimensional systems. Journal of Physics C Solid State Physics, 6:1181–1203, April 1973.

[9] Franz J Wegner. Duality in generalized ising models and phase transitions without local order parameters. Journal of Mathematical Physics, 12(10):2259–2272, 1971.

[10] Tom Banks, R Myerson, and John Kogut. Phase transitions in abelian lattice gauge theories. Nuclear Physics B, 129(3):493–510, 1977.

[11] Robert Savit. Duality in field theory and statistical systems. Reviews of Modern Physics, 52(2):453, 1980.

[12] Xiao-Gang Wen. Artificial light and quantum order in systems of screened dipoles. Phys. Rev. B, 68:115413, Sep 2003.

[13] Michael Levin and Xiao-Gang Wen. Fermions, strings, and gauge fields in lattice spin models. Phys. Rev. B, 67:245316, Jun 2003.

[14] V. Kalmeyer and R. B. Laughlin. Equivalence of the resonating-valence-bond and fractional quantum hall states. Phys. Rev. Lett., 59:2095, 1987.

[15] X. G. Wen, F. Wilczek, and A. Zee. Chiral spin states and superconductivity. Phys. Rev. B, 39:11413, 1989.

[16] Daniel C Tsui, Horst L Stormer, and Arthur C Gossard. Two-dimensional magnetotransport in the extreme quantum limit. Phys. Rev. Lett., 48(22):1559, 1982.

[17] Leon Balents. Spin liquids in frustrated magnets. Nature, 464(7286):199–208, 2010.

[18] Lucile Savary and Leon Balents. Quantum spin liquids: a review. Reports on Progress in Physics, 80(1):016502, 2017.

[19] C. L. Kane and E. J. Mele. Quantum spin hall effect in graphene. Phys. Rev. Lett., 95:226801, Nov 2005.

[20] B Andrei Bernevig, Taylor L Hughes, and Shou-Cheng Zhang. Quantum spin hall effect and topological phase transition in hgte quantum wells. Science, 314(5806):1757–1761, 2006.

[21] Joel E Moore and Leon Balents. Topological invariants of time-reversal-invariant band structures. Physical Review B, 75(12):121306, 2007.

[22] Liang Fu, Charles L Kane, and Eugene J Mele. Topological insulators in three dimensions. Phys. Rev. Lett., 98(10):106803, 2007.

[23] Rahul Roy. Topological phases and the quantum spin hall effect in three dimensions. Physical Review B, 79(19):195322, 2009.

[24] Markus König, Steffen Wiedmann, Christoph Brüne, Andreas Roth, Hartmut Buhmann, Laurens W Molenkamp, Xiao-Liang Qi, and Shou-Cheng Zhang. Quantum spin hall insulator state in hgte quantum wells. Science, 318(5851):766–770, 2007.

[25] David Hsieh, Dong Qian, Lewis Wray, YuQi Xia, Yew San Hor, RJ Cava, and M Zahid Hasan. A topological dirac insulator in a quantum spin hall phase. Nature, 452(7190):970–974, 2008.

[26] M Hasan and C Kane. Colloquium: Topological insulators. Rev. Mod. Phys., 82(4):3045–3067, November 2010.

[27] Xiao-Liang Qi and Shou-Cheng Zhang. Topological insulators and superconductors. Reviews of Modern Physics, 83(4):1057, 2011.

[28] Alexei Kitaev, Vladimir Lebedev, and Mikhail Feigelman. Periodic table for topological insulators and superconductors. In AIP Conference Proceedings, volume 1134, pages 22–30. AIP, 2009.

[29] Shinsei Ryu, Andreas P Schnyder, Akira Furusaki, and Andreas WW Ludwig. Topological insulators and superconductors: tenfold way and dimensional hierarchy. New Journal of Physics, 12(6):065010, 2010.

[30] Zheng-Cheng Gu and Xiao-Gang Wen. Tensor-entanglement-filtering renormalization approach and symmetry-protected topological order. Phys. Rev. B, 80:155131, Oct 2009.

[31] Frank Pollmann, Ari M. Turner, Erez Berg, and Masaki Oshikawa. Entanglement spectrum of a topological phase in one dimension. Phys. Rev. B, 81:064439, Feb 2010.

[32] Lukasz Fidkowski and Alexei Kitaev. Topological phases of fermions in one dimension. Phys. Rev. B, 83:075103, Feb 2011.

[33] Ari M. Turner, Frank Pollmann, and Erez Berg. Topological phases of one-dimensional fermions: An entanglement point of view. Phys. Rev. B, 83:075102, Feb 2011.

[34] Xie Chen, Zheng-Cheng Gu, and Xiao-Gang Wen. Classification of gapped symmetric phases in one-dimensional spin systems. Phys. Rev. B, 83:035107, Jan 2011.

[35] Norbert Schuch, David Pérez-García, and Ignacio Cirac. Classifying quantum phases using matrix product states and projected entangled pair states. Phys. Rev. B, 84:165139, Oct 2011.

[36] Xie Chen, Zheng-Cheng Gu, Zheng-Xin Liu, and Xiao-Gang Wen. Symmetry protected topological orders and the group cohomology of their symmetry group. Phys. Rev. B, 87:155114, Apr 2013.

[37] Michael Levin and Zheng-Cheng Gu. Braiding statistics approach to symmetry-protected topological phases. Phys. Rev. B, 86:115109, Sep 2012.

[38] T Senthil. Symmetry-protected topological phases of quantum matter. Annu. Rev. Condens. Matter Phys., 6(1):299–324, 2015.

[39] Xiao-Gang Wen. Quantum orders and symmetric spin liquids. Phys. Rev. B, 65:165113, Apr 2002.

[40] Xiao-Gang Wen. Quantum order from string-net condensations and the origin of light and massless fermions. Phys. Rev. D, 68:065003, Sep 2003.

[41] Fa Wang and Ashvin Vishwanath. Spin-liquid states on the triangular and kagomé lattices: A projective-symmetry-group analysis of schwinger boson states. Phys. Rev. B, 74:174423, Nov 2006.

[42] Su-Peng Kou, Michael Levin, and Xiao-Gang Wen. Mutual chern-simons theory for Z_2 topological order. Phys. Rev. B, 78:155134, Oct 2008.

[43] Su-Peng Kou and Xiao-Gang Wen. Translation-symmetry-protected topological orders in quantum spin systems. Phys. Rev. B, 80:224406, Dec 2009.

[44] Yejin Huh, Matthias Punk, and Subir Sachdev. Vison states and confinement transitions of $\mathbb{Z}_2$ spin liquids on the kagome lattice. Phys. Rev. B, 84:094419, Sep 2011.

[45] Gang Chen, Andrew Essin, and Michael Hermele. Majorana spin liquids and projective realization of SU(2) spin symmetry. Phys. Rev. B, 85:094418, Mar 2012.

[46] Michael Levin and Ady Stern. Classification and analysis of two-dimensional abelian fractional topological insulators. Phys. Rev. B, 86:115131, Sep 2012.

[47] Gil Young Cho, Yuan-Ming Lu, and Joel E. Moore. Gapless edge states of background field theory and translation-symmetric $\mathbb{Z}_2$ spin liquids. Phys. Rev. B, 86:125101, Sep 2012.

[48] Yi-Ping Huang, Gang Chen, and Michael Hermele. Quantum spin ices and topological phases from dipolar-octupolar doublets on the pyrochlore lattice. Phys. Rev. Lett., 112:167203, Apr 2014.

[49] Yi-Ping Huang and Michael Hermele. Theory of quantum kagome ice and vison zero modes. Phys. Rev. B, 95:075130, Feb 2017.

[50] Juan Carrasquilla, Zhihao Hao, and Roger G Melko. A two-dimensional spin liquid in quantum kagome ice. Nature communications, 6, 2015.

[51] Jhih-An Yang, Yi-Ping Huang, Michael Hermele, Tongfei Qi, Gang Cao, and Dmitry Reznik. High-energy electronic excitations in Sr_2IrO_4 observed by Raman scattering. Phys. Rev. B, 91:195140, May 2015.

[52] William Witczak-Krempa, Gang Chen, Yong Baek Kim, and Leon Balents. Correlated quantum phenomena in the strong spin-orbit regime. Annu. Rev. Condens. Matter Phys., 5(1):57–82, 2014.

[53] Michael Hermele, Matthew P. A. Fisher, and Leon Balents. Pyrochlore photons: The U(1) spin liquid in a S=1/2 three-dimensional frustrated magnet. Phys. Rev. B, 69(6):064404, February 2004.

[54] M J P Gingras and P A McClarty. Quantum spin ice: a search for gapless quantum spin liquids in pyrochlore magnets. Reports on Progress in Physics, 77(5):056501, 2014.

[55] Dmytro Pesin and Leon Balents. Mott physics and band topology in materials with strong spin–orbit interaction. Nature Physics, 6(5):376–381, 2010.

[56] Xiangang Wan, Ari M. Turner, Ashvin Vishwanath, and Sergey Y. Savrasov. Topological semimetal and fermi-arc surface states in the electronic structure of pyrochlore iridates. Phys. Rev. B, 83:205101, May 2011.

[57] Mehdi Kargarian, Jun Wen, and Gregory A. Fiete. Competing exotic topological insulator phases in transition-metal oxides on the pyrochlore lattice with distortion. Phys. Rev. B, 83:165112, Apr 2011.

[58] Gang Chen and Michael Hermele. Magnetic orders and topological phases from f-d exchange in pyrochlore iridates. Phys. Rev. B, 86:235129, Dec 2012.

[59] William Witczak-Krempa and Yong Baek Kim. Topological and magnetic phases of interacting electrons in the pyrochlore iridates. Phys. Rev. B, 85:045124, Jan 2012.

[60] William Witczak-Krempa, Ara Go, and Yong Baek Kim. Pyrochlore electrons under pressure, heat, and field: Shedding light on the iridates. Phys. Rev. B, 87:155101, Apr 2013.

[61] Gang Chen and Leon Balents. Spin-orbit effects in $Na_4Ir_3O_8$: A hyper-kagome lattice antiferromagnet. Phys. Rev. B, 78(9):094403, September 2008.

[62] Yi Zhou, Patrick A. Lee, Tai-Kai Ng, and Fu-Chun Zhang. $Na_4Ir_3O_8$ as a 3D Spin Liquid with Fermionic Spinons. Phys. Rev. Lett., 101:197201, Nov 2008.

[63] Michael J. Lawler, Hae-Young Kee, Yong Baek Kim, and Ashvin Vishwanath. Topological Spin Liquid on the Hyperkagome Lattice of $Na_4Ir_3O_8$. Phys. Rev. Lett., 100:227201, Jun 2008.

[64] Michael J. Lawler, Arun Paramekanti, Yong Baek Kim, and Leon Balents. Gapless Spin Liquids on the Three-Dimensional Hyperkagome Lattice of $Na_4Ir_3O_8$. Phys. Rev. Lett., 101:197202, Nov 2008.

[65] E. J. Bergholtz, A. M. Läuchli, and R. Moessner. Symmetry Breaking on the Three-Dimensional Hyperkagome Lattice of $Na_4Ir_3O_8$. Phys. Rev. Lett., 105:237202, Dec 2010.

[66] Gang Chen and Yong Baek Kim. Anomalous enhancement of the Wilson ratio in a quantum spin liquid: The case of $Na_4Ir_3O_8$. Phys. Rev. B, 87:165120, Apr 2013.

[67] J. Chaloupka, George Jackeli, and Giniyat Khaliullin. Kitaev-Heisenberg Model on a Honeycomb Lattice: Possible Exotic Phases in Iridium Oxides A_2IrO_3. Phys. Rev. Lett., 105:027204, Jul 2010.

[68] Itamar Kimchi, James G. Analytis, and Ashvin Vishwanath. Three-dimensional quantum spin liquids in models of harmonic-honeycomb iridates and phase diagram in an infinite-d approximation. Phys. Rev. B, 90:205126, Nov 2014.

[69] Eric Kin-Ho Lee, Robert Schaffer, Subhro Bhattacharjee, and Yong Baek Kim. Heisenberg-kitaev model on the hyperhoneycomb lattice. Phys. Rev. B, 89:045117, Jan 2014.

[70] Hamid R. Molavian, Michel J. P. Gingras, and Benjamin Canals. Dynamically Induced Frustration as a Route to a Quantum Spin Ice State in $Tb_2Ti_2O_7$ via Virtual Crystal Field Excitations and Quantum Many-Body Effects. Phys. Rev. Lett., 98:157204, Apr 2007.

[71] Shigeki Onoda and Yoichi Tanaka. Quantum fluctuations in the effective pseudospin-$\frac{1}{2}$ model for magnetic pyrochlore oxides. Phys. Rev. B, 83:094411, Mar 2011.

[72] Lucile Savary and Leon Balents. Coulombic Quantum Liquids in Spin-1/2 Pyrochlores. Phys. Rev. Lett., 108(3):037202, January 2012.

[73] SungBin Lee, Shigeki Onoda, and Leon Balents. Generic quantum spin ice. Phys. Rev. B, 86:104412, Sep 2012.

[74] R. Applegate, N. R. Hayre, R. R. P. Singh, T. Lin, A. G. R. Day, and M. J. P. Gingras. Vindication of $Yb_2Ti_2O_7$ as a Model Exchange Quantum Spin Ice. Phys. Rev. Lett., 109:097205, Aug 2012.

[75] A. Abragam and B. Bleaney. Electron Paramagnetic Resonance of Transition Ions (Oxford Classic Texts in the Physical Sciences). Oxford University Press, USA, reprint edition, 7 1970.

[76] George Jackeli and Giniyat Khaliullin. Magnetically Hidden Order of Kramers Doublets in d^1 Systems: Sr_2VO_4. Phys. Rev. Lett., 103:067205, Aug 2009.

[77] Gang Chen, Rodrigo Pereira, and Leon Balents. Exotic phases induced by strong spin-orbit coupling in ordered double perovskites. Phys. Rev. B, 82(17):174440, November 2010.

[78] B. J. Kim, Hosub Jin, S. J. Moon, J.-Y. Kim, B.-G. Park, C. S. Leem, Jaejun Yu, T. W. Noh, C. Kim, S.-J. Oh, J.-H. Park, V. Durairaj, G. Cao, and E. Rotenberg. Novel $J_{\text{eff}} = 1/2$ Mott State Induced by Relativistic Spin-Orbit Coupling in Sr_2IrO_4. Phys. Rev. Lett., 101:076402, Aug 2008.

[79] B. J. Kim, H. Ohsumi, T. Komesu, S. Sakai, T. Morita, H. Takagi, and T. Arima. Phase-Sensitive Observation of a Spin-Orbital Mott State in Sr_2IrO_4. Science, 323(5919):1329–1332, 2009.

[80] Gang Chen and Leon Balents. Spin-orbit coupling in d^2 ordered double perovskites. Phys. Rev. B, 84:094420, Sep 2011.

[81] George F Koster, John O Dimmock, Robert G Wheeler, and Hermann Statz. The Properties of the Thirty-Two Point Groups (Research Monograph). The MIT Press, 1963.

[82] Jason S. Gardner, Michel J. P. Gingras, and John E. Greedan. Magnetic pyrochlore oxides. Rev. Mod. Phys., 82:53–107, Jan 2010.

[83] M Watahiki, K Tomiyasu, K Matsuhira, K Iwasa, M Yokoyama, S Takagi, M Wakeshima, and Y Hinatsu. Crystalline electric field study in the pyrochlore $Nd_2Ir_2O_7$ with metal-insulator transition. Journal of Physics: Conference Series, 320(1):012080, 2011.

[84] A Bertin, Y Chapuis, P Dalmas de Réotier, and A Yaouanc. Crystal electric field in the $R_2Ti_2O_7$ pyrochlore compounds. Journal of Physics: Condensed Matter, 24(25):256003, 2012.

[85] S. H. Curnoe. Structural distortion and the spin liquid state in $Tb_2Ti_2O_7$. Phys. Rev. B, 78:094418, Sep 2008.

[86] M Kurita, Y Yamaji, and M Imada. Topological Insulators from Spontaneous Symmetry Breaking Induced by Electron Correlation on Pyrochlore Lattices. J. Phys. Soc. Jpn., 80(044708):044708, 2011.

[87] F. Burnell, Shoibal Chakravarty, and S. Sondhi. Monopole flux state on the pyrochlore lattice. Phys. Rev. B, 79(14):144432, April 2009.

[88] Argha Banerjee, Sergei Isakov, Kedar Damle, and Yong Kim. Unusual Liquid State of Hard-Core Bosons on the Pyrochlore Lattice. Phys. Rev. Lett., 100(4):047208, January 2008.

[89] H. W. J. Blöte, R. F. Wielinga, and W. J. Huiskamp. Heat-capacity measurements on rare-earth double oxides $R_2M_2O_7$. Physica, 43:549, 1969.

[90] Kazuyuki Matsuhira, Yukio Hinatsu, Kenichi Tenya, Hiroshi Amitsuka, and Toshiro Sakakibara. Low-temperature magnetic properties of pyrochlore stannates. Journal of the Physical Society of Japan, 71(6):1576, 2002.

[91] M. A. Subramanian, G. Aravamudan, and G. V. Subba Rao. Oxide pyrochlores – a review. Prog. Solid St. Chem., 15:55, 1983.

[92] Kate Ross, Lucile Savary, Bruce Gaulin, and Leon Balents. Quantum Excitations in Quantum Spin Ice. Phys. Rev. X, 1(2):021002, October 2011.

[93] J. Lago, I. Živković, B. Z. Malkin, J. Rodriguez Fernandez, P. Ghigna, P. Dalmas de Réotier, A. Yaouanc, and T. Rojo. $CdEr_2Se_4$: A New Erbium Spin Ice System in a Spinel Structure. Phys. Rev. Lett., 104:247203, Jun 2010.

[94] Akihiro Koda, Ryosuke Kadono, Kazuki Ohishi, Shanta R. Saha, Wataru Higemoto, Shigeki Yonezawa, Yuji Muraoka, and Zenji Hiroi. Anomalous Magnetic Phase in an Undistorted Pyrochlore Oxide $Cd_2Os_2O_7$ Induced by Geometrical Frustration. Journal of the Physical Society of Japan, 76(6):063703, 2007.

[95] J. Yamaura, K. Ohgushi, H. Ohsumi, T. Hasegawa, I. Yamauchi, K. Sugimoto, S. Takeshita, A. Tokuda, M. Takata, M. Udagawa, M. Takigawa, H. Harima, T. Arima, and Z. Hiroi. Tetrahedral Magnetic Order and the Metal-Insulator Transition in the Pyrochlore Lattice of $Cd_2Os_2O_7$. Phys. Rev. Lett., 108:247205, Jun 2012.

[96] Nikolay A. Bogdanov, Rémi Maurice, Ioannis Rousochatzakis, Jeroen van den Brink, and Liviu Hozoi. Magnetic State of Pyrochlore $Cd_2Os_2O_7$ Emerging from Strong Competition of Ligand Distortions and Longer-Range Crystalline Anisotropy. Phys. Rev. Lett., 110(12):127206, March 2013.

[97] D. Singh, P. Blaha, K. Schwarz, and J. Sofo. Electronic structure of the pyrochlore metals $Cd_2Os_2O_7$ and $Cd_2Re_2O_7$. Phys. Rev. B, 65(15):155109, March 2002.

[98] Hiroshi Shinaoka, Takashi Miyake, and Shoji Ishibashi. Noncollinear Magnetism and Spin-Orbit Coupling in $5d$ Pyrochlore Oxide $Cd_2Os_2O_7$. Phys. Rev. Lett., 108:247204, Jun 2012.

[99] Yi-Ping Huang and Michael Hermele. unpublished.

[100] Liang Fu and C. L. Kane. Topological insulators with inversion symmetry. Phys. Rev. B, 76:045302, Jul 2007.

[101] P. W. Anderson. Resonating valence bonds: A new kind of insulator? Mat. Res. Bull., 8:153, 1973.

[102] P. W. Anderson. The Resonating Valence Bond State in La_2CuO_4 and Superconductivity. Science, 235:1196, 1987.

[103] Mingxuan Fu, Takashi Imai, Tian-Heng Han, and Young S Lee. Evidence for a gapped spin-liquid ground state in a kagome heisenberg antiferromagnet. Science, 350(6261):655–658, 2015.

[104] Tian-Heng Han, M. R. Norman, J.-J. Wen, Jose A. Rodriguez-Rivera, Joel S. Helton, Collin Broholm, and Young S. Lee. Correlated impurities and intrinsic spin-liquid physics in the kagome material herbertsmithite. Phys. Rev. B, 94:060409, Aug 2016.

[105] M. R. Norman. *Colloquium* : Herbertsmithite and the search for the quantum spin liquid. Rev. Mod. Phys., 88:041002, Dec 2016.

[106] Philippe Mendels and Fabrice Bert. Quantum kagome frustrated antiferromagnets: One route to quantum spin liquids. Comptes Rendus Physique, 17(3–4):455 – 470, 2016. Physique de la matière condensée au {XXIe} siècle: l'héritage de Jacques Friedel.

[107] N. Read and B. Chakraborty. Statistics of the excitations of the resonating-valence-bond state. Phys. Rev. B, 40:7133–7140, Oct 1989.

[108] N. Read and Subir Sachdev. Large-N expansion for frustrated quantum antiferromagnets. Phys. Rev. Lett., 66:1773–1776, Apr 1991.

[109] X. G. Wen. Mean-field theory of spin-liquid states with finite energy gap and topological orders. Phys. Rev. B, 44:2664–2672, Aug 1991.

[110] Leon Balents, Matthew P. A. Fisher, and Chetan Nayak. Dual order parameter for the nodal liquid. Phys. Rev. B, 60:1654–1667, Jul 1999.

[111] T. Senthil and Matthew P. A. Fisher. Z_2 gauge theory of electron fractionalization in strongly correlated systems. Phys. Rev. B, 62:7850–7881, Sep 2000.

[112] R. Moessner and S. L. Sondhi. Resonating valence bond phase in the triangular lattice quantum dimer model. Phys. Rev. Lett., 86:1881–1884, Feb 2001.

[113] R. Moessner, S. L. Sondhi, and Eduardo Fradkin. Short-ranged resonating valence bond physics, quantum dimer models, and ising gauge theories. Phys. Rev. B, 65:024504, Dec 2001.

[114] L. Balents, M. P. A. Fisher, and S. M. Girvin. Fractionalization in an easy-axis kagome antiferromagnet. Phys. Rev. B, 65:224412, May 2002.

[115] A. Yu. Kitaev. Fault-tolerant quantum computation by anyons. Ann. Phys., 303:2, 2003.

[116] Simeng Yan, David A Huse, and Steven R White. Spin-liquid ground state of the s= 1/2 kagome heisenberg antiferromagnet. Science, 332(6034):1173–1176, 2011.

[117] Stefan Depenbrock, Ian P. McCulloch, and Ulrich Schollwöck. Nature of the spin-liquid ground state of the $s = 1/2$ heisenberg model on the kagome lattice. Phys. Rev. Lett., 109:067201, Aug 2012.

[118] H.-C. Jiang, Z. Wang, and L. Balents. Identifying topological order by entanglement entropy. Nat. Phys., 8:902, 2012.

[119] J. W. Mei, J. Y. Chen, H. He, and X. G. Wen. Gapped spin liquid with Z_2-topological order for kagome Heisenberg model. 2016.

[120] Yasir Iqbal, Federico Becca, and Didier Poilblanc. Projected wave function study of $\mathbb{Z}_2$ spin liquids on the kagome lattice for the spin-$\frac{1}{2}$ quantum Heisenberg antiferromagnet. Phys. Rev. B, 84:020407, Jul 2011.

[121] Yasir Iqbal, Federico Becca, Sandro Sorella, and Didier Poilblanc. Gapless spin-liquid phase in the kagome spin-$\frac{1}{2}$ heisenberg antiferromagnet. Phys. Rev. B, 87:060405, Feb 2013.

[122] Yasir Iqbal, Didier Poilblanc, and Federico Becca. Vanishing spin gap in a competing spin-liquid phase in the kagome heisenberg antiferromagnet. Phys. Rev. B, 89:020407, Jan 2014.

[123] H. J. Liao, Z. Y. Xie, J. Chen, Z. Y. Liu, H. D. Xie, R. Z. Huang, B. Normand, and T. Xiang. Gapless spin-liquid ground state in the s=1/2 kagome antiferromagnet. 2016.

[124] Yin-Chen He, D. N. Sheng, and Yan Chen. Chiral spin liquid in a frustrated anisotropic kagome heisenberg model. Phys. Rev. Lett., 112:137202, Apr 2014.

[125] Shou-Shu Gong, Wei Zhu, and D. N. Sheng. Emergent chiral spin liquid: Fractional quantum hall effect in a kagome heisenberg model. Scientific Reports, 4:6317, 2014.

[126] Shou-Shu Gong, Wei Zhu, Leon Balents, and D. N. Sheng. Global phase diagram of competing ordered and quantum spin-liquid phases on the kagome lattice. Phys. Rev. B, 91:075112, Feb 2015.

[127] Zhenyue Zhu and Steven R. White. Spin liquid phase of the $s = \frac{1}{2}$ $J_1 - J_2$ heisenberg model on the triangular lattice. Phys. Rev. B, 92:041105, Jul 2015.

[128] Wen-Jun Hu, Shou-Shu Gong, Wei Zhu, and D. N. Sheng. Competing spin-liquid states in the spin-$\frac{1}{2}$ heisenberg model on the triangular lattice. Phys. Rev. B, 92:140403, Oct 2015.

[129] Yasir Iqbal, Wen-Jun Hu, Ronny Thomale, Didier Poilblanc, and Federico Becca. Spin liquid nature in the heisenberg $J_1 - J_2$ triangular antiferromagnet. Phys. Rev. B, 93:144411, Apr 2016.

[130] R. Moessner, S. L. Sondhi, and P. Chandra. Phase diagram of the hexagonal lattice quantum dimer model. Phys. Rev. B, 64:144416, Sep 2001.

[131] M. Ciomaga Hatnean, M. R. Lees, O. A. Petrenko, D. S. Keeble, G. Balakrishnan, M. J. Gutmann, V. V. Klekovkina, and B. Z. Malkin. Structural and magnetic investigations of single-crystalline neodymium zirconate pyrochlore $Nd_2Zr_2O_7$. Phys. Rev. B, 91:174416, May 2015.

[132] E. Lhotel, S. Petit, S. Guitteny, O. Florea, M. Ciomaga Hatnean, C. Colin, E. Ressouche, M. R. Lees, and G. Balakrishnan. Fluctuations and All-In˘All-Out Ordering in Dipole-Octupole $Nd_2Zr_2O_7$. Phys. Rev. Lett., 115:197202, Nov 2015.

[133] J. Xu, V. K. Anand, A. K. Bera, M. Frontzek, D. L. Abernathy, N. Casati, K. Siemensmeyer, and B. Lake. Magnetic structure and crystal-field states of the pyrochlore antiferromagnet $Nd_2Zr_2O_7$. Phys. Rev. B, 92:224430, Dec 2015.

[134] K Matsuhira, Z Hiroi, T Tayama, S Takagi, and T Sakakibara. A new macroscopically degenerate ground state in the spin ice compound Dy_2 Ti_2 O_7 under a magnetic field. Journal of Physics: Condensed Matter, 14(29):L559, 2002.

[135] A. S. Wills, R. Ballou, and C. Lacroix. Model of localized highly frustrated ferromagnetism: The *kagomé* spin ice. Phys. Rev. B, 66:144407, Oct 2002.

[136] R. Moessner and S. L. Sondhi. Theory of the [111] magnetization plateau in spin ice. Phys. Rev. B, 68:064411, Aug 2003.

[137] Zenji Hiroi, Kazuyuki Matsuhira, Seishi Takagi, Takashi Tayama, and Toshio Sakakibara. Specific heat of kagome ice in the pyrochlore oxide $Dy_2Ti_2O_7$. Journal of the Physical Society of Japan, 72(2):411–418, 2003.

[138] T. Sakakibara, T. Tayama, Z. Hiroi, K. Matsuhira, and S. Takagi. Observation of a Liquid-Gas-Type Transition in the Pyrochlore Spin Ice Compound $Dy_2Ti_2O_7$ in a Magnetic Field. Phys. Rev. Lett., 90:207205, May 2003.

[139] S. V. Isakov, K. S. Raman, R. Moessner, and S. L. Sondhi. Magnetization curve of spin ice in a [111] magnetic field. Phys. Rev. B, 70:104418, Sep 2004.

[140] Y. Tabata, H. Kadowaki, K. Matsuhira, Z. Hiroi, N. Aso, E. Ressouche, and B. Fåk. Kagomé Ice State in the Dipolar Spin Ice $Dy_2Ti_2O_7$. Phys. Rev. Lett., 97:257205, Dec 2006.

[141] Andrew J Macdonald, Peter C W Holdsworth, and Roger G Melko. Classical topological order in kagome ice. Journal of Physics: Condensed Matter, 23(16):164208, 2011.

[142] P. Nikolić and T. Senthil. Theory of the kagome lattice ising antiferromagnet in weak transverse fields. Phys. Rev. B, 71:024401, Jan 2005.

[143] Elliott Lieb, Theodore Schultz, and Daniel Mattis. Two soluble models of an antiferromagnetic chain. Annals of Physics, 16(3):407 – 466, 1961.

[144] Masaki Oshikawa. Commensurability, excitation gap, and topology in quantum many-particle systems on a periodic lattice. Phys. Rev. Lett., 84:1535–1538, Feb 2000.

[145] M. B. Hastings. Lieb-schultz-mattis in higher dimensions. Phys. Rev. B, 69:104431, Mar 2004.

[146] Gang Chen. in preparation.

[147] Eduardo Fradkin and Stephen H. Shenker. Phase diagrams of lattice gauge theories with higgs fields. Phys. Rev. D, 19:3682–3697, Jun 1979.

[148] Arun Paramekanti and Ashvin Vishwanath. Extending luttinger's theorem to Z_2 fractionalized phases of matter. Phys. Rev. B, 70:245118, Dec 2004.

[149] Andrew M. Essin and Michael Hermele. Classifying fractionalization: Symmetry classification of gapped $\mathbb{Z}_2$ spin liquids in two dimensions. Phys. Rev. B, 87:104406, Mar 2013.

[150] Xie Chen, F. J. Burnell, Ashvin Vishwanath, and Lukasz Fidkowski. Anomalous symmetry fractionalization and surface topological order. Phys. Rev. X, 5:041013, Oct 2015.

[151] Xie Chen. Symmetry fractionalization in two dimensional topological phases. 2016.

[152] Andrej Mesaros and Ying Ran. Classification of symmetry enriched topological phases with exactly solvable models. Phys. Rev. B, 87:155115, Apr 2013.

[153] Ling-Yan Hung and Xiao-Gang Wen. Quantized topological terms in weak-coupling gauge theories with a global symmetry and their connection to symmetry-enriched topological phases. Phys. Rev. B, 87:165107, Apr 2013.

[154] Meng Cheng, Michael Zaletel, Maissam Barkeshli, Ashvin Vishwanath, and Parsa Bonderson. Translational symmetry and microscopic constraints on symmetry-enriched topological phases: A view from the surface. Phys. Rev. X, 6:041068, Dec 2016.

[155] Hao Song, Sheng-Jie Huang, Liang Fu, and Michael Hermele. Topological phases protected by point group symmetry. Phys. Rev. X, 7:011020, Feb 2017.

[156] M. Hermele. unpublished.

[157] Xiao-Gang Wen. Quantum order: a quantum entanglement of many particles. Physics Letters A, 300:175 – 181, 2002.

[158] X.-G. Wen. Quantum Field Theory of Many-Body Systems. Oxford University Press, 2004.

[159] Andrew M. Essin and Michael Hermele. Spectroscopic signatures of crystal momentum fractionalization. Phys. Rev. B, 90:121102, Sep 2014.

[160] Ching-Yu Huang, Xie Chen, and Frank Pollmann. Detection of symmetry-enriched topological phases. Phys. Rev. B, 90:045142, Jul 2014.

[161] Michael Zaletel, Yuan-Ming Lu, and Ashvin Vishwanath. Measuring space-group symmetry fractionalization in Z_2 spin liquids. 2015.

[162] F.D.M. Haldane. Continuum dynamics of the 1-D Heisenberg antiferromagnet: Identification with the O(3) nonlinear sigma model. Physics Letters A, 93(9):464 – 468, 1983.

[163] F. D. M. Haldane. Nonlinear field theory of large-spin heisenberg antiferromagnets: Semiclassically quantized solitons of the one-dimensional easy-axis néel state. Phys. Rev. Lett., 50:1153–1156, Apr 1983.

[164] R. Moessner and S. L. Sondhi. Ising models of quantum frustration. Phys. Rev. B, 63:224401, May 2001.

[165] Cenke Xu and Leon Balents. Quantum phase transitions around the staggered valence-bond solid. Phys. Rev. B, 84:014402, Jul 2011.

[166] Jie Lou, Anders W. Sandvik, and Leon Balents. Emergence of U(1) Symmetry in the 3D XY Model with Z_q Anisotropy. Phys. Rev. Lett., 99:207203, Nov 2007.

[167] Hao Song and Michael Hermele. Space-group symmetry fractionalization in a family of exactly solvable models with Z_2 topological order. Phys. Rev. B, 91:014405, Jan 2015.

[168] Masatoshi Imada, Atsushi Fujimori, and Yoshinori Tokura. Metal-insulator transitions. Rev. Mod. Phys., 70:1039–1263, Oct 1998.

[169] Patrick A. Lee, Naoto Nagaosa, and Xiao-Gang Wen. Doping a mott insulator: Physics of high-temperature superconductivity. Rev. Mod. Phys., 78:17–85, Jan 2006.

[170] Alexander Cyril Hewson. The Kondo problem to heavy fermions, volume 2. Cambridge university press, 1997.

[171] Fa Wang and T Senthil. Twisted Hubbard model for Sr_2IrO_4: Magnetism and possible high temperature superconductivity. Phys. Rev. Lett., 106(13):136402, 2011.

[172] D. Salamon, Ran Liu, M. V. Klein, M. A. Karlow, S. L. Cooper, S-W. Cheong, W. C. Lee, and D. M. Ginsberg. Large-shift raman scattering in insulating parent compounds of cuprate superconductors. Phys. Rev. B, 51:6617–6633, Mar 1995.

[173] Feng Ye, Songxue Chi, Bryan C. Chakoumakos, Jaime A. Fernandez-Baca, Tongfei Qi, and G. Cao. Magnetic and crystal structures of Sr_2IrO_4: A neutron diffraction study. Phys. Rev. B, 87:140406, Apr 2013.

[174] D. Haskel, G. Fabbris, Mikhail Zhernenkov, P. P. Kong, C. Q. Jin, G. Cao, and M. van Veenendaal. Pressure Tuning of the Spin-Orbit Coupled Ground State in Sr_2IrO_4. Phys. Rev. Lett., 109:027204, Jul 2012.

[175] S. J. Moon, M. W. Kim, K. W. Kim, Y. S. Lee, J.-Y. Kim, J.-H. Park, B. J. Kim, S.-J. Oh, S. Nakatsuji, Y. Maeno, I. Nagai, S. I. Ikeda, G. Cao, and T. W. Noh. Electronic structures of layered perovskite Sr_2MO_4 (M = Ru, Rh, and Ir). Phys. Rev. B, 74:113104, Sep 2006.

[176] Jungho Kim, M Daghofer, AH Said, T Gog, J van den Brink, G Khaliullin, and BJ Kim. Excitonic quasiparticles in a spin–orbit mott insulator. Nature Communications, 5, 2014.

[177] Thomas P. Devereaux and Rudi Hackl. Inelastic light scattering from correlated electrons. Rev. Mod. Phys., 79:175–233, Jan 2007.

[178] X. Liu, Vamshi M. Katukuri, L. Hozoi, Wei-Guo Yin, M. P. M. Dean, M. H. Upton, Jungho Kim, D. Casa, A. Said, T. Gog, T. F. Qi, G. Cao, A. M. Tsvelik, Jeroen van den Brink, and J. P. Hill. Testing the Validity of the Strong Spin-Orbit-Coupling Limit for Octahedrally Coordinated Iridate Compounds in a Model System Sr_3CuIrO_6. Phys. Rev. Lett., 109:157401, Oct 2012.

[179] Luuk J. P. Ament, Giniyat Khaliullin, and Jeroen van den Brink. Theory of resonant inelastic x-ray scattering in iridium oxide compounds: Probing spin-orbit-entangled ground states and excitations. Phys. Rev. B, 84:020403, Jul 2011.

[180] Kenya Ohgushi, Jun-ichi Yamaura, Hiroyuki Ohsumi, Kunihisa Sugimoto, Soshi Takeshita, Akihisa Tokuda, Hidenori Takagi, Masaki Takata, and Taka-hisa Arima. Resonant X-ray Diffraction Study of the Strongly Spin-Orbit-Coupled Mott Insulator $CaIrO_3$. Phys. Rev. Lett., 110:217212, May 2013.

[181] S Boseggia, H C Walker, J Vale, R Springell, Z Feng, R S Perry, M Moretti Sala, H M Rønnow, S P Collins, and D F McMorrow. Locking of iridium magnetic moments to the correlated rotation of oxygen octahedra in Sr_2IrO_4 revealed by x-ray resonant scattering. Journal of Physics: Condensed Matter, 25(42):422202, 2013.

[182] Chetan Dhital, Tom Hogan, Z. Yamani, Clarina de la Cruz, Xiang Chen, Sovit Khadka, Zhensong Ren, and Stephen D. Wilson. Neutron scattering study of correlated phase behavior in Sr_2IrO_4. Phys. Rev. B, 87:144405, Apr 2013.

[183] Feng Ye, Songxue Chi, Bryan C. Chakoumakos, Jaime A. Fernandez-Baca, Tongfei Qi, and G. Cao. Magnetic and crystal structures of Sr_2IrO_4: A neutron diffraction study. Phys. Rev. B, 87:140406, Apr 2013.

Appendix A

Cross section of Raman scattering

Let incident/scattering light denoted by $(\boldsymbol{q}_i, \omega_i, \boldsymbol{e}_{\boldsymbol{q}_i})$ and $(\boldsymbol{q}_s, \omega_s, \boldsymbol{e}_{\boldsymbol{q}_s})$. The Hamiltonian is written as

$$\begin{aligned} H &= \sum_{i=1}^{N} \frac{(\boldsymbol{p}_i + (e/c)\boldsymbol{A}(\boldsymbol{r}_i))^2}{2m} + H_{Coulomb} + H_{fields} \\ &= \left[\sum_i \frac{\boldsymbol{p}_i^2}{2m} + H_{Coulomb}\right] + H_{fields} + H_{int} \\ &= H_0 + H_{fields} + H_{int}. \end{aligned} \tag{A.1}$$

Here, e is the magnitude of electron charge. H_0 describe the system we want to probe without light which satisfied $H_0|\alpha\rangle = E_\alpha|\alpha\rangle$. Here, α can be a combination of band index, wave vector, orbital, spin qunatum numbers depends on how Coulomb interaction is included into H_0. H_{fields} describe the free electromagnetic wave. H_{int} describe how light is coupled to the system we want to probe.

$$H_{int} = \frac{e}{2mc}\sum_i [\boldsymbol{p}_i \cdot \boldsymbol{A}(\boldsymbol{r}_i) + \boldsymbol{A}(\boldsymbol{r}_i) \cdot \boldsymbol{p}_i] + \frac{e^2}{2mc^2}\sum_i \boldsymbol{A}(\boldsymbol{r}_i) \cdot \boldsymbol{A}(\boldsymbol{r}_i) = H_1 + H_2 \tag{A.2}$$

Here H_1 denote the part with linear dependence of $\boldsymbol{A}$ and H_2 denote the part with quadratic dependence of $\boldsymbol{A}$. Now, we quantize the vector potential with transverse gauge as usual

$$\boldsymbol{A}(\boldsymbol{r}_i) = \sqrt{\frac{1}{V}}\sum_{\boldsymbol{k}} \left[e^{i\boldsymbol{k}\cdot\boldsymbol{r}_i}\boldsymbol{A}_{\boldsymbol{k}}(t) + c.c.\right]. \tag{A.3}$$

Since $\boldsymbol{A}(\boldsymbol{r}_i)$ is real, we need the second term. Then, replace the Fourier component by

$$\boldsymbol{A}_{\boldsymbol{k}}(t) \to \sqrt{\frac{\hbar c}{2|\boldsymbol{k}|}}\boldsymbol{a}_{\boldsymbol{k}}(t); \boldsymbol{a}_{\boldsymbol{k}}(t) = \sum_\eta a_{k\eta}\boldsymbol{\epsilon}_{k\eta} \tag{A.4}$$

$a^\dagger_{k\eta}, a_{k\eta}$ are creation and annihilation operators of transversal photon with momentum value k and polarization direction denoted by real unit vector $\boldsymbol{\epsilon}_{k\eta}$. The quantized vector potential and electric field is

$$\begin{aligned}
\boldsymbol{A}(\boldsymbol{r}_i) &= \sum_{\boldsymbol{k}} \sqrt{\frac{\hbar c}{2V|\boldsymbol{k}|}} \left[e^{i\boldsymbol{k}\cdot\boldsymbol{r}_i} \boldsymbol{a}_{\boldsymbol{k}}(t) + h.c. \right] \\
\boldsymbol{E}(\boldsymbol{r}_i) &= -\frac{1}{c}\frac{\partial \boldsymbol{A}(\boldsymbol{r}_i)}{\partial t} = \sum_{\boldsymbol{k}} \sqrt{\frac{\hbar c}{2V|\boldsymbol{k}|}} (ik) \left[e^{i\boldsymbol{k}\cdot\boldsymbol{r}_i} \boldsymbol{a}_{\boldsymbol{k}}(t) - e^{-i\boldsymbol{k}\cdot\boldsymbol{r}_i} \boldsymbol{a}^\dagger_{\boldsymbol{k}}(t) \right]. \qquad \text{(A.5)}
\end{aligned}$$

From above expression, we can see that H_1 and H_2 corresponds to the process that system is coupled to one photon and two photons cases.

In order to construct the general expression, we would like to write H_{int} in second quantization form.

$$\begin{aligned}
H_1 &= \frac{e}{mc} \sum_i \sum_{\boldsymbol{k},\eta} \sqrt{\frac{\hbar c}{2Vk}} \left[(\boldsymbol{p}_i \cdot \boldsymbol{\epsilon}_{k\eta}) \, e^{i\boldsymbol{k}\cdot\boldsymbol{r}_i} a_{k\eta} + h.c. \right] \\
&= \frac{e}{mc} \sum_{\boldsymbol{k},\eta} \sqrt{\frac{\hbar c}{2Vk}} \left[\left(\sum_{\alpha,\beta} \langle \alpha | (\boldsymbol{p} \cdot \boldsymbol{\epsilon}_{k\eta}) e^{i\boldsymbol{k}\cdot\boldsymbol{r}} | \beta \rangle c^\dagger_\alpha c_\beta \right) a_{k\eta} + h.c. \right] \qquad \text{(A.6)}
\end{aligned}$$

$$\begin{aligned}
H_2 &= \frac{e^2}{2mc^2} \sum_i \frac{1}{V} \sum_{\boldsymbol{k}\eta,\boldsymbol{k}'\eta'} \left[\left(e^{i\boldsymbol{k}\cdot\boldsymbol{r}_i} \sqrt{\frac{\hbar c}{2k}} a_{k\eta} + h.c. \right) \boldsymbol{\epsilon}_{k\eta} \cdot \left(e^{i\boldsymbol{k}'\cdot\boldsymbol{r}_i} \sqrt{\frac{\hbar c}{2k'}} a_{k'\eta'} + h.c. \right) \boldsymbol{\epsilon}_{k'\eta'} \right] \\
&= \frac{e^2}{2mc^2} \frac{1}{V} \sum_i \sum_{\substack{\boldsymbol{k}\eta \\ \boldsymbol{k}'\eta'}} \frac{\hbar c}{2\sqrt{kk'}} \Big[\left(e^{i(\boldsymbol{k}+\boldsymbol{k}')\cdot\boldsymbol{r}_i} a_{k\eta} a_{k'\eta'} \right) + \left(e^{-i(\boldsymbol{k}+\boldsymbol{k}')\cdot\boldsymbol{r}_i} a^\dagger_{k\eta} a^\dagger_{k'\eta'} \right) \\
&\quad + \left(e^{i(\boldsymbol{k}-\boldsymbol{k}')\cdot\boldsymbol{r}_i} a_{k\eta} a^\dagger_{k'\eta'} \right) + \left(e^{-i(\boldsymbol{k}-\boldsymbol{k}')\cdot\boldsymbol{r}_i} a^\dagger_{k\eta} a_{k'\eta'} \right) \Big] (\boldsymbol{\epsilon}_{k\eta} \cdot \boldsymbol{\epsilon}_{k'\eta'}) \\
&= \frac{e^2}{2mc^2} \frac{\hbar c}{2V} \sum_{\substack{\boldsymbol{k}\eta \\ \boldsymbol{k}'\eta'}} \frac{\boldsymbol{\epsilon}_{k\eta} \cdot \boldsymbol{\epsilon}_{k'\eta'}}{\sqrt{kk'}} \Big[\sum_{\alpha\beta} \langle \alpha | e^{i(\boldsymbol{k}+\boldsymbol{k}')\cdot\boldsymbol{r}} | \beta \rangle c^\dagger_\alpha c_\beta a_{k\eta} a_{k'\eta'} + \langle \alpha | e^{-i(\boldsymbol{k}+\boldsymbol{k}')\cdot\boldsymbol{r}} | \beta \rangle c^\dagger_\alpha c_\beta a^\dagger_{k\eta} a^\dagger_{k'\eta'} \\
&\quad + \langle \alpha | e^{i(\boldsymbol{k}-\boldsymbol{k}')\cdot\boldsymbol{r}} | \beta \rangle c^\dagger_\alpha c_\beta a_{k\eta} a^\dagger_{k'\eta'} + \langle \alpha | e^{-i(\boldsymbol{k}-\boldsymbol{k}')\cdot\boldsymbol{r}} | \beta \rangle c^\dagger_\alpha c_\beta a^\dagger_{k\eta} a_{k'\eta'} \Big] \qquad \text{(A.7)}
\end{aligned}$$

When $\boldsymbol{k} \cdot \boldsymbol{r}_i \ll 1$, which means electron is bounded in a range $\sim a^3$. The above exponent can

be expanded in term of power series.

$$\begin{aligned} H_1 \quad &\sim \frac{e}{mc}\sum_{\boldsymbol{k},\eta}\sqrt{\frac{\hbar c}{2Vk}}\left[\left(\sum_{\alpha,\beta}\langle\alpha|(\boldsymbol{p}\cdot\boldsymbol{\epsilon}_{k\eta})\left(1+i\boldsymbol{k}\cdot\boldsymbol{r}+\cdots\right)|\beta\rangle c_\alpha^\dagger c_\beta\right)a_{k\eta}+h.c.\right] \\ &\sim \frac{e}{mc}\sum_{\boldsymbol{k},\eta}\sqrt{\frac{\hbar c}{2Vk}}\left[\left(\sum_{\alpha,\beta}\langle\alpha|(\boldsymbol{p}\cdot\boldsymbol{\epsilon}_{k\eta})|\beta\rangle c_\alpha^\dagger c_\beta\right)a_{k\eta}+h.c.\right] \end{aligned} \tag{A.8}$$

To zeroth order of $\boldsymbol{k}\cdot\boldsymbol{r}$ corresponds to the electric dipole approximation. Using the relation

$$\boldsymbol{p}=\frac{m}{i\hbar}\left[\boldsymbol{r},H_0\right]. \tag{A.9}$$

H_1 can be represented by dipole operator conveniently as

$$\begin{aligned} H_1 \quad &\sim \frac{e}{mc}\sum_{\boldsymbol{k},\eta}\sqrt{\frac{\hbar c}{2Vk}}\left[\left(\sum_{\alpha,\beta}\langle\alpha|(\frac{m}{i\hbar}\left[\boldsymbol{r},H_0\right]\cdot\boldsymbol{\epsilon}_{k\eta})|\beta\rangle c_\alpha^\dagger c_\beta\right)a_{k\eta}+h.c.\right] \\ &=-i\frac{e}{mc}\sum_{\boldsymbol{k},\eta}\sqrt{\frac{\hbar c}{2Vk}}\left[\left(\sum_{\alpha,\beta}\frac{m}{\hbar}(E_\beta-E_\alpha)\langle\alpha|(\boldsymbol{r}\cdot\boldsymbol{\epsilon}_{k\eta})|\beta\rangle c_\alpha^\dagger c_\beta\right)a_{k\eta}-h.c.\right] \\ &=-\left(\sum_{\alpha,\beta}\langle\alpha|(e\boldsymbol{r})|\beta\rangle c_\alpha^\dagger c_\beta\right)\cdot\sum_{\boldsymbol{k},\eta}\sqrt{\frac{\hbar c}{2Vk}}(ik)\left[\boldsymbol{\epsilon}_{k\eta}a_{k\eta}-h.c.\right] \\ &=-\sum_i \boldsymbol{D}_i\cdot\boldsymbol{E}(\boldsymbol{k}\cdot\boldsymbol{r}_i=0). \end{aligned} \tag{A.10}$$

The expression into dipole operator is convenient when we consider local orbitals since the physical meaning of dipole is transparent. To start from the local picture, dipole operator is easier to work with. For conductor, k is a good quantum number, the original expression is easier to implement.

Now, if we assume the initial, final and intermediate state to be

$$\begin{aligned} |\Psi_i\rangle &= |I\rangle\otimes|n_i\rangle \\ |\Psi_f\rangle &= |F\rangle\otimes|n_f\rangle \\ |\Psi_\nu\rangle &= |\nu\rangle\otimes|n_\nu\rangle. \end{aligned} \tag{A.11}$$

Here, $|I,F,\nu\rangle$ represent the many electron wave function of the probed system. $|n_i,n_f,n_\nu\rangle$ represent the photon wave function. With those definition, we can calculate $\langle\Psi_f|T|\Psi_i\rangle$,where

$$T=H_2+H_1\frac{1}{E-(H_0+H_{field})+i\varepsilon}H_1. \tag{A.12}$$

$E = E_i + \hbar c k_i = E_s + \hbar c k_s$. The transition rate is

$$\begin{aligned} d\Gamma &= 2\pi |\langle \Psi_f | T | \Psi_i \rangle|^2 \rho_{q_s}^{(\gamma)}; \\ \rho_{q_s}^{(\gamma)} &= \frac{V}{(2\pi)^3} \frac{d^3 q_s}{c dq_s} = \frac{V}{(2\pi)^3} \frac{q_s^2}{c} d\Omega; \\ d\Gamma(\frac{V}{c}) &= \frac{d\sigma}{d\Omega} \end{aligned} \tag{A.13}$$

$$\begin{aligned} \langle \Psi_f | H_2 | \Psi_i \rangle &= \frac{2e^2}{2mc^2} \frac{\hbar c}{2V} \sum_{\substack{\boldsymbol{k}\eta \\ \boldsymbol{k}'\eta'}} \frac{\boldsymbol{\epsilon}_{k\eta} \cdot \boldsymbol{\epsilon}_{k'\eta'}}{\sqrt{kk'}} \left(\sum_{\alpha\beta} \langle \alpha | e^{-i(\boldsymbol{k}-\boldsymbol{k}')\cdot \boldsymbol{r}} | \beta \rangle \langle F | c_\alpha^\dagger c_\beta | I \rangle \right) \langle n_f | a_{k\eta}^\dagger a_{k'\eta'} | n_i \rangle \\ &= \frac{e^2}{mc^2} \frac{\hbar c}{2V} \frac{\boldsymbol{e}_i \cdot \boldsymbol{e}_s}{\sqrt{q_i q_s}} \sum_{\alpha\beta} \left(\langle \alpha | e^{i\boldsymbol{q}\cdot\boldsymbol{r}} | \beta \rangle \right) \langle F | c_\alpha^\dagger c_\beta | I \rangle = \frac{e^2}{mc^2} \frac{\hbar c}{2V} \frac{1}{\sqrt{q_i q_s}} \mathcal{A}_2 \end{aligned} \tag{A.14}$$

Above expression is the only non-zero contribution if we assume $|n_i\rangle$ and $|n_f\rangle$ are both single mode laser. This term represent an incident photon with momentum q_i is absorbed by the system and release a photon with momentum q_s. So $\boldsymbol{q} = \boldsymbol{q}_i - \boldsymbol{q}_s$.

Similarly, we can evaluate the contribution of the second term.

$$
\begin{aligned}
&\langle\Psi_f|H_1\frac{1}{E-(H_0+H_{field})+i\varepsilon}H_1|\Psi_i\rangle = \langle\Psi_f|\frac{e}{mc}\sum_{\boldsymbol{k},\eta}\sqrt{\frac{\hbar c}{2Vk}}\\
&\left[\left(\sum_{\alpha,\beta}\langle\alpha|(\boldsymbol{p}\cdot\boldsymbol{\epsilon}_{k\eta})e^{i\boldsymbol{k}\cdot\boldsymbol{r}}|\beta\rangle c_\alpha^\dagger c_\beta\right)a_{k\eta}+h.c.\right]\\
&\left(\sum_\nu|\Psi_\nu\rangle\langle\Psi_\nu|\right)\frac{1}{E-(H_0+H_{field})+i\varepsilon}\left(\sum_{\nu'}|\Psi_{\nu'}\rangle\langle\Psi_{\nu'}|\right)H_1|\Psi_i\rangle\\
&=\left(\frac{e}{mc}\right)^2\frac{\hbar c}{2V}\sum_\nu\frac{1}{\sqrt{q_iq_s}}\Big\{\left(\sum_{\alpha,\beta}\langle\alpha|(\boldsymbol{p}\cdot\boldsymbol{e}_s)e^{-i\boldsymbol{q}_s\cdot\boldsymbol{r}}|\beta\rangle\right)\left(\sum_{\alpha',\beta'}\langle\alpha'|(\boldsymbol{p}\cdot\boldsymbol{e}_i)e^{i\boldsymbol{q}_i\cdot\boldsymbol{r}}|\beta'\rangle\right)\\
&\langle F|c_\alpha^\dagger c_\beta|\nu\rangle\langle n_\nu|\langle\nu|\frac{1}{E-(H_0+H_{field})+i\varepsilon}|\nu'\rangle|n_{\nu'}\rangle\langle\nu'|c_{\alpha'}^\dagger c_{\beta'}|I\rangle\langle n_f|a_{\boldsymbol{q}_s}^\dagger|n_\nu\rangle\langle n_{\nu'}|a_{\boldsymbol{q}_i}|n_i\rangle\\
&+\left(\sum_{\alpha,\beta}\langle\alpha|(\boldsymbol{p}\cdot\boldsymbol{e}_i)e^{i\boldsymbol{q}_i\cdot\boldsymbol{r}}|\beta\rangle\right)\left(\sum_{\alpha',\beta'}\langle\alpha'|(\boldsymbol{p}\cdot\boldsymbol{e}_s)e^{-i\boldsymbol{q}_s\cdot\boldsymbol{r}}|\beta'\rangle\right)\\
&\langle F|c_\alpha^\dagger c_\beta|\nu\rangle\langle n_\nu|\langle\nu|\frac{1}{E-(H_0+H_{field})+i\varepsilon}|\nu'\rangle|n_{\nu'}\rangle\langle\nu'|c_{\alpha'}^\dagger c_{\beta'}|I\rangle\langle n_f|a_{\boldsymbol{q}_i}|n_\nu\rangle\langle n_{\nu'}|a_{\boldsymbol{q}_s}^\dagger|n_i\rangle\Big\}\\
=\;&\left(\frac{e}{mc}\right)^2\frac{\hbar c}{2V}\frac{1}{\sqrt{q_iq_s}}\sum_\nu\sum_{\substack{\alpha\alpha'\\\beta\beta'}}\langle\alpha|(\boldsymbol{p}\cdot\boldsymbol{e}_s)e^{-i\boldsymbol{q}_s\cdot\boldsymbol{r}}|\alpha'\rangle\langle\beta|(\boldsymbol{p}\cdot\boldsymbol{e}_i)e^{i\boldsymbol{q}_i\cdot\boldsymbol{r}}|\beta'\rangle\\
&\left[\frac{\langle F|c_\alpha^\dagger c_{\alpha'}|\nu\rangle\langle\nu|c_\beta^\dagger c_{\beta'}|I\rangle}{(E_i+n_i(\hbar\omega_i))-(E_\nu+(n_i-1)(\hbar\omega_i))+i\varepsilon}+\frac{\langle F|c_\beta^\dagger c_{\beta'}|\nu\rangle\langle\nu|c_\alpha^\dagger c_{\alpha'}|I\rangle}{E_i-E_\nu-\hbar\omega_s+i\varepsilon}\right]\\
=\;&\left(\frac{e}{mc}\right)^2\frac{\hbar c}{2V}\frac{1}{\sqrt{q_iq_s}}\sum_\nu\sum_{\substack{\alpha\alpha'\\\beta\beta'}}\langle\alpha|(\boldsymbol{p}\cdot\boldsymbol{e}_s)e^{-i\boldsymbol{q}_s\cdot\boldsymbol{r}}|\alpha'\rangle\langle\beta|(\boldsymbol{p}\cdot\boldsymbol{e}_i)e^{i\boldsymbol{q}_i\cdot\boldsymbol{r}}|\beta'\rangle\\
&\left[\frac{\langle F|c_\alpha^\dagger c_{\alpha'}|\nu\rangle\langle\nu|c_\beta^\dagger c_{\beta'}|I\rangle}{(E_i-E_\nu+\hbar\omega_i+i\varepsilon}+\frac{\langle F|c_\beta^\dagger c_{\beta'}|\nu\rangle\langle\nu|c_\alpha^\dagger c_{\alpha'}|I\rangle}{E_i-E_\nu-\hbar\omega_s+i\varepsilon}\right]=\frac{e^2}{mc^2}\frac{\hbar c}{2V}\frac{1}{\sqrt{q_iq_s}}\frac{\mathcal{A}_1}{m}
\end{aligned}
\tag{A.15}
$$

The collision rate is

$$
\begin{aligned}
d\Gamma &= (2\pi)\left[\frac{e^2}{mc^2}\frac{\hbar c}{2V}\right]^2\frac{1}{q_iq_s}|\mathcal{A}_2+\frac{\mathcal{A}_1}{m}|^2\frac{V}{(2\pi)^3}\frac{q_s^2}{c}d\Omega\\
&= \left(\frac{e^2}{4\pi mc^2}\right)^2\left(\frac{\hbar c}{V}\right)^2\frac{V}{c}\frac{q_s}{q_i}|\mathcal{A}_2+\frac{\mathcal{A}_1}{m}|^2d\Omega
\end{aligned}
\tag{A.16}
$$

And the differential cross section is

$$
\frac{d\sigma}{d\Omega}=r_0^2\frac{q_s}{q_i}\hbar^2|\mathcal{A}_2+\frac{\mathcal{A}_1}{m}|^2. \tag{A.17}
$$

Differential cross section is

$$\frac{d^2\sigma}{d\Omega d\omega_s} = \hbar r_0^2 \frac{\omega_s}{\omega_i} \left[\frac{1}{Z} \sum_{I,F} e^{-\beta E_I} |M_{F,I}|^2 \delta \left(E_F - E_I - \hbar(\omega_i - \omega_s) \right) \right] \tag{A.18}$$

Here, E_I, E_F corresponds to the many-electron system's initial and final energy. $M_{F,I} = \mathcal{A}_2 + \frac{\mathcal{A}_1}{m}$ where M is the effective light scattering operator. With this definition, we can calculate

And now we define $\boldsymbol{q} = \boldsymbol{q}_i - \boldsymbol{q}_s$ which is the momentum transfer to the system by photon. Usual Raman scattering process with visible light satisfied $|\boldsymbol{q}| << k_F$. Physically, that means the wave length of light is much larger than lattice constant which is the typical range for electron to move around. Thus, **Raman scattering detect the zero momentum transfer excitation.**

$M_{F,I}$ has contribution from H_1 and H_2. H_1 couples the current to a single photon. H_2 couples the electron charge to two photons.

Assume we have two bands, the conduction band and the valence band. In the nonresonant intra band case, H_1 couples to the current, which means the photon gives part of its energy to the electron current which is contributed from the conduction band. Thus we end up with an electron-hole pair in the conduction band and a photon with lower energy. In the intra band situation, the valence electron is excited to some intermediate state and decay into the final state with emitted photon. When the incident or emitted photon energy fits the energy gap separation, it is resonant.

The simple picture says that the electrons near the fermi surface is probed by nonresonant intra band scattering and excitations that involve inter band transition are probed by intermediate state scattering.

$$\begin{aligned} M_{F,I} &= \boldsymbol{e}_i \cdot \boldsymbol{e}_s \sum_{\alpha,\beta} \left(\int d^3 r \varphi_\alpha^*(\boldsymbol{r}) e^{i\boldsymbol{q}\cdot\boldsymbol{r}} \varphi_\beta(\boldsymbol{r}) \right) \langle F | c_\alpha^\dagger c_\beta | I \rangle \\ &+ \frac{1}{m} \sum_{\nu} \sum_{\substack{\alpha\alpha' \\ \beta\beta'}} \langle \alpha | \boldsymbol{p} \cdot \boldsymbol{e}_s e^{-i\boldsymbol{q}_s\cdot\boldsymbol{r}} | \alpha' \rangle \langle \beta | \boldsymbol{p} \cdot \boldsymbol{e}_i e^{i\boldsymbol{q}_i\cdot\boldsymbol{r}} | \beta' \rangle \\ &\left(\frac{\langle F | c_\alpha^\dagger c_{\alpha'} | \nu \rangle \langle \nu | c_\beta^\dagger c_{\beta'} | I \rangle}{E_I - E_\nu + \hbar\omega_i + i\varepsilon} + \frac{\langle F | c_\beta^\dagger c_{\beta'} | \nu \rangle \langle \nu | c_\alpha^\dagger c_{\alpha'} | I \rangle}{E_I - E_\nu - \hbar\omega_s + i\varepsilon} \right) \end{aligned} \tag{A.19}$$

Or under electric dipole approximation, it can be written in terms of dipole operator

$$\begin{aligned} M_{F,I} &= \boldsymbol{e}_i \cdot \boldsymbol{e}_s \sum_{\alpha,\beta} \left(\int d^3 r \varphi^*_\alpha(\boldsymbol{r}) \varphi_\beta(\boldsymbol{r}) \right) \langle F | c^\dagger_\alpha c_\beta | I \rangle \\ &+ mc^2 \sum_\nu \sum_{\substack{\alpha\alpha' \\ \beta\beta'}} \langle \alpha | (\boldsymbol{r}) \cdot \boldsymbol{e}_s | \alpha' \rangle \langle \beta | (\boldsymbol{r}) \cdot \boldsymbol{e}_i | \beta' \rangle \\ &\left(\frac{\langle F | c^\dagger_\alpha c_{\alpha'} | \nu \rangle \langle \nu | c^\dagger_\beta c_{\beta'} | I \rangle}{E_I - E_\nu + \hbar\omega_i + i\varepsilon} + \frac{\langle F | c^\dagger_\beta c_{\beta'} | \nu \rangle \langle \nu | c^\dagger_\alpha c_{\alpha'} | I \rangle}{E_I - E_\nu - \hbar\omega_s + i\varepsilon} \right). \end{aligned} \tag{A.20}$$

or

$$\begin{aligned} M_{F,I} &= \boldsymbol{e}_i \cdot \boldsymbol{e}_s \sum_{\alpha,\beta} \left(\int d^3 r \varphi^*_\alpha(\boldsymbol{r}) \varphi_\beta(\boldsymbol{r}) \right) \langle F | c^\dagger_\alpha c_\beta | I \rangle \\ &+ \frac{1}{m} \sum_\nu \sum_{\substack{\alpha\alpha' \\ \beta\beta'}} \langle \alpha | (\boldsymbol{p}) \cdot \boldsymbol{e}_s | \alpha' \rangle \langle \beta | (\boldsymbol{p}) \cdot \boldsymbol{e}_i | \beta' \rangle \\ &\left(\frac{\langle F | c^\dagger_\alpha c_{\alpha'} | \nu \rangle \langle \nu | c^\dagger_\beta c_{\beta'} | I \rangle}{E_I - E_\nu + \hbar\omega_i + i\varepsilon} + \frac{\langle F | c^\dagger_\beta c_{\beta'} | \nu \rangle \langle \nu | c^\dagger_\alpha c_{\alpha'} | I \rangle}{E_I - E_\nu - \hbar\omega_s + i\varepsilon} \right). \end{aligned} \tag{A.21}$$

The first term should be considered for xx and $x'x'$ scattering process and it had no resonance behavior. The xy and $x'y'$ are purely contribution from the second term.

Appendix B

Polarization and pseudospin structure

Here, we give details on how symmetry constrains the polarization dependence and pseudospin structure of the electronic Raman transitions considered in the main text. We focus on on-site transitions; as stated in the main text, the inter-site transitions discussed are of the same symmetry as on-site transitions, and do not need to be considered separately here. In addition, we show that the Raman tensor can indeed induce pseudospin-flip processes, even if $R_{\mu\nu}$ is assumed to act only on orbital (and not spin) degrees of freedom.

Beginning with Eq. (3) of the main text, the objective is to use site symmetry and time reversal to constrain the matrix elements for on-site transitions, contained in the 6×6 matrix $M_{0;\mu\nu}$. We focus on a single lattice site $\boldsymbol{r}$ and thus drop the site label from our analysis. As discussed in the main text, we consider an idealized case of D_{4h} site symmetry and only later consider breaking down to C_{4h}. The analysis proceeds in the high-temperature phase, with no spontaneous symmetry breaking due to long-range magnetic order.

We focus on two 2×2 blocks of $M_{0;\mu\nu}$, one describing transitions from a j-doublet to another j-doublet ($M_{\mu\nu}^{j\to j}$), and another describing transitions from a j-doublet to a $\bar{j}$-doublet ($M_{\mu\nu}^{j\to\bar{j}}$). The on-site $j_2 \to j_1$ transition and the inter-site $\boldsymbol{r} \to s$ transition are both of $j \to j$ type, while the on-site $\bar{j}_2 \to j_1$ and inter-site $\boldsymbol{r} \to d_{x^2-y^2}$ transitions are of $j \to \bar{j}$ type. (The symmetry constraints on $j \to \bar{j}$ and $\bar{j} \to j$ transitions are the same.)

Ignoring inversion, which acts trivially on the electronic states of interest, D_{4h} is generated by the operations C_{4z} (four-fold rotation about the z-axis), C_{2x} (two-fold rotation about the x-axis),

and C_{2xy} (two-fold rotation about the $(\hat{x}+\hat{y})$-axis). It will also be useful to explicitly consider $C_{2z} = (C_{4z})^2$. We consider the single-ion Hamiltonian obtained by projecting spin-orbit coupling and D_{4h} crystal field to the t_{2g} manifold, which allows us to obtain wave functions for the electronic states of interest. Using these wave functions, we find the following matrices representing the action of D_{4h} symmetry on the j-doublets:

$$C_{4z}^{j} = -\begin{pmatrix} e^{-i\pi/4} & 0 \\ 0 & e^{i\pi/4} \end{pmatrix} \tag{B.1}$$

$$C_{2z}^{j} = -i\sigma^z \tag{B.2}$$

$$C_{2x}^{j} = i\sigma^x \tag{B.3}$$

$$C_{2xy}^{j} = \frac{-i}{\sqrt{2}}(\sigma^x + \sigma^y), \tag{B.4}$$

where $\sigma^x, \sigma^y, \sigma^z$ are the usual 2×2 Pauli matrices. For $\bar{j}$-doublets we find:

$$C_{4z}^{\bar{j}} = \begin{pmatrix} e^{-i\pi/4} & 0 \\ 0 & e^{i\pi/4} \end{pmatrix} \tag{B.5}$$

$$C_{2z}^{\bar{j}} = -i\sigma^z \tag{B.6}$$

$$C_{2x}^{\bar{j}} = i\sigma^x \tag{B.7}$$

$$C_{2xy}^{\bar{j}} = \frac{i}{\sqrt{2}}(\sigma^x + \sigma^y). \tag{B.8}$$

In both cases time reversal is given by

$$\mathcal{T} = i\sigma^y K, \tag{B.9}$$

where K is the complex conjugation operator. We note that these forms only depend on the symmetry properties of the electronic states, which are expected to be captured accurately in our simple treatment.

Now we analyze the constraints on the matrix elements. First, we consider the action of symmetry on $R_{\mu\nu}$, which has to agree with that on the corresponding matrix elements. We only

need to consider those operations that take a given component of $R_{\mu\nu}$ into itself (or minus itself):

$$C_{2z} : R_{xx} \rightarrow R_{xx} \tag{B.10}$$

$$C_{2x} : R_{xx} \rightarrow R_{xx} \tag{B.11}$$

$$C_{2z} : R_{x'x'} \rightarrow R_{x'x'} \tag{B.12}$$

$$C_{2xy} : R_{x'x'} \rightarrow R_{x'x'} \tag{B.13}$$

$$C_{2z} : R_{xy} \rightarrow R_{xy} \tag{B.14}$$

$$C_{2x} : R_{xy} \rightarrow -R_{xy} \tag{B.15}$$

$$C_{2z} : R_{x'y'} \rightarrow R_{x'y'} \tag{B.16}$$

$$C_{2xy} : R_{x'y'} \rightarrow -R_{x'y'}. \tag{B.17}$$

In addition, $R_{\mu\nu}$ is invariant under time reversal.

Now we consider the matrix elements $M_{\mu\nu}^{j\rightarrow j}$ and $M_{\mu\nu}^{j\rightarrow \bar{j}}$. In each case, time reversal allows the matrices $1_{2\times 2}$ and $i\sigma^{\mu}$ ($\mu = x, y, z$) to appear with arbitrary real coefficients, where $1_{2\times 2}$ is the 2×2 identity matrix. For example, time reversal allows the form $M_{xx}^{j\rightarrow j} = a_0 \cdot 1_{2\times 2} + a_{\mu} i\sigma^{\mu}$, without yet imposing any other symmetries. Using all symmetries gives

$$M_{xx}^{j\rightarrow j}, M_{x'x'}^{j\rightarrow j}, M_{xx}^{j\rightarrow \bar{j}}, M_{x'y'}^{j\rightarrow \bar{j}} \propto 1_{2\times 2} \tag{B.18}$$

$$M_{xy}^{j\rightarrow j}, M_{x'y'}^{j\rightarrow j}, M_{x'x'}^{j\rightarrow \bar{j}}, M_{xy}^{j\rightarrow \bar{j}} \propto \sigma^{z}. \tag{B.19}$$

The information provided in Table I of the main text follows from these results. We note in particular that only pseudospin-flip transitions contribute in xy polarization.

Effect of C_{4h} site symmetry. The true Ir site symmetry is C_{4h}, which is generated by the operations C_{4z} and inversion. Focusing on effects of this lower symmetry in xy polarization, we find that $M_{xy}^{j\rightarrow j}$ and $M_{xy}^{j\rightarrow \bar{j}}$ are both allowed to have a non-pseudospin-flip contribution. The fact that a peak is not seen in xy polarization suggests that the breaking of $D_{4h} \rightarrow C_{4h}$ is a weak effect, at least for the electronic states probed by our Raman measurements.

Below Neel temperature. Below the Neel temperature, long-range magnetic order lowers the site symmetry. Assuming the moments lie in the xy plane and point along the x' axis, the site

symmetry is generated by the operations $C_{2z}\mathcal{T}$ and C_{2xy} [181, 182, 183]. All components of $R_{\mu\nu}$ are left invariant by $C_{2z}\mathcal{T}$. This operation acts on both doublets as the matrix $C_{2z}\mathcal{T} = -i\sigma^x K$, and this allows the matrices (with real coefficients) $1, \sigma^x, \sigma^y, i\sigma^z$ to appear. Focusing again on xy polarization, there are no further constraints on $M_{xy}^{j\to j}$ and $M_{xy}^{j\to \bar{j}}$, so non-pseudospin-flip transitions are allowed to contribute in xy polarization. The absence of a peak indicates that Neel order is not strong enough compared to electronic energy scales to have a significant effect on the Raman transitions probed.

Raman scattering can flip the pseudospin. In the absence of spin-orbit coupling, the Raman tensor cannot induce spin-flip processes. This follows from the presence of SU(2) spin rotation symmetry, and the fact that $R_{\mu\nu}$ commutes with SU(2) spin rotations. In the present case, there is substantial spin-orbit coupling, and SU(2) spin symmetry is not present, opening the possibility of pseudospin flips in the Raman process.

To assess whether $R_{\mu\nu}$ indeed contains pseudospin-flip transitions with significant amplitude, we make the conservative assumption that spin-orbit coupling only enters in the initial and final t_{2g} states, ignoring spin-orbit coupling in the intermediate state. As a result $R_{\mu\nu}$ commutes with SU(2) spin rotations, and spin-flip processes are forbidden. However, we find pseudospin-flip processes are nonetheless Raman active. To illustrate this point we focus on a single lattice site for simplicity and assume:

$$R_{\mu\nu} = f_{A\sigma}^{\dagger} \mathcal{R}_{AB}^{\mu\nu} f_{B\sigma}. \tag{B.20}$$

Here $A, B = yz, xz, xy$ labels the t_{2g} orbital states, $\sigma = \uparrow, \downarrow$ is electron spin, and the 3×3 matrix $\mathcal{R}^{\mu\nu}$ is constrained by site symmetry and time reversal. We are thus assuming that $R_{\mu\nu}$ acts only on the orbital degrees of freedom. Spin-orbit coupling enters via the single-ion Hamiltonian, whose local energy eigenstates (the j_1, j_2 and $\bar{j}_2$ doublets) have mixed spin and orbital character. We determined the general symmetry-allowed form of $\mathcal{R}^{\mu\nu}$. Then transforming the expression for $R_{\mu\nu}$ into the basis of spin-orbital energy eigenstates, we find that pseudospin-flip processes are fully allowed, even though $R_{\mu\nu}$ contains no spin-flip terms. This justifies our analysis of the Raman

process including both transitions with and without pseudospin flips.